

**A Fast Pipelined Trigger for the
H1 Experiment at HERA
Based on
Multiwire Proportional Chamber Signals**

Inaugural Dissertation
zur Erlangung der philosophischen Doktorwürde
vorgelegt der
Philosophischen Fakultät II
der
Universität Zürich

von
Stefan Eichenberger
aus Zürich

begutachtet von Prof. Dr. P. Truöl
und Dr. U. Straumann

Zürich 1993

**A Fast Pipelined Trigger for the
H1 Experiment at HERA
Based on
Multiwire Proportional Chamber Signals**

Inaugural Dissertation
zur Erlangung der philosophischen Doktorwürde
vorgelegt der
Philosophischen Fakultät II
der
Universität Zürich

von
Stefan Eichenberger
aus Zürich

begutachtet von Prof. Dr. P. Truöl
und Dr. U. Straumann

Zürich 1993

Table of Contents

Table of Contents	1
List of figures	3
List of tables	5
Abstract	6
Zusammenfassung	7
Introduction	9
The HERA machine	9
The H1 detector	10
The H1 tracking system	12
The H1 trigger environment	14
Background sources	15
The H1 trigger scheme	17
The first level trigger	22
The z-vertex trigger	27
Principles of operation	27
Peak significance criteria	32
Trigger acceptance	33
Geometrical constraints	34
Chamber response to charged particles	37
Ray multiplicities	41
The influence of incoherent noise	47
Monte Carlo simulations of trigger efficiencies	48
Experiences during the first H1 run period	54
The MWPC performance	54
The z-vertex trigger performance	58
Trigger performance on deep inelastic scattering events	62
Total photoproduction cross section measurements	67
Hard scattering in γp interactions	69
Improving the trigger as a vertex estimator	69
Principle of the vertex estimator	69
Performance of the vertex estimator	71

Hardware realization	76
Block diagram	76
The rayfinder electronics	76
The rayfinder backplane and rack layout	81
The vertex finder crate	86
The RAM card	86
The vertex finder card	88
The adder cards	94
The driver card	95
Test procedures	96
The rayfinder electronics and the scanner	96
Testing the RAM card	99
Difficult error conditions	101
Online monitoring and diagnosing	102
Expanding the z-vertex trigger	106
Big rays and the big ray distribution box	106
Extended peak significance criterion	108
Building a vertex estimator	110
Summary and Conclusion	112
Appendix A: Pipelined triggers	113
Appendix B: XILINX logic cell arrays	114
Appendix C: Low energy cutoff in the single ray acceptance	118
Appendix D: Dictionary of abbreviations	122
Bibliography	124
Acknowledgements	128
Curriculum vitae	129

List of figures

Fig. 1 The HERA storage ring	9
Fig. 2 The H1 detector	11
Fig. 3 The H1 tracking system	13
Fig. 4 Event vertex distribution along the beam axis	17
Fig. 5 The H1 trigger concept	19
Fig. 6 The detector subsystems included in the first level trigger	22
Fig. 7 The first level trigger of H1	23
Fig. 8 Principle of the ToF trigger	24
Fig. 9 Cross sectional view of the central tracker	25
Fig. 10 The big tower granularity of the calorimeter	26
Fig. 11 Principle of the z-vertex trigger	29
Fig. 12 Pad sizes of the barrel MWPCs	30
Fig. 13 An electron-tagged two jet event accepted by the z-vertex trigger	31
Fig. 14 A proton - beam pipe interaction rejected by the z-vertex trigger	31
Fig. 15 Error estimation of the peak significance	32
Fig. 16 Geometrical acceptance of the z-vertex trigger	35
Fig. 17 Low momentum cutoff of the z-vertex trigger	36
Fig. 18 Probability for finding the correct ray	36
Fig. 19 Calculating the charge distribution of a track	38
Fig. 20 The charge deposited by a track on the MWPC cathode plane	39
Fig. 21 Single ray multiplicity as a function of ϑ	43
Fig. 22 Inefficiencies at pad boundaries	44
Fig. 23 Acceptance for artificial, jet-like bundles of particle tracks	45
Fig. 24 Peak significance as a function of the chamber threshold	46
Fig. 25 Trigger efficiency as a function of the noise rate in the MWPCs	49
Fig. 26 Kinematical variables of a neutral current DIS interaction	50
Fig. 27 Trigger efficiency for DIS events as a function of x and Q^2	51
Fig. 28 Trigger efficiency for DIS events as a function of p_t and ϑ_{jet}	53
Fig. 29 Trigger efficiency for DIS and $c\bar{c}$ events as a function the chamber digitization threshold	54
Fig. 30 The time resolution of CIP	56
Fig. 31 Timing of the synchronization window	57
Fig. 32 An electron beam related background event accepted by the z-vertex trigger	58

Fig. 33 Distribution of event vertices along the beam axis with and without the z-vertex trigger required	60
Fig. 34 Reconstructed vertex versus peak location	61
Fig. 35 A typical DIS event	63
Fig. 36 Distribution of the DIS event sample in the $x-Q^2$ plane	64
Fig. 37 Comparison between simulated and recorded z-vertex histograms	65
Fig. 38 Comparison of trigger efficiencies for a DIS sample	66
Fig. 39 The total γp cross section as measured by H1 and ZEUS	68
Fig. 40 Principle of the vertex estimator	70
Fig. 41 Cuts performed by the vertex estimator	72
Fig. 42 Performance of the vertex estimator	75
Fig. 43 Block diagram of the z-vertex trigger	77
Fig. 44 The rayfinder printed circuit board	79
Fig. 45 Photo of a rayfinder printed circuit board	80
Fig. 46 Signal distribution at the trigger input	82
Fig. 47 Rack and crate layout	83
Fig. 48 Side view of a rayfinder crate	84
Fig. 49 Signal quality on the rayfinder backplane	85
Fig. 50 Block diagram of the RAM card	87
Fig. 51 Block diagram of the adder and vertex finder card	89
Fig. 52 Implementation of a peak finding algorithm	91
Fig. 53 Photo of the vertex finder card	92
Fig. 54 Propagation delay of an adder cascade	93
Fig. 55 The <i>scanner</i> XILINX program	97
Fig. 56 A XILINX program to test the RAM card	99
Fig. 57 The adder card XILINX program during normal operation	103
Fig. 58 The big ray distribution box	106
Fig. 59 Hardware extensions needed to calculate the peak significance in view of the statistical error of the histogram background	108
Fig. 60 Principle of a pipelined trigger	113
Fig. 61 Principle of a XILINX logic cell array	114
Fig. 62 A XILINX configurable logic block	116
Fig. 63 Low momentum cutoff: Geometry	119
Fig. 64 Track acceptance as a function of p_t and DCA	120
Fig. 65 Low momentum tracks in the R-z projection	121

List of tables

Table 1: Data acquisition parameters of the HERA detectors	14
Table 2: Comparison between HERA and other colliders	15
Table 3: Main H1 trigger parameters	21
Table 4: Geometrical properties of the proportional chambers used by the z-vertex trigger	28
Table 5: Efficiency of the vertex estimator	74
Table 6: Parity bit allocation	104
Table 7: XILINX 3000 series: available dies	115

Abstract

A fast, pipelined trigger for the H1 detector at the electron proton (ep) storage ring HERA is presented. It is based on the signals of a total of 1920 cathode pads from two cylindrical and one planar double layer multiwire proportional chamber. With their help, the vertex position of ep collisions along the beam axis is reconstructed. This allows discrimination between ep events, originating from the nominal interaction region, and background, introduced mainly by protons interacting with either beam defining apertures or residual gas atoms in the beam line vacuum chamber. The trigger works in a pipelined manner, delivering a delayed decision every 96 ns, corresponding to the accelerator bunch crossing frequency.

Chapter 1 describes the HERA accelerator complex and the H1 experiment.

Chapter 2 gives a general introduction into the H1 trigger environment, with a special emphasis on the first trigger level, of which the *z-vertex trigger* described herein is a part.

Chapter 3 introduces the general principle of the *z-vertex trigger*. It then discusses various aspects of the trigger acceptance, including geometrical restrictions, the influence of the chamber performance and the effect of noise. The trigger efficiency for Monte Carlo simulated deep inelastic scattering events (DIS) is discussed as a function of the kinematical parameters x , Q^2 , p_t and ϑ_{jet} . Experiences during the first H1 run period in 1992 are presented with a special emphasis on photoproduction and DIS events. Based on these experiences, a hardware extension is suggested, which improves the ratio between accepted ep collisions and the rejected background by a factor of two to four. Its feasibility is discussed in chapter 6.

A central part of this thesis, the hardware realization of the trigger, is discussed in chapter 4. It employs state of the art electronic technology, e.g. a custom designed gate array, XILINX logic cell arrays and a 16 MByte static RAM lookup table.

An important aspect of a digital circuitry of the complexity of this trigger is its testability. Chapter 5 is dedicated to these aspects. Computer controlled debugging procedures take full advantage of the reprogrammability of XILINX chips. Semi-automated test procedures are described, which are capable of detecting and tracing most conceivable errors. An online monitoring scheme is suggested.

Zusammenfassung

Ein schneller, totzeitfreier Trigger für das H1 Experiment am Elektron - Proton Speicherring HERA wird vorgestellt. Er basiert auf den Signalen von insgesamt 1920 Kathodenstreifen zweier zylindrischer und einer planaren Vieldrahtproportional-kammer mit jeweils zwei Lagen und rekonstruiert den Wechselwirkungspunkt einer Elektron - Proton (ep) Kollision entlang der Strahlachse. Mit dieser Vorrichtung lassen sich ep Wechselwirkungen von Untergrund unterscheiden. Letzterer stammt vorwiegend von Kollisionen zwischen Protonen und strahlbegrenzenden Aperturen bzw. Restgasatomen im evakuierten Strahlrohr. Der Trigger arbeitet totzeitfrei und produziert alle 96 ns eine Entscheidung. Dies entspricht dem minimalen zeitlichen Abstand von zwei aufeinanderfolgenden Strahlkreuzungen.

Nach einer kurzen Einführung zum H1 Experiment und dem HERA Beschleuniger-komplex werden in Kapitel 2 die allgemeinen Randbedingungen für eine Triggerent-scheidung bei H1 beschrieben. Die Bedeutung des ersten, schnellsten Triggerniveaus, zu dem auch der in dieser Arbeit diskutierte *z-Vertex Trigger* gehört, wird dabei besonders hervorgehoben.

Kapitel 3 erklärt dann zuerst das Prinzip des *z-Vertex Triggers*. Anschliessend werden verschiedene Aspekte der Triggerakzeptanz betrachtet, einschliesslich geome-trischer Randbedingungen, des Einflusses des Kammernverhaltens und des elektronischen Rauschens. Die Triggereffizienz wird anhand der Monte Carlo Simulation von tiefinelastischer Streuung als Funktion der kinematischen Variablen x , Q^2 , p_t und ϑ_{Jet} diskutiert. Erfahrungen der ersten HERA Betriebsperiode im Jahre 1992 werden rapportiert. Besonders berücksichtigt werden dabei Photoproduktionsereignisse und tiefinelastische Streuung. Aufgrund der dabei gewonnen Erkenntnisse kann ferner eine Erweiterung des Konzepts vorgeschlagen werden, die das Verhältnis zwischen akzeptierten ep Kollisionen und verworfenen Untergrundereignissen um etwa den Faktor zwei bis vier verbessert. Die technische Realisation davon wird in Kapitel 6 diskutiert.

Der zentrale Teil dieser Arbeit, der eigentliche Aufbau des Triggers wird im Kapitel 4 dargestellt. Erwähnenswert ist die Verwendung eines kundenspezifisch erstellten 'Gate Array' Schaltkreises sowie von programmierbaren XILINX 'Logic Cell Arrays'. Ein 16 MByte grosses statisches RAM ('random access memory') wird als Lookup Table betrieben.

Ein wichtiger Aspekt bei einer derart komplexen Verknüpfung logischer Komponenten ist es, die Funktionsweise zuverlässig zu überprüfen und zu überwachen. In Kapitel 5 wird gezeigt, wie mit rechnergesteuerten Prozeduren und unter Ausnutzung der Programmierbarkeit der XILINX Schaltkreise ein nahezu automatischer Test der Elektronik möglich ist. Die meisten denkbaren Fehler können mit diesen Methoden gefunden werden. Ein Vorschlag zur zeitgleichen Betriebsüberwachung wird gemacht.

1 Introduction

1.1 The HERA machine

HERA is the first electron-proton storage ring available to particle physicists. Its construction started 1984 at DESY in Hamburg, Germany. It finally came into operation

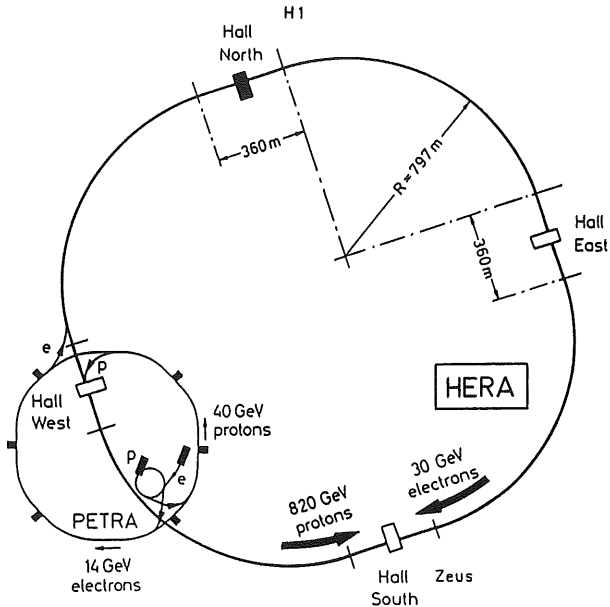


Fig. 1 The HERA storage ring.

in May 1992. Two independent machines reside in the 6.3 km long tunnel some 15 m below the surface. One is a conventional electron storage ring, which accelerates electrons from an initial 14 GeV to 30 GeV. The proton machine is loaded with 40 GeV protons, which are brought to 820 GeV before letting them collide with the electrons. The necessary magnetic field of 4.6 T to keep the protons on their track is produced by superconducting magnets. Figure 1 gives an overview of HERA and its injector chains. The former e^+e^- storage ring PETRA is operated as a pre-accelerator.

This new facility opens up an entirely new energy range, with the square of the four momentum transfer Q^2 reaching values up to $4 \cdot 10^4 \text{ GeV}^2$. This is two orders of magnitudes higher than what was attainable so far and allows investigations of substructures down to the millifermi scale. The proton structure function can be measured over a wide kinematical range (see figure 27, p. 51). The energy scale now accessible is also drastically illustrated by the measurement of the total γp cross section $\sigma_{\text{p}}^{\text{tot}}$ as shown in figure 39 on page 68.

γ -gluon processes produce heavy quarks including $b\bar{b}$ pairs. D-mesons can be investigated under much cleaner conditions than would be the case on hadron colliders, allowing the study of rare and forbidden decays.

In a second stage, spin flipping magnets in front and behind the two experiments ZEUS and H1 will put the natural transversal polarization of the electrons to use and allow studies with longitudinally polarized electrons, making HERA an even better tool to investigate quark substructures [1].

A detailed account of all aspects of HERA physics can be found in the proceedings of three workshops held before the experimental program started [2].

The accelerator delivered an integrated luminosity $\int \mathcal{L} \approx 62 \text{ nb}^{-1}$ during its first running period between May and November 1992. About 59% of that could be used for H1 data taking. The remainder was lost due to:

- Bad beam quality. After a new filling of one of the two machines, a certain time is needed to adjust the beams before one can safely switch on the sensible tracking detectors.
- Dead times introduced by the H1 trigger and readout system (see chapter 2.2).
- Malfunctions of the detector.

1.2 The H1 detector

The H1 detector, located at the north interaction point of HERA, is shown in figure 2. A detailed description is given in [3]. It consists of a central (A) and forward (B) tracking system, surrounded by a liquid argon calorimeter. The latter is separated into an electromagnetic (D) and hadronic (E) part. This entire system is located within

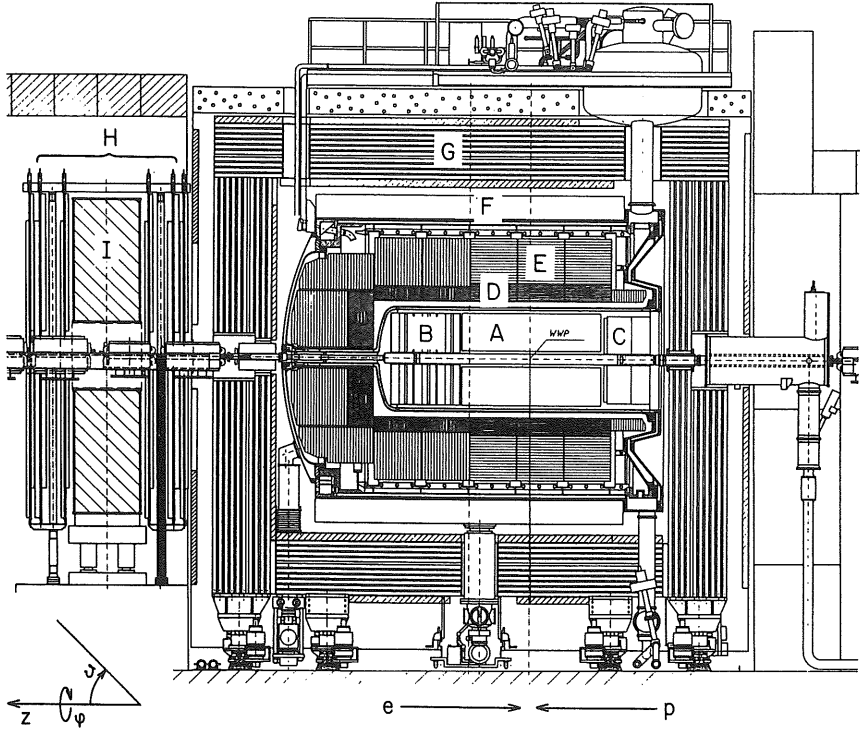


Fig. 2 The H1 detector consists of a central (A) and forward (B) tracker, a backward electromagnetic calorimeter (C), a liquid argon calorimeter with an electromagnetic (D) and hadronic (E) section, a solenoid (F), an instrumented iron system (G) and a forward muon system (H) with its own toroidal magnet (I). The H1 coordinate system as used throughout this document is indicated in the lower left corner.

a superconducting solenoid (F), which produces a homogenous magnetic field of 1.2 T parallel to the beam axis in the tracking region of the detector. Escaping muons are detected in the instrumented iron structure (G) and the forward muon system (H). The latter includes its own toroidal magnet (I) for energy determination.

The scattered electron escaping in the backward direction is detected in the warm backward electromagnetic calorimeter (C, BEMC), in front of which a four-layer

multiwire proportional chamber is located for better spatial resolution. Directly behind the calorimeter, a *time of flight* scintillator wall is installed (see figure 8, p. 24).

Electrons scattered under even smaller angles (≤ 5 mrad) escape through the beam tube and are detected by a crystal calorimeter at $z = -33$ m. This electron tagger, together with a similar apparatus at $z = -103$ m used to detect photons, is used as a luminosity measuring system. It records the $ep \rightarrow e\gamma$ rate, which is proportional to the luminosity \mathcal{L} and has a well-known cross section [4].

The cold calorimeter covers polar angles between $\vartheta = 4^\circ$ and 155° and has an energy resolution of $\sigma(E)/E = 0.10/\sqrt{E}$ for electrons and $\sigma(E)/E = 0.5/\sqrt{E}$ for hadrons (E in GeV). The electromagnetic section has a thickness of 20 to 30 radiation lengths, the hadronic section a thickness of 4 to 8 interaction lengths. The BEMC has a similar resolution as the liquid argon calorimeter and covers $154^\circ < \vartheta < 176^\circ$.

The octagonal iron yoke has a total length of 9.6 m and a height of 8.7 m. It is instrumented with streamer tubes. Some 140'000 wires are read out for muon tracking purposes [5].

1.3 The H1 tracking system

An overview of the H1 tracking system is given in figure 3. The forward tracker consists of three identical supermodules, each composed of a planar and radial driftchamber, a transition radiation volume and a double-layer multiwire proportional chamber (MWPC). The central region ($25^\circ < \vartheta < 155^\circ$) is surrounded by a set of concentric chambers. A cross sectional view is given in figure 9 on page 25.

The innermost chamber is a double layer MWPC (CIP), followed by a z-drift-chamber (CIZ) [6]. The latter measures the z-coordinate of a track to a precision of 250 μm with four sense wires per cell. It consists of 12 cells, each spanning 12 cm in z.

Two jet chambers (CJC) measure the R- ϕ projection of a track to within 210 μm , employing 24 and 32 layers of sense wires respectively. The inner chamber consists of

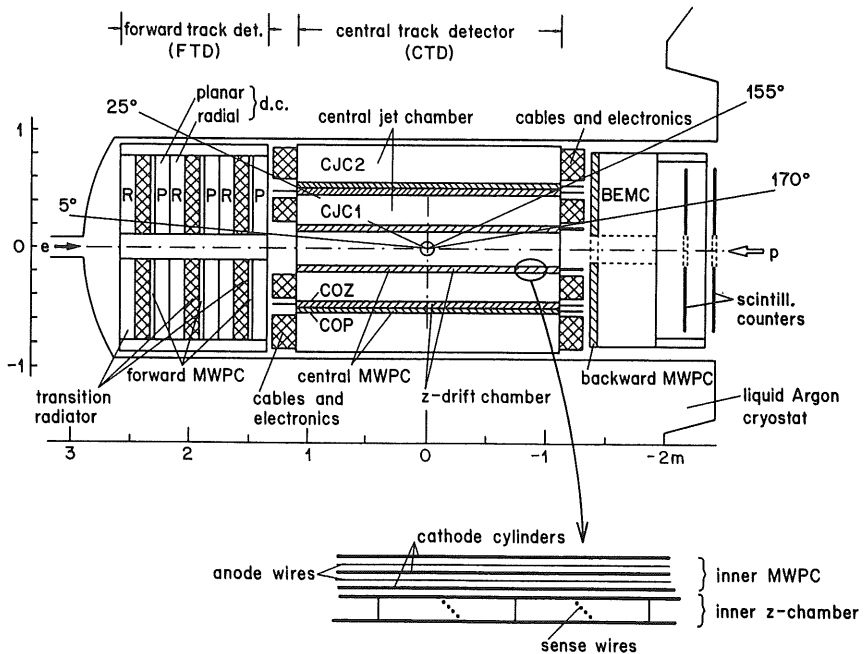


Fig. 3 The H1 tracking system.

30 ϕ -segments, the outer of 60. These cells are tilted in ϕ such that the magnetic field does not compromise the resolution of low momentum tracks.

The two jet chambers are separated by another MWPC (COP) and again a z-driftchamber (COZ). The latter measures z to an accuracy of 340 μm .

The proportional chambers are used for trigger purposes, including the z -vertex trigger presented in this document. Their properties and usage are further discussed in chapter 3.1.

2 The H1 trigger environment

HERA is the first of a new series of accelerators, which will challenge current trigger technologies. The task of any trigger is to discriminate background interactions from interesting physics events.

Limiting factor for many of today's experiments is the transfer rate with which data can be recorded onto permanent computer storage media. Whereas conventional tape recording devices allow recording speeds of up to roughly 0.5 MByte/s, experiments tend to require to save an ever increasing number of events as the luminosity is raised in order to make even very rare processes observable. Secondly, the event size is proportional to the number of electronic readout channels, which is maximized for best possible spatial granularity and therefore precision. This requires a trigger with a very high rejection power for high-rate background and near-perfect efficiency for physics events. Table 1 gives the main parameters of the data acquisition chain of the two HERA detectors H1 and Zeus.

	H1	Zeus
Number of channels	~ 270'000 (1)	~ 260'000
Raw data size	~ 3.07 MByte/Event	~ 2.87 MByte/Event
Average formatted size (2)	~ 44-132 kByte/Event	~ 100 kByte/Event
Bunch crossing rate	10.4 MHz	
Expected background rate	50 - 500 kHz at design luminosity	
Max. data logging rate	5 Hz	
Trigger suppression factor needed	$10^{-4} - 10^{-5}$	

(1) additional 214'000 channels are foreseen for the proposed silicon tracker detector [7].

(2) depending on the degree of zero-suppression and the analysis performed in front end computers.

Table 1: Data acquisition parameters of the HERA detectors [8], [9].

2.1 Background sources

With HERA being a precision tool to investigate the proton structure, almost all kinds of event classes of genuine ep collisions are of interest and should therefore be recorded. Thus, background is mainly caused by other than ep interactions.

Process	$p\bar{p}, pp$		ep	e^+e^-
σ_{Physics}	40 mb		10 μb (1)	≤ 40 nb (2)
σ_{Restgas}	$A^{2/3} \cdot 40$ mb		$A^{2/3} \cdot 40$ mb	150 μb
$\sigma_{\text{Physics}} / \sigma_{\text{Restgas}}$	1/6		1/24'000	1/3800
Machine	SppS	LHC (3)	HERA	LEP
$\mathcal{L} [\cdot 10^{31} \text{ cm}^{-2}\text{s}^{-1}]$	0.3	4000	1.6	1.7
I_p [mA]	6	865	163	-
I_e [mA]	-	-	58	3
$\frac{\sigma_{\text{Physics}}}{\sigma_{\text{Restgas}}} \cdot \frac{\mathcal{L}}{I_1 \cdot I_2}$	$\frac{1}{6} \cdot \frac{1}{20}$ $= 8.33 \cdot 10^{-3}$	$\frac{1}{6} \cdot 4.6$ $= 0.77$	$\frac{1}{24000} \cdot \frac{1}{100}$ $= 4.17 \cdot 10^{-7}$	$\frac{1}{3800} \cdot \frac{1}{2}$ $= 1.3 \cdot 10^{-4}$
Vacuum [Torr]	10^{-10}	10^{-11}	10^{-9}	10^{-9}
Beam Lifetime [h]	20	15	3 - 10	5
Bunch Distance [μs]	3.8	0.016	0.1	11

(1) H1 determined the total ep cross section for photoproduction events as $\sigma_{\text{ep}}^{\text{Photo}} \approx 11 \mu\text{b}$ [10]. Other physics processes have a much smaller cross section.

(2) LEP at Z^0 resonance energy.

(3) The triggering task at both LHC and SSC is not so much to suppress beam - gas interactions but to select the few 'interesting' events (eg. Higgs production) from an average of 10 to 20 pp collisions *per bunch crossing*.

A = atomic mass of a residual gas nucleon hit by a proton, $A \approx 16$ [13].

Table 2: Comparison between HERA and other colliders [11].

Table 2 compares parameters of current and planned new machines. It demonstrates that HERA not only suffers from the small ep cross-section as compared to the one for

beam - residual gas processes, but that this ratio is further aggravated by the high beam currents necessary to achieve the desired luminosity \mathcal{L} . Beam collisions scale with $R = \sigma_{\text{tot}} \mathcal{L}$ with σ_{tot} being the total ep cross section, whereas beam - beam pipe and beam - gas interactions are proportional to the beam currents. The latter are also proportional to the cross section σ_{Resgas} .

The signal to noise ratio of HERA is not only one of the worst, but the time available for event classification is also minimized due to the short bunch distance of just 96 ns. Furthermore, the unequal collision partners cause the centre of mass system to move relative to the laboratory system for both genuine ep reactions and background, making the event topologies less distinguishable.

Background sources at HERA include:

- Cosmic rays: given the area covered by the H1 experiment (8 m² for the tracker, 28 m² for the calorimeter) and the flux of cosmic ray particles on a horizontal surface of roughly 1.7·10² m⁻²s⁻¹, the rate amounts to roughly 1.4-4.8 kHz. Since their topologies differ strongly from ep collision events, they do not pose a major trigger problem.
- Synchrotron radiation: The electrons and protons travel in independent beam lines. However, at the interaction zones they have to cross each other under an angle of exactly π . To achieve this, the electron beam is bent with a radius of 1360 m over a length of 13.6 m [12]. As this happens just a few meters away from the interaction point, the resulting synchrotron radiation becomes visible in the detectors.
- Proton - gas interactions: Protons may hit residual gas atoms still existing in the vacuum of the beam pipe. The cross section for such interactions is given as $\sigma_{\text{pN}} \approx A^{2/3} \cdot 40 \text{ mb}$ with A being the atomic mass of the nucleon N hit by the proton [13]. These gas interactions are enhanced by the relatively bad vacuum near the ep-interaction zone due to synchrotron radiation induced heating of the beam pipe. Electron beam - gas interactions are negligible due to the small cross section $\sigma_{\text{eN}} \approx 200 \text{ } \mu\text{b}$.
- Proton - beam pipe interactions: Off-momentum protons hit part of the beam pipe structure. This happens mainly at collimator locations upstream (as seen from the protons) from the interaction point. Electron - beam pipe interactions are thought to be of minor importance due to the smaller beam current and better focusing properties of the electron beam optics as well as the much shorter penetration length of the produced shower.

The proton - beam pipe interaction rate was expected to be on the order of 50 kHz at the design luminosity, which compares very well with the measured rate of 225 Hz during the 1992 running period at a total proton beam current of 0.8 mA (0.5% of the design value). The proton-gas interaction rate can be calculated as 1 kHz/m from the observed vacuum of 10^{-9} Torr and at design luminosity. This scales to 2.5 Hz within the interaction region ($|z| < 25$ cm) with the reduced proton beam current. We effectively observed 2 Hz of such events, triggered with the central tracking triggers [3].

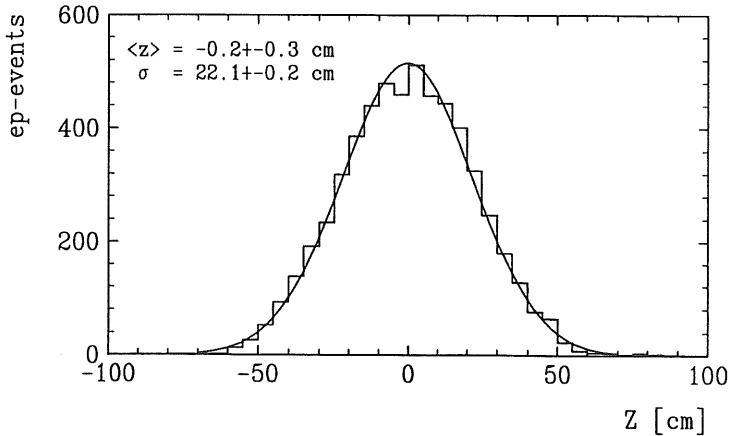


Fig. 4 Vertex distribution along the beam axis for a background free sample of photoproduction events.

Figure 4 shows the vertex distribution along the beam axis for a background free sample of photoproduction events. Clearly, one possible handle for a trigger is the z-coordinate of the event vertex, as none of the background sources would display a similar distribution.

2.2 The H1 trigger scheme

Given the constraints described above, it is obvious that the final event selection cannot be done in a single step. Thus, the H1 detector makes use of a four level trigger scheme in order to minimize dead time. Each subsequent level is only started if a given

event has been accepted by the preceding decision logic. A well-balanced design obeys the rule that the dead time introduced by the trigger level i , $t_{\text{dead}, i} = R_{i-1} \cdot t_i$, is about equal for all levels. Here, t_i is the decision time of level i and R_{i-1} the output rate of the previous stage. Figure 5 gives an overview of the H1 trigger scheme.

To further reduce the overall dead time, the first trigger level (L1), which receives an input rate $R_0 \approx 50 \text{ kHz}$ ¹, makes use of a pipelined design as detailed in appendix A. This allows its decision time to be enlarged to $2.3 \mu\text{s}$ despite the short bunch distance of just 96 ns . A positive L1 decision (*L1-Keep*) stops all pipelines and starts the second trigger level (L2), which introduces a dead time of $20 \mu\text{s}$. Upon an *L2-Keep* signal, the front-end data readout is started. This process requires 1.2 ms . In parallel, a software based level three trigger (L3) operates on the same subset of the event data that was available to L2 (plus the L2 trigger condition). An *L3-Reject* signal can prematurely interrupt the readout process, clear all pipelines and restart the front-end electronics by sending a *Front End Ready (FER)* signal. If no *L3-Reject* occurs, restarting is initiated after completion of the data transfer. With the detector ready again for the next event, a RISC processor farm based level four trigger (L4) works asynchronously on the full event data, selecting events for finally being written to a data storage device [14].

Each trigger level has access to the exact trigger conditions of all lower levels. Hence, the latter can be interpreted as an event classification. Certain critical classes can bypass all or some of the subsequent filtering processes, or invoke special algorithms optimized for particular types of events. Examples are events with much energy deposited in the calorimeter. They are particularly interesting candidates for new or unexpected physics processes and should therefore never be rejected by a higher trigger level. It is furthermore possible to lower thresholds on particular signatures in one of the first trigger levels, if one has good filter algorithms available for them at a higher level.

The length of the pipeline and therefore the decision time available to L1 was kept as short as possible. A lower limit is given by the maximum drift time in the tracking detectors, which is on the order of $1 \mu\text{s}$. Secondly, the sheer geometrical size of the H1 detector structure introduces cable delays, which are also on the order of a few hundred nano-seconds. This had to be considered for the design of the pipeline length since a

¹ The bunch crossing frequency of 10.4 MHz corresponds to the L1 input rate. The defacto rate however, defined by a non-empty detector, is given by the number of background interactions, estimated to be roughly 50 kHz at design luminosity. Even a very primitive trigger could determine the corresponding bunch crossings.

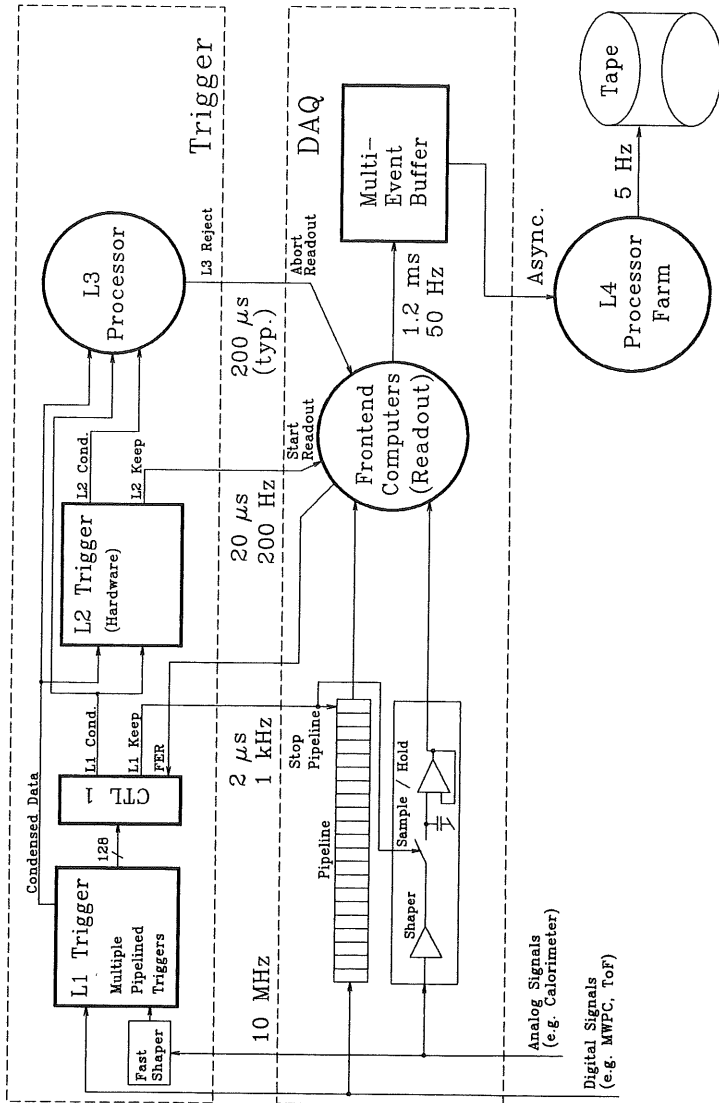


Fig. 5 The H1 trigger concept.

centrally derived trigger decision has to be communicated to the various, spatially distributed subsystems before the corresponding event data reach the end of the respective shift registers.

The main arguments for keeping the pipelines short were their costs - an argument that was certainly true at the time H1 was designed. Given the decrease in silicon costs for electronic circuits, this must be disputed for the upcoming detector designs at LHC and SSC as it has to be weighted against additional costs introduced by making the trigger electronics keep up with the short decision time.

Trigger levels two and three operate on a subset of the event data, prepared by part of the L1 electronics, which extracts information from the various detector subsystems and presents them in a granularity feasible for L2 and L3. An L2 processor can combine information from different subsystems at a much finer level than what is possible in the L1 *central trigger logic* (CTL1, see below).

Both trigger levels one and two were planned as hardware triggers given the tight time constraints of just a few microseconds. However, advances in neural network design in the past few years seem to offer new options for at least L2 [15]. The level two decision time should be long compared to the one of L1, such that algorithms, which are an order of magnitude more complex, become feasible. Favourable times are multiples of 21.1 μs , corresponding to the HERA revolution frequency of 47.3 kHz. The front-end system is then guaranteed to become active again at the same machine bunch number at which it was stopped. Thus, different currents for different machine bunches do not bias luminosity calculations or dead time estimations, which have to take into account the 10 out of the total of 220 bunches stored in the ring, which are purposely kept empty.

The level three trigger is the first completely software controlled stage in the trigger chain. Given its flexibility, it can be used as a test bed for future level two triggers. The decision time is not fixed. It has only to be shorter than the time needed by the front-end processors to completely store an event in the multi-event buffer, as L3 should interrupt this readout process.

The level four trigger rate is determined by the recording speed of the currently used data storage media and explained in table 1. The L4 input rate is limited by the total computer power available in the processor farm, which is mainly a budget constraint.

The ultimate goal would be to run the full event reconstruction program on L4. Secondly, the front-end readout speed is limited to about 50 Hz for 60 kbyte-sized events by the current hardware². An upgrade, which will allow a rate of 200 Hz is under way [9].

	Status Autumn 1992	Design Value
HERA luminosity \mathcal{L}	$1.5 \cdot 10^{29} \text{ cm}^2\text{s}^{-1}$ typ.	$1.7 \cdot 10^{31} \text{ cm}^2\text{s}^{-1}$
Bunches / revolution in HERA	9+1 e ⁻ , 9+1 p (1)	210 e ⁻ , 210 p (2)
L1 trigger rate (deadtime corrected)	10-15 Hz	1-5 kHz
L2 trigger rate	-	50-200 Hz
L3 trigger rate	-	50 Hz
Front end readout	3-10 ms/event typ.	1.2 ms/event typ.
L4 trigger rate / data logging	5-10 Hz	5 Hz
Deadtime	3-15%	9-20%

- (1) One bunch of either beam was not made colliding with its corresponding bunch partner by keeping the latter empty. This allows background investigations using the *empty target* method.
- (2) The HERA circumference corresponds to 220 bunches, of which 10 are always kept empty to allow beam dump magnets to be properly switched on if necessary.

Table 3: Main H1 trigger parameters

Table 3 compares the planned and current operation of the H1 trigger system. During the first running period, neither trigger level two nor three were operational. This was however compensated by the small luminosity delivered by the machine. The low front-end readout speed was partly caused by running programs in debug mode, where much more data needs being processed. The data logging rate was dependent on the number of detector subsystems running.

² A high speed glass fibre vertical interconnection (VMEtaxi) between the otherwise independent VME based front-end systems is used to transfer all subdetector data to the L4 event buffer, on which the processor farm operates.

2.3 The first level trigger

Figure 6 and 7 give an overview over the level one trigger as installed at H1. Various detector subsystems provide *trigger elements*, which are combined in the *central trigger logic* (CTL1) to a common L1 decision (*L1-Keep*). The CTL1 is capable of evaluating almost any arbitrarily complex function of the 128 trigger elements it receives [16].

Powerful handles with good background rejection capabilities include both topological conditions, such as energy flow distributions in the calorimeter, and the reconstruction of the primary event vertex from precise tracking detector information. Level one triggers include:

- Cosmic Scintillator: A large scintillator located below the H1 detector can be used to purposely trigger cosmic ray events for calibration runs.

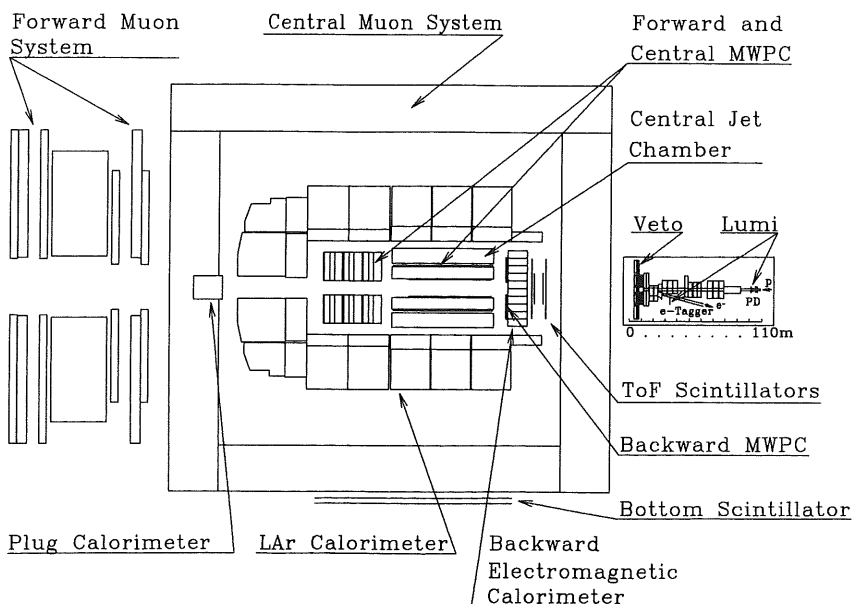


Fig. 6 The detector subsystems included in the L1 trigger.

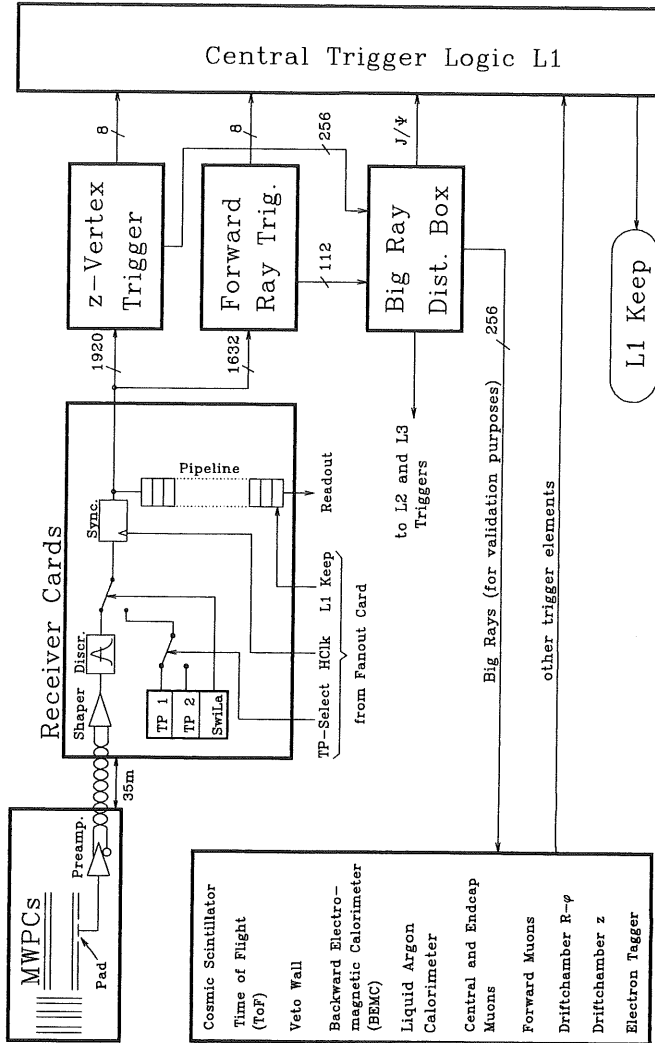


Fig. 7 The first level trigger of H1. The MWPC subsystem with its two independent triggers enlarged. A detailed block diagram of the z-vertex trigger is given in figure 43 on page 77.

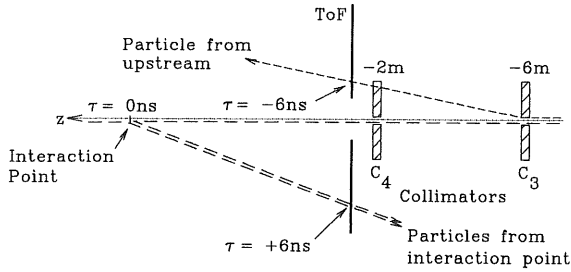


Fig. 8 The ToF trigger determines the primary interaction vertex by measuring the time at which particles traverse a scintillator wall.

- Time of Flight (ToF): A time of flight scintillator wall located upstream (in the proton direction) from the interaction point discriminates proton - beam collimator collisions. Figure 8 shows, that particles originating from ep collisions have to travel a longer distance and therefore arrive $\Delta\tau \approx 12$ ns later at the ToF wall than particles from the collimator locations. Thus, the ToF trigger reconstructs the primary vertex position in the time coordinate.
- Veto Wall: Two further upstream scintillator hodoscopes, which veto proton beam halo.
- MWPC triggers: They are described below.
- Driftchamber R- ϕ Trigger [17]: Information from the Central Jet Chamber (CJC) is used to find charged particle tracks in the R- ϕ projection of the detector. Due to the magnetic field in the tracker, the trajectories form segments of a circle, which should originate from the beam axis, as shown in figure 9. The trigger cuts on this *distance of closest approach* (DCA), thus reconstructs the primary vertex in the R- ϕ projection. It also allows to count the number of tracks found in the 15 ϕ -segments of the CJC.
- Driftchamber z-Trigger (planned) [18]: Using the information of the z-driftchambers, the z-coordinate (along the beam axis) of the primary vertex is reconstructed.
- Liquid Argon Calorimeter [19]: The energy flow in the main H1 calorimeter is measured. Total, missing and transversal energies are calculated, based on energy deposited in groups of calorimeter segments, so called *big towers*, which are combined by the calorimeter front-end electronics. The big tower granularity is shown in figure 10.

- Backward Electromagnetic Calorimeter (BEMC) [20]: Scattered electrons deposit energy in a cluster of scintillator cells. The BEMC trigger sets a threshold on the energy content of such a cluster.
- Central Muon System (Instrumented Iron) [21]: One or more muons in certain areas of the detector can be required for a positive trigger condition. It makes use of the streamer tubes installed in the iron yoke.
- Forward Muon System [22]: Triggers on muons produced under a very small angle ϑ relative to the beam axis.
- Electron Tagger: Triggers on electrons scattered under a very low angle ($\vartheta \leq 5$ mrad) and is used mainly by the luminosity monitoring system, which counts $e p \rightarrow e p \gamma$ events. A coincidence with a γ detector at $z = -103$ m is required for this purpose. The tagger signal however is also independently available to the level one trigger.

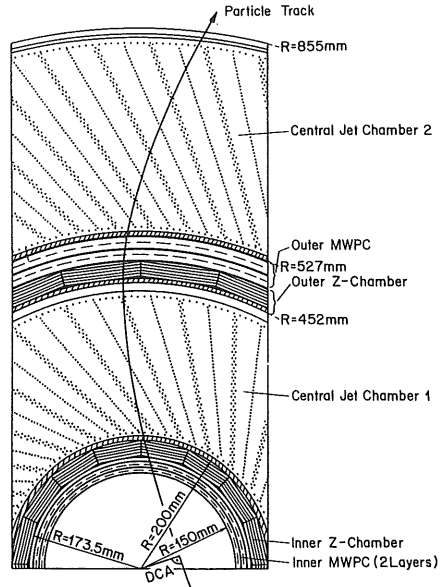


Fig. 9 A cross sectional view of the central trackers. *DCA* is defined as the *distance of closest approach* of a track to the beam axis. It is measured online by the driftchamber $R-\varphi$ trigger.

As an example of a first level trigger, figure 7 shows details of the proportional chamber triggers. Cathode pad signals³ are preamplified directly on the detector and transported to the electronic trailer outside the apparatus. There, the signals are shaped, discriminated and synchronized with the HERA clock on a so-called *receiver card* [23]. The output pulse of the synchronization units are forced to be 96 ns wide. A logical high indicates at least one crossing of the discriminator threshold in the positive direction within the corresponding 96 ns time window.

³ Anode wires are read out for the four layers of the backward proportional chamber.

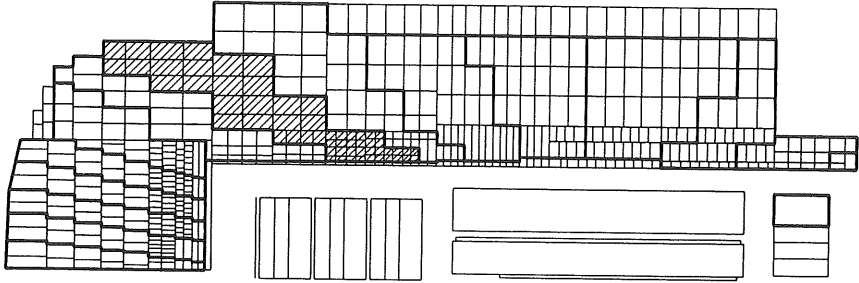


Fig. 10 The calorimeter trigger towers (thin lines) are grouped into big towers (heavy lines) according to the angle ϑ they appear under if seen from the interaction point. One such big tower is hatched for better visibility.

The digitized and synchronized pad signals are stored in a pipeline, such that they can be read out later, should an L1 trigger decision hold the pipeline and *L2-Keep* start the readout. The signals are immediately available to the two triggers operating on them, the *z-vertex trigger* described in this document and the *forward ray trigger*. Each of the two filters delivers eight trigger elements to the central trigger logic CTL1.

The *forward ray trigger* [24] requires a six-fold coincidence between pads of the six MWPCs located in the three super modules of the forward tracker, such that a corresponding particle trajectory has to originate from the anticipated interaction zone of H1. It is then possible to require a certain number of such *roads* for the trigger to accept an event.

Apart from producing the trigger elements, both triggers make MWPC information available to subsequent trigger levels. These so-called *big rays* are discussed in chapter 3.1 and 6.1. Essentially, they mark regions of interest in the ϑ - ϕ plane, as seen by the proportional chambers. To make this information suitable for other triggers, a somewhat coarse 16·16 granularity was chosen. The big rays are not only used by the trigger levels two and three, but also to verify calorimeter and maybe driftchamber trigger information at L1.

3 The *z*-vertex trigger

3.1 Principles of operation

The aim of the *z*-vertex trigger is to reconstruct the primary interaction vertex along the beam axis, the *z*-coordinate, using an algorithm inspired by a software trigger used at the former JADE experiment at the collider PETRA [25]. It operates on the cathode pad signals of two cylindrical multiwire proportional chambers (MWPCs: CIP and COP) [26], situated around the beam axis, as well as one planar chamber (FPC), located in the proton direction from the interaction zone. To suppress the influence of single synchrotron radiation hits, each chamber consists of two independent layers. Table 4 lists their geometrical properties.

The use of a pad readout structure allows the approximative determination of both coordinates φ and z (r) of a particle crossing the barrel (forward) chambers. The design goal of a 16-fold φ -segmentation could only be fully achieved for the COP and the outermost areas of FPC. The 16 innermost pads of FPC as well as those of CIP are staggered in φ by $2\pi/16$ between the two layers. Thus, they form logical pads of the desired φ resolution despite mechanical constraints, which allowed only eight segments per layer. The pads of the two layers of the FPC are also staggered against each other in r for increased resolution.

Figure 11 explains the basic principles of the trigger: a *ray* is defined as the coincidence of four MWPC pads, which can be connected by a straight line in the r - z plane. The number of such rays, which are active for any given bunch crossing, is entered into a 16 bin wide histogram. Each bin is related to the origin of its respective rays along the beam axis. Inevitably, one also finds combinations not originating from a true particle track. However, these fake rays generally produce a flat distribution in the histogram, whereas at the true vertex location a peak is found. Background events do not show this typical peak as they mostly originate from interactions outside the nominal interaction zone (and the histogrammed area).

The pad sizes of the barrel chambers were matched to the anticipated resolution of the vertex determination as shown in figure 12, whereas the forward chamber pad sizes were dictated by the forward ray trigger requirements.

	Inner Barrel Chamber (CIP)	Outer Barrel Chamber (COP)	Forward Chambers (FPC)
Radius: inner	157.0 mm	501.5 mm	167.5 mm
outer	166.0 mm	514.5 mm	750 mm
z-position	-1125 .. 1065 mm	-1107 .. 1065 mm	1451 mm, 1463 mm
Gap width	3 mm	4 mm	4 mm
Pad size	$\Delta z = 36.5$ mm	$\Delta Z = 120.7$ mm	Pad boundaries at: $r_0 = \begin{cases} 167.5 \cdot 1.0778^i, \\ 750 \end{cases}$ with $i=0..19$ (Layer 0) $r_1 = \begin{cases} 167.5, \\ 187.44 \cdot 1.0778^i, \\ 750 \end{cases}$ with $i=0..18$ (Layer 1)
Number of pads per φ -segment and layer	60	18	20
Number of φ -segments (1)	8	16	8 for the inner 16 pads 16 for the outer 4 pads
Number of layers	2	2	2 (+ 4 not used (2))
Tot. number of pads	960	576	384 (+ 768 in unused layers)
z-vertex bin width	$\Delta z_0 = 54.9$ mm		

- (1) The two layers of the eight-fold segmented chambers (chamber areas) are staggered in φ by $2\pi/16$.
- (2) The H1 forward tracker contains three independent super-modules, each equipped with a double-layer proportional chamber. The *z-vertex trigger*, in contrast to the *forward ray trigger*, makes use of the first super-module only.

Table 4: Geometrical properties of the proportional chambers used by the *z-vertex trigger*.

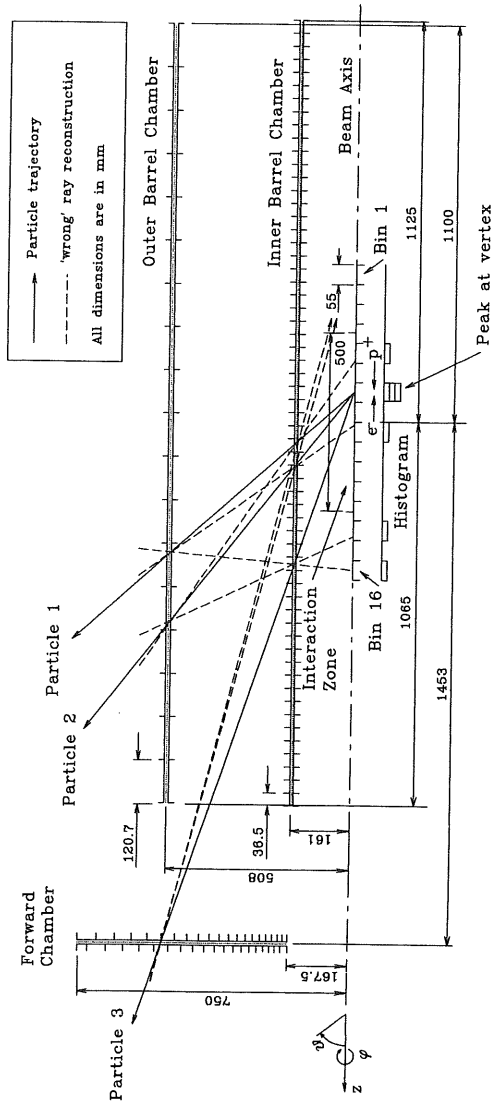


Fig. 11 The z-coordinate of the vertex position is reconstructed by the z-vertex trigger by building a histogram, which displays a peak at the true vertex.

The 16-fold ϕ -segmentation (around the beam axis) of the chambers corresponds to 16 independently built histograms, one for each segment. This is a compromise between suppressing random coincidences and accepting genuine low momentum particle tracks, which should be entered into the histogram. This is further discussed in chapter 3.3.1. Each segment checks a total of 2150 rays.

Once a peak in the histogram is found, assumptions about which reconstructed rays result from true particle trajectories (namely those pointing to the bin containing the peak) can be made. These rays are grouped into the coarser granularity of *big rays*, which is matched to the calorimeter *big tower* granularity (figure 10, p. 26). There are a total of 16 big rays per ϕ -segment, corresponding to 16 regions in \mathcal{V} . A big ray is said to be on if at least one of its contributing rays is on. Consumers of these big rays include:

- L2 and L3 triggers.
- The calorimeter trigger validates big tower energies with the big ray bits. This allows to lower the energy thresholds for the individual big towers. One can then apply a threshold on the number of such validated big towers.
- The $J/\psi \rightarrow \mu^+\mu^-$ trigger quality can be enhanced by asking for a back-to-back topology in the R - ϕ projection of the two μ tracks. This can be achieved by feeding the logical OR of all big rays of one ϕ -segment into a topological unit, which checks for exactly two inputs with $\Delta\phi = \pi$ [27].
- The quality of the driftchamber R - ϕ trigger could be enhanced by validating reconstructed jet chamber tracks with the \mathcal{V} information of the big rays. This however is a non-trivial task as unfortunately the jet chamber has a 30-fold ϕ -segmentation not matching any other H1 subdetector.

The big rays are enabled whenever there is a non-empty z-vertex histogram and do not require a peak to be significant to any criterion. This is important for combined triggers using big rays for validation purposes only. If a significant peak was required, the 'validated' trigger would in most cases be logically identical to a non-validated function in coincidence with the z-vertex trigger. This combination however is realized in CTL1 even without the additional logic required for the big rays.

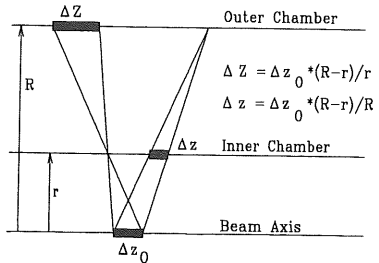


Fig. 12 The pad sizes of both the inner and outer barrel chamber (CIP and COP) are matched to the anticipated vertex resolution Δz_0 of the z-vertex histogram.

Figure 13 shows an electron-tagged event from the first HERA running period, which was also accepted by the z-vertex trigger according to the peak significance criteria described below. A proton - beam pipe interaction with an obvious upstream vertex is shown in figure 14. It is rejected by the trigger.

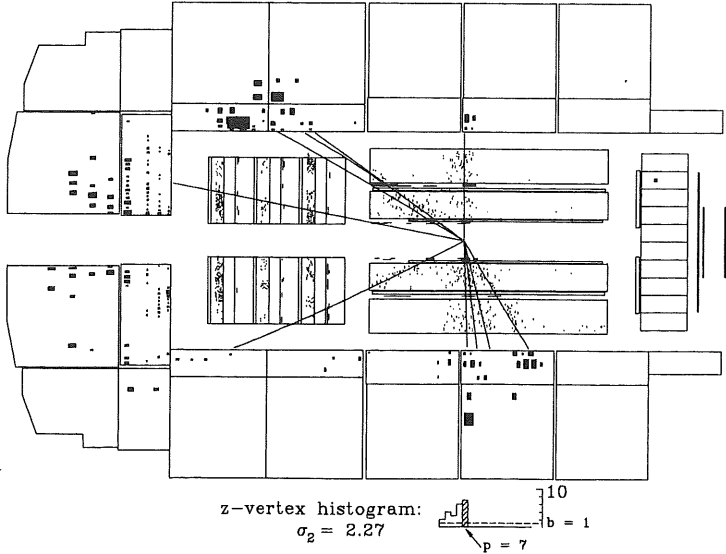


Fig. 13 This electron-tagged two jet event is clearly accepted by the z-vertex trigger with $\sigma_2 = 2.27$ (eq. (2), p. 32).

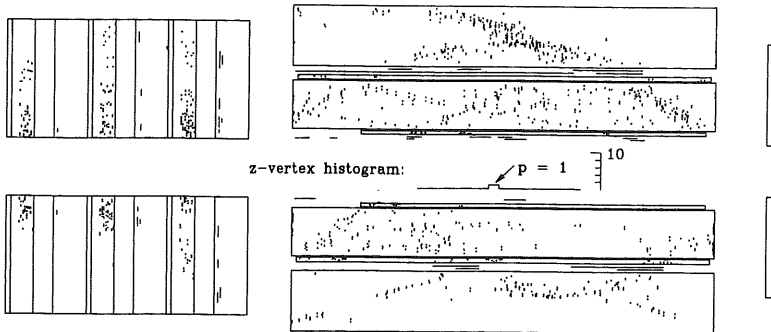


Fig. 14 A proton - beam pipe interaction with a clear upstream vertex is rejected by the z-vertex trigger.

3.2 Peak significance criteria

The hardware is very flexible in adapting to almost any imaginable significance criterion for the peak in the z-vertex histogram by making use of a large RAM lookup table as described in chapter 4.5. A peak is said to be significant, if

$$\sigma_1 = \frac{p-b}{\sqrt{p+s^2}} > x_1 \quad (1)$$

with p the content of the peak bin j , b the average number of entries in all other bins, and s the error of b , $s^2 = (\sum c_i^2 - nb^2) / (n^2-n)$. c_i is the number of entries in bin $i \neq j$, $n = 15$ for our 16 bin wide histogram. x_1 is a freely selectable parameter.

The data displayed in figure 15 indicates, that $p \gg s^2$ holds. Therefore, we can simplify equation (1) to:

$$\sigma_2 = \frac{p-b}{\sqrt{p}} > x_2 \quad (2)$$

which is much easier to implement in hardware as it avoids evaluating s^2 . Equation (1) would require an expansion as described in chapter 6.2. The parameter x_2 is typically chosen to be 1.5.

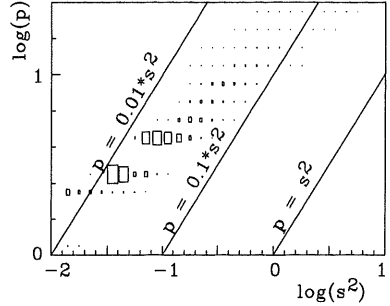


Fig. 15 Data recorded on a POT (production output tape) show that $p \gg s^2$.

The significance criterion has been adapted to the particular requirements of different classes of physics processes. Some events with a clear signature of just two muons for example are best triggered by a coincidence between the H1 instrumented iron (muon) trigger and a histogram with all entries clustered in no more than three adjacent bins [28].

Equation (2) can be interpreted as a cut in a p versus b plane. It can also be arbitrarily defined such as to achieve best possible distinction between a desired event class and background. Such an investigation has been done for heavy quark events using extensive Monte Carlo simulations. As a result,

$$\alpha_3 = \frac{\sqrt{p-2.5}}{b+1/15} > 1.4 \quad (3)$$

was found to be an optimum selection criterion [29]. It should not be interpreted in any other way but in comparing the trigger efficiency for the selected event class with its background rejection power.

It is usually desirable to reject events independently of their peak significance according to any of the above formulae, if the peak bin j is at either end of the histogram. These bins correspond to vertex locations outside the anticipated interaction zone of $|z_{\text{vertex}}| < 33$ cm (figure 4, p. 17). Furthermore, events with two or more bins displaying the same number of entries p should be rejected, especially if these bins are non-adjacent. Coherent noise within the H1 detector system usually leads to an unreasonably high number of fired MWPC pads. Such pseudo-events can be vetoed by requiring $p + b < x_3$ with x_3 large enough.

Given the short bunch crossing distance of just 96 ns at HERA, it is important to uniquely determine the bunch crossing number for any event triggered. As this is not possible with all level one triggers, some of them have a time resolution of several clock cycles, a so-called *weak* t_0 information is required. A non-empty histogram, $p > 0$, is a good candidate, since the MWPCs involved have a sufficiently good intrinsic time resolution as shown in figure 30 on page 56. This condition is then required in coincidence with another trigger.

3.3 Trigger acceptance

Acceptance calculations of the z-vertex trigger for any given class of physics events are non-trivial. The response is not solely understandable by looking on the track multiplicity and their spatial distribution for a given event, since we make use of a *statistical* criterion, namely the significance of a peak in a histogram. It contains by definition a great number of entries caused by random coincidences, which again depend also on the noise situation. This is opposed to what many other known track triggers do, which essentially search *good* tracks according to some criteria. An example for the latter is the driftchamber R- ϕ trigger [17], which requires a certain number of reconstructed tracks with a DCA below a given cutoff parameter. Noise or unlucky

geometrical combinations of many independent track segments may produce fake triggers, but can hardly cause any inefficiencies. Mostly, the latter are directly correlated to single wire inefficiencies.

For a better understanding of the trigger a detailed simulation of the MWPCs is needed. The acceptance for a given track is both subject to some geometrical constraints and to the efficiency and crosstalk of the chambers measuring it. Once the response to single tracks is understood and a realistic noise simulation is available, the trigger efficiency can be estimated by applying this knowledge to Monte Carlo simulated events.

3.3.1 Geometrical constraints

Figure 16 shows the geometrical track acceptance for infinite momentum tracks. The z-vertex histogram covers an area between -440 and 440 mm in z. The trigger is usually configured such that only histogram peaks within bins 3 to 14 lead to a positive output. The acceptance limit in ϑ is slightly dependent on z_{vertex} according to $\tan(\vartheta_L) = r_L / (z_L - z_{\text{vertex}})$ with r_L and z_L being the limiting radius and z-position respectively.

Figure 16 also shows the pad boundaries of CIP and COP - and thus the rays formed by the central chambers. Each ray is uniquely related to the histogram bin corresponding to $z = (z_{\text{min}} + z_{\text{max}})/2$. For the calculation of the displayed boundaries, the average radius of the two layers of each chamber was used for r_L . A *ray* however is defined as the coincidence of four pads of four layers using the *exact* anode wire position for each chamber, as shown in the inset. The number of rays examined by the trigger is therefore roughly three times as high as the drawing suggests. All rays covering a non-empty area in the z- ϑ plane are tested.

For small angle tracks, this is obviously necessary. A crossing angle of $\vartheta = 26^\circ$ corresponds to a particle travelling 18 mm or half a pad in the z-direction between the two layers of the CIP. For tracks with a larger ϑ , as shown in the inset of figure 16, the projections of the pads onto the ϑ -z plane are much closer together. As shown below, the charge deposited on the cathode pads is however negligible already some 3 mm away from the trajectory intersection with the wire plane (figure 20, p. 39). Thus, particles crossing one chamber close to a pad boundary do not necessarily fire the directly corresponding pad in the other layer plane but its neighbour.

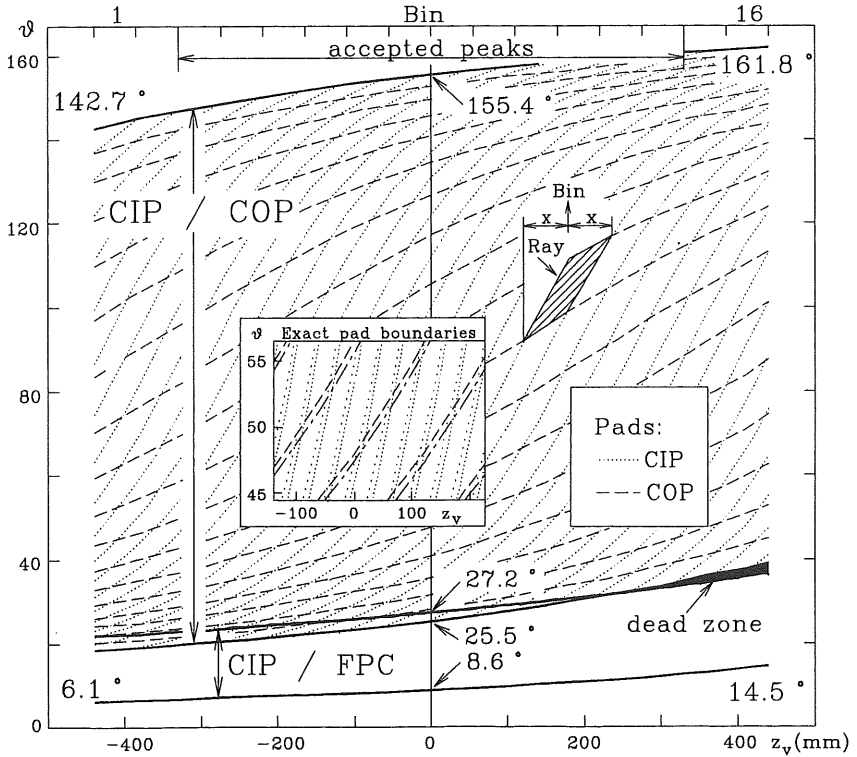


Fig. 16 The geometrical acceptance of the z -vertex trigger for infinite momentum tracks is limited by the MWPC dimensions only. A ray defines an area in the ϑ - z plane and leads to a histogram entry in the bin corresponding to its z -position.

Each ray can be disabled independently through programmable registers (chapter 4.2), such that looser requirements could be chosen any time, which might be desirable in conjunction with the *3-out-of-4* option available for the ray building. One might also want to disable double counted rays in the small area around $\vartheta = 20^\circ$, which is covered by both central (CIP/COP) and forward (CIP/FPC) rays. The dead zone around $\vartheta = 37^\circ$ with z outside the anticipated ep interaction zone however cannot be recovered. It corresponds to a small gap between COP and FPC.

For low momentum tracks the influence of the magnetic field has to be considered, which leads to additional geometrical constraints. The field value is 1.2 T parallel to the

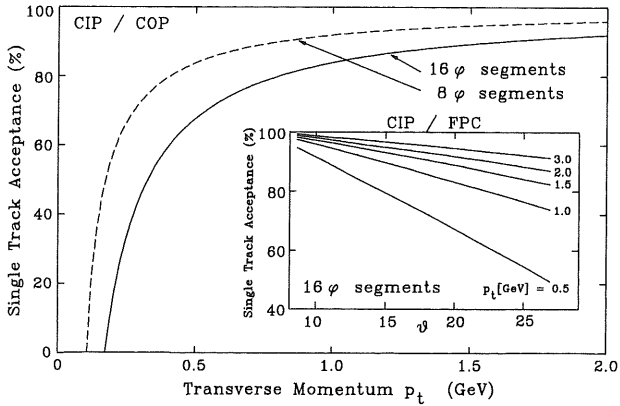


Fig. 17 Low momentum tracks suffer from a lower acceptance due to the ϕ -segmentation of the z-vertex trigger, which is programmable to be either 8 or 16-fold.

beam axis. The trajectory of a charged particle therefore describes a circle in the R- ϕ projection and thus has a certain probability of crossing a ϕ -segment boundary of the trigger. Such tracks do not enable any rays as the z-vertex histogram is independently built for each segment. The resulting acceptance, plotted in figure 17, for such particles is dependent on the transverse momentum p_t , the radii at which the chambers are crossed and the segmentation of the trigger. The crossing radius is a function of ϕ for tracks passing through CIP and the forward MWPCs. The mathematics of these cuts are explained in appendix C.

The R-z projection of a finite momentum track, which follows a helix in three-dimensional space, is a sine curve rather than a straight line as anticipated by the list of valid rays for the trigger. Because of this, the radii, and thus the pads, at which the forward MWPCs are crossed, are different to where an infinite momentum track would cross the chambers. It would still activate a combination of pads which form a ray, but the

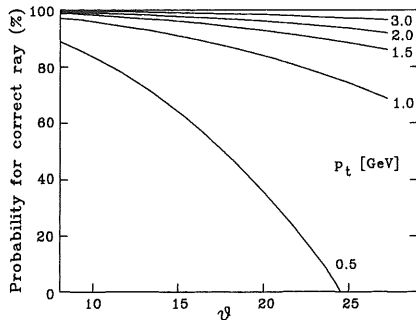


Fig. 18 Very forward oriented particle trajectories do not always enable the same ray as an infinite momentum particle would do.

z-coordinate associated with this ray - assuming it to be fired due to an infinite momentum particle - is smaller than where the true particle originated from. As a result, the bin associated with this ray may not always reflect the true vertex position. Figure 18 shows the probability of activating the same ray as an infinite momentum track would do, as a function of ϑ and p_t .

For the same reason, the crossing coordinate of a central track through CIP and COP may be shifted in z at the radius of the COP. The probability to fire the same ray as an infinite momentum track is above 80% for $p_t > 0.5$ GeV and above 95% for $p_t > 1$ GeV. Thus, this effect is negligible compared to the low energy cutoff discussed above and shown in figure 17 if the φ -segmentation of the z -vertex trigger is chosen to be 16-fold.

3.3.2 Chamber response to charged particles

The table of valid rays suggested in the previous chapter assumes perfect chambers. For any given track segment crossing a chamber, exactly one pad is assumed to have fired, namely the one positioned opposite the intersection of the track with the anode wire plane. This idealistic picture only holds for tracks travelling almost perpendicularly to the chamber and crossing it close to the centre of a pad. In the following, we shall deduce which pads are activated by an arbitrary track segment by calculating the charge deposited on any given pad by that track.

An electrostatic point charge Q sitting on the anode wire plane at $(y,z) = (0,0)$, as shown in figure 19(a), induces a charge density $\sigma(y,z)$ on the cathode plane at a distance l from the anode [30]:

$$\sigma(y,z) = -\frac{Q}{2\pi} \sum_{n=0}^{\infty} (-1)^n \frac{(2n+1)l}{((2n+1)^2 l^2 + y^2 + z^2)^{3/2}} \quad (4)$$

We now consider a particle traversing the chamber under an angle ϑ to the wire plane (figure 19(b)). The primary ionisation along the trajectory produces electrons, which drift towards the anode wire within about 20 ns. The total charge involved in this process is negligible. Only very close to the wires, an avalanche of electrons is generated. We shall neglect the dynamics of this gas amplification process, which typically takes less than 1 ns and increases the charge by a factor of roughly 10^4

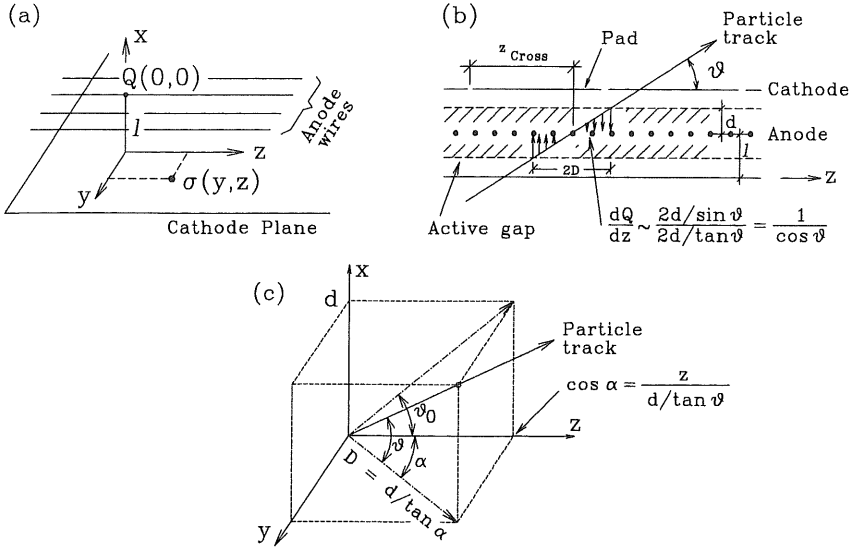


Fig. 19 (a) Equation (4) calculates the charge density $\sigma(y,z)$ on the cathode plane. (b) The primary ionisation is assumed to take place only within an active gap $d \leq l$ (Equation (5)). (c) A particle including an angle α to the direction of the anode wires can be projected onto the (x,z) plane (Equation (9)).

to 10^5 [31]. The short duration makes it invisible due to the much larger time constants of the readout electronics.

Assuming that primary ionisation only takes place in an active zone $d \leq l$, the charge produced by such a particle is proportional to $2d/\sin(\vartheta)$ and homogeneously distributed over a distance $2d/\tan(\vartheta)$ along the projection of the trajectory to the anode wire plane⁴. Choosing the coordinate system such that the particle travels parallel to the z-axis leads to a charge Q_{Pad} deposited on a given pad as:

$$Q_{Pad} = \frac{1}{\cos(\vartheta)} \int_{Pad} \int_{-D}^D \sigma(y,z-u) du \quad (5)$$

⁴ Appropriate corrections can be performed for particles *not* travelling through the entire active zone of a chamber due to decay processes.

with $D = d/\tan(\vartheta)$. A pad is said to have fired if the charge, deposited by all particle tracks crossing the chamber close to it, is above a given threshold T .

Equation (5) has been shown to adequately describe the number of fired pads for an electron test beam crossing the CIP in the centre of a φ -segment under $16^\circ < \vartheta < 45^\circ$ with z parallel to the chamber axis [26]. Q_{Pad} is plotted in figure 20 as a function of z_{cross} , the distance between the track intersection with the anode wire plane and the cathode pad boundaries (figure 19(b)).

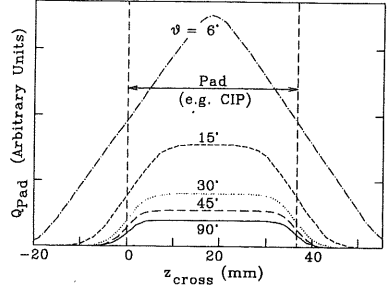


Fig. 20 The charge Q_{Pad} deposited on a given cathode pad is a function of both the intersection z_{cross} of the particle track with the anode wire plane (see figure 19) and the angle ϑ included between them.

Applying (5) to Monte Carlo simulated events however is impractical, as it involves lengthy integrations over each pad for every track segment crossing one of the chambers⁵. It is therefore desirable to subdivide the calculations involved for Q_{Pad} into three steps:

- Neglecting the φ -segmentation of the MWPCs, the charge deposited on each section (pad) along z is calculated.
- Secondly, disregarding the pad structure along z , the charge is distributed over all φ -segments.
- The sum of all charges is equal for both the above steps. The charge per physical pad is estimated by applying the φ distribution as a weight factor to the z -distribution.

This approach allows integrating (4) over y :

$$\sigma(z) = \int_{-\infty}^{\infty} \sigma(y, z) dy = \frac{-Q}{4l} \cosh^{-1} \left(\frac{\pi z}{2l} \right) \quad (6)$$

The charge deposited on one section along z is then calculated as:

⁵ An average event with reasonable activity in the H1 tracker easily contains 50 such track segments!

$$Q_z = \int_{z_{\min}}^{z_{\max}} Q_0(z, \vartheta_0) dz \cdot \frac{\sin(\vartheta_0)}{\sin(\vartheta)} \quad (7)$$

with z_{\min} and z_{\max} the pad boundaries,

$$Q_0(z, \vartheta_0) = \frac{1}{\cos(\vartheta_0)} \cdot \int_{-D}^D \sigma(z) dz = \left[\frac{Q}{\pi \cos(\vartheta_0)} \arctan \left(\exp \left(\frac{\pi(z-z_0)}{2l} \right) \right) \right]_{z_0=-D}^{z_0=D} \quad (8)$$

and assuming that the track crosses the chamber under an angle ϑ . Its projection onto the wire plane is not necessarily parallel to the z -axis, but includes an angle⁶ α . ϑ_0 is the projection of ϑ onto a plane perpendicular to the wire plane and parallel to z (figure 19(c)):

$$\vartheta_0 = \arctan \left(\frac{\tan(\vartheta)}{\cos(\alpha)} \right) \quad (9)$$

This method greatly reduces computing time as only one to six one-dimensional integrals (7) have to be evaluated. Pads further away than about 20 mm from the track intersection point with the anode wire plane need not be considered according to figure 20.

The charge deposited by a heavy⁷ particle scales with the energy loss of that particle in a medium, calculated from the Bethe-Bloch formula [32]:

$$-\frac{dE(\eta)}{dx} = \frac{D_{BB} \rho Z z^2 (\eta^2 + 1)}{\eta^2 A} \cdot \left(\ln \left(\frac{2 m_e c^2 \eta^2}{I} \right) - \frac{\eta^2}{\eta^2 + 1} - \delta(\eta) - \frac{C(\eta)}{Z} \right) = \frac{\bar{\Delta}(\eta)}{x} \quad (10)$$

with $D_{BB} = 4\pi N_A r_e^2 m_e c^2 = 0.3070 \text{ MeV} \cdot \text{cm}^2/\text{g}$,
 $\eta = \beta\gamma = p/mc$, with p the momentum and m the mass of the interacting particle,
 z its charge,

⁶ Equation (7) can be shown to be numerically equivalent to (5) for arbitrary α if φ -segment pad boundaries are neglected.

⁷ Equation (10) must be corrected appropriately for electrons, which have the same mass and are indistinguishable from the hit particles, namely the atomic electrons of the chamber gas. Secondly, one must take into account energy loss due to bremsstrahlung.

Z and A the charge and mass number of the chamber gas,
 ρ its density,
I its mean excitation potential, $I \approx I_0 \cdot Z$ with $I_0 = 12 \text{ eV}$,
 $\delta(\eta)$ and $C(\eta)$ phenomenological functions correcting the formula
for very high (low) values of η (so-called *density* and *shell*
corrections)
and $\bar{\Delta}(\eta)$ the mean energy loss per unit length.

Equation (10) describes the *mean* energy loss suffered by charged particles. The actual energy loss $\Delta \sim Q$ however is statistically distributed according to a function $f(x, \Delta, \bar{\Delta}(\eta))$. f has been calculated in the literature for various thicknesses of the absorber. The distinguishing parameter is the ratio $\kappa(\eta, x) = \bar{\Delta}(\eta)/W_{\max}$ with $W_{\max} = 2m_e c^2 \eta^2$ the maximum energy transfer in a single collision between the incident particle with mass $M \gg m_e$ and an atomic electron, and $x = 2d/\sin(\vartheta)$ the path length within the active gap of the chamber. In our case, κ varies between 1.5 and 0.01 for $\eta < 1$ and $\vartheta > 6^\circ$. For $\eta > 1$, one finds $\kappa < 0.01$, in which case Landau's theory can be applied for the evaluation of f . It is then [33]:

$$f(x, \Delta, \bar{\Delta}(\eta)) = \frac{1}{\pi \cdot \bar{\Delta}(\eta)} \cdot \int_0^{\infty} \exp(-u \ln u - u \lambda) \sin(\pi u) du \quad (11)$$

with

$$\lambda = \frac{1}{\Delta} \cdot \left(\Delta - \bar{\Delta} \left(\ln \bar{\Delta} - \ln \left(\frac{(1 - \beta^2) I^2}{2mc^2 \beta^2} + \beta^2 \right) + 0.423 \right) \right) \quad (12)$$

3.3.3 Ray multiplicities

Adapting equation (7) to real chambers is done by modifying both the active gap d and the threshold T such that isolated rays, rays with no other activity in the chamber sufficiently close to them, display the simulated efficiency. Both d and T are functions of the chamber gas used, the high voltage applied and the readout electronics configuration. Thus, they may not only differ for each individual chamber, but d may also depend on the φ -segment, as the high voltage is separately controllable for each segment. T may even be different for each readout channel, each pad.

Fitting all these parameters is of course a lengthy procedure. Thus, we shall discuss the influence of them on the trigger performance in this chapter. Comparing ray definitions according to figure 16 (p. 35) and charge distributions caused by traversing charged particles as shown in figure 20 (p. 39) make it obvious, that only few trajectories will fire *exactly* one ray. Some, traversing a chamber under large angles ϑ close enough to a pad boundary, distribute their charge onto two pads in such an unfortunate way that none of them will fire. Others allow more than one pad to fire due to their small crossing angle ϑ . Consequently, the number of rays activated by a given particle track may be different from one.

Figure 21(a) shows the expected ray multiplicity as a function of ϑ for various thresholds T for infinite momentum tracks, thus omitting geometrical acceptance cuts as discussed in chapter 3.3.1. Effects from equations (10) and (11) are disregarded. T is compared to the integrated charge $Q_{\text{tot}} = \sum(Q_{\text{pad}})$ deposited by a track traversing a chamber under $\vartheta = 90^\circ$ according to equation (5) (p. 39). d is chosen to be 70% of the chamber gap width l . Figure 21(b) compares different active gap widths d for a constant $T = 60\%$. Figure 21(c) and (d) correspond to (a) and (b) with a global *3-out-of-4* option enabled although all chambers were kept fully operational. One concludes that d and T are only independent parameters for $\vartheta < 40^\circ$ and $\vartheta > 140^\circ$. The multiplicity distribution along z is flat.

Thresholds $T > 50\%$ lead to inefficiencies at pad boundaries, as none of the two adjacent pads receive enough charge. Figure 22(a) shows the distribution of rays suffering from this effect for $T = 80\%$. Similarly, even infinite momentum tracks distribute their charge onto two φ -segments if they come close enough to a boundary. Tracks with a small Q_{tot} , namely those with $\vartheta \approx 90^\circ$, may thus not fire their corresponding ray. As shown in figure 22(b) this leads to dead zones in φ , which may cover as much as 7% of the entire circumference. Of course, the important parameter for this effect is not so much the angular distance $\Delta\varphi$ of a trajectory from the segment boundary but its absolute distance. Thus, these inefficiencies should primarily be discussed in terms of T_{CIP} , the thresholds applied to CIP only. One also notes, that this effect is caused by the integrating property of the chamber pads itself and therefore cannot be minimized by altering the φ -segmentation of the trigger electronics alone. This is opposed to the low energy cutoffs discussed in chapter 3.3.1.

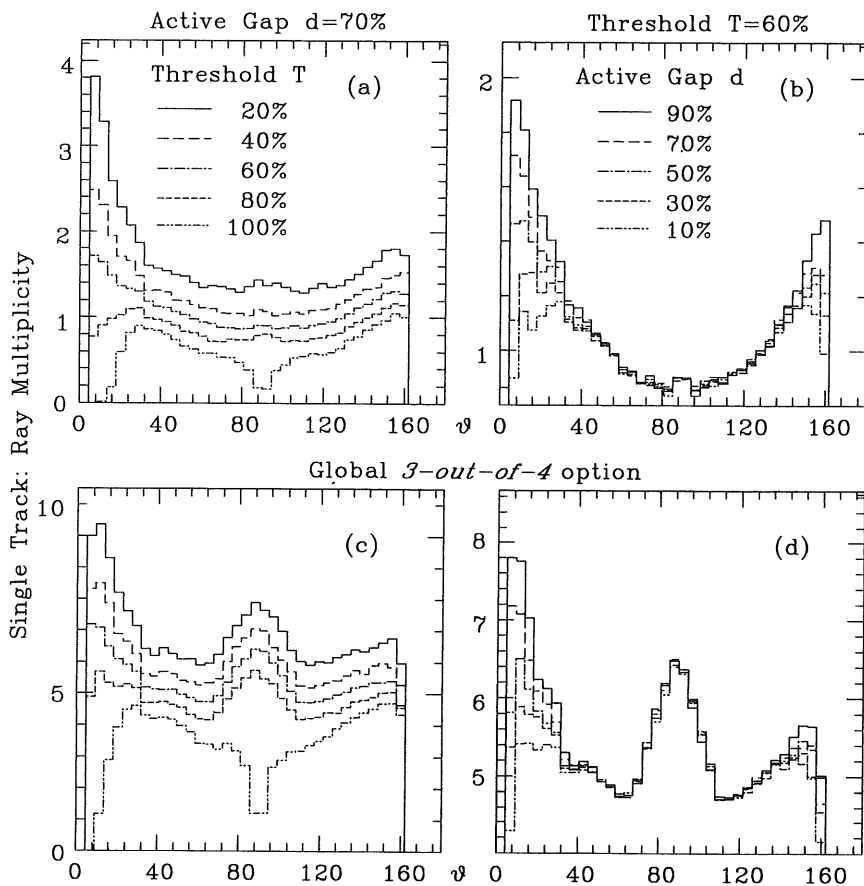


Fig. 21 The number of rays enabled by a single particle track as a function of ϑ is dependent on both the digitization threshold T of the pad readout chains (a, c) and the active gap width d of the chambers (b, d). Requiring only 3 out of 4 pads for each ray increases the multiplicity by roughly a factor of five (c, d).

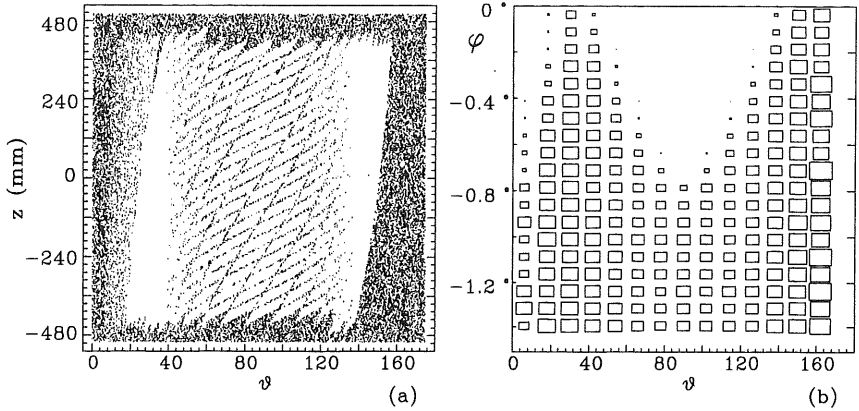


Fig. 22 For a threshold $T = 80\%$ ($> 50\%$), inefficiencies occur at both pad (a) and ϕ -segment (b) boundaries. (a) shows the distribution of rays in the ϑ - z plane, which have not enabled a single ray. The pad boundaries calculated in figure 16 (p. 35) become visible. (b) displays single ray multiplicities as a function of ϑ and ϕ . For $\phi < -1^\circ$, the multiplicity is the same as shown in figure 21(a). For $\phi > -1^\circ$, inefficiencies occur around $\vartheta = 90^\circ$ and in the forward direction.

The above seems to suggest a great ϑ -dependence of the trigger efficiency. However, most physical event classes display a jet structure. These jets fragment into a relatively small spatial area, which increases the likelihood of 'wrong' entries into the z -vertex histogram from there. The number of such background entries is of course also dependent on ϑ , since it is a function of the number of fired pads. To test these dependencies independently, artificial jet-like bundles of tracks were constructed:

- A jet axis was chosen randomly in space (z_{jet} , ϑ_{jet} and ϕ_{jet}).
- The jet multiplicity n was varied between 1 and 7.
- The first three tracks were forced to be on a cone with an opening angle of 10° around the jet axis.
- The remaining tracks were allowed to be inside this cone.
- All tracks were stiff, corresponding to infinite momentum trajectories.
- Equations (10) and (11) on page 41 were again disregarded.

Figure 23(a) shows the average number of peak bin entries for such 'jets' as a function of ϑ and n . The threshold parameter was set to $T = 80\%$ and the active gap width was chosen as $d = 0.7l$. As opposed to figure 21, the distributions do not peak at $\vartheta_{\text{jet}} \approx 8^\circ$ and 160° but at $\vartheta_{\text{jet}} \approx 35^\circ$ and 130° . This is an artefact of the construction

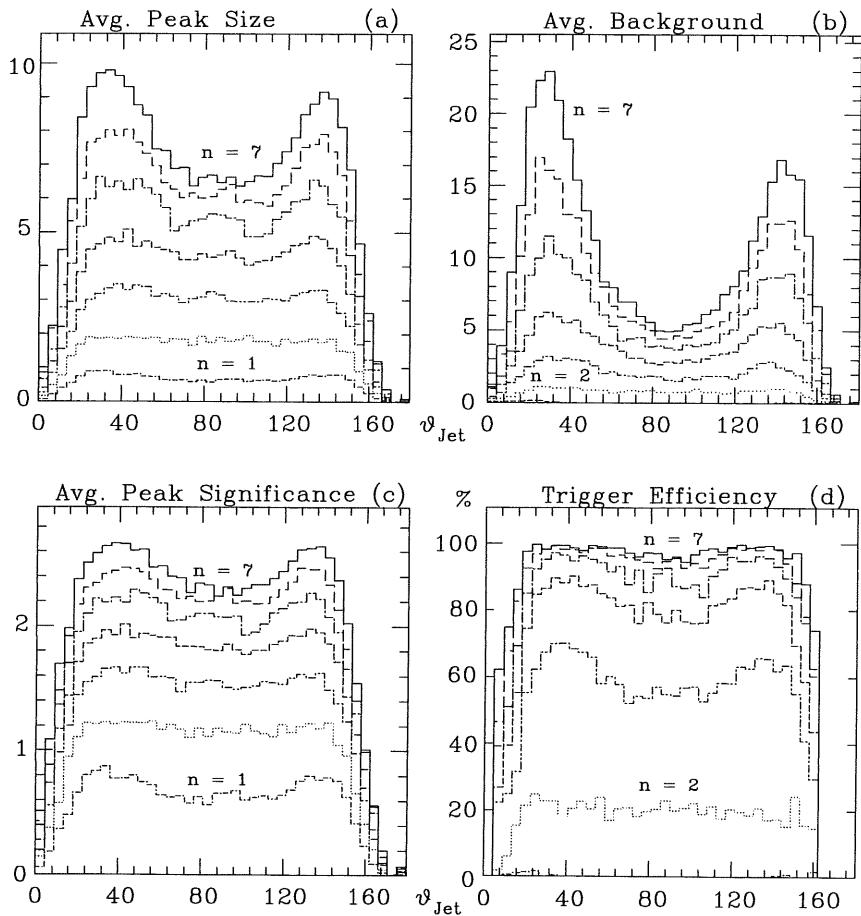


Fig. 23 The peak size (a) and number of background entries (b) in the z-vertex histogram for jet-like bundles of tracks are both dependent on ϑ_{Jet} and the number of tracks $n = 1..7$ in the 'jet'. However, the average peak significance σ_2 (c) and trigger efficiency for $\sigma_2 > 1.5$ (d), with σ_2 according to equation (2) on page 32, are almost independent of ϑ_{Jet} .

rules for the 'jets' as some of their tracks may fall outside the geometrical acceptance region of the trigger as shown in figure 16 on page 35. Thus, the jet actually has a higher multiplicity n than the one seen by the trigger. Figure 23(b) shows the sums of all but the peak bin entries, which display about the same ϑ_{jet} dependence as the peak sizes. Consequently, it is not surprising that the average peak significance σ_2 according to equation (2) (p. 32) is largely independent of ϑ_{jet} , which is also true for the trigger efficiency with $\sigma_2 > 1.5$ as the trigger criterion. This is shown in figure 23(c) and (d). A larger dependence on ϑ_{jet} is only seen for the very high threshold $T = 100\%$ for $n \leq 3$.

The peak position of 91% of the generated 'jets' with a non-empty histogram agreed with the bin corresponding to the vertex z_{jet} . Only 3.3% showed an offset of more than one bin. 97.7% of the 'jets' with a badly reconstructed vertex however had either $\vartheta_{\text{jet}} < 40^\circ$ or $\vartheta_{\text{jet}} > 120^\circ$. The misreconstruction is obviously correlated to the larger number of histogram entries in these ϑ ranges.

Figure 24 compares average peak significances and trigger efficiencies for various settings of the threshold T . ϑ_{jet} was chosen to be between 31.5° and 135° , the plateau region of figure 23(c) and (d). The good stability against changes in T can be explained by the fact, that the average single track multiplicity as shown in figure 21 is mostly

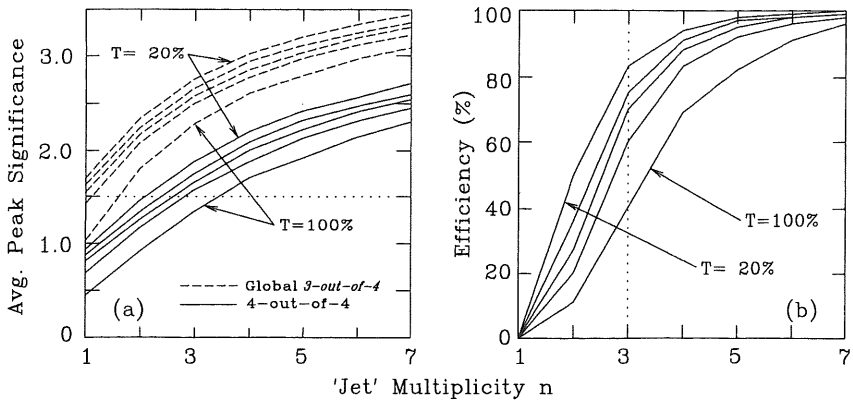


Fig. 24 The average peak significance (a) and trigger efficiency (b) are more dependent on the number of tracks in a 'jet' than on the digitization threshold T , which was set to 20, 40, 60, 80 and 100%.

greater than one. One can conclude that a particle trajectory which has fired *at least one* ray, is treated by the trigger almost independently of the other parameters such as T , d , n , ϑ_{jet} and so on. This is further underlined by the fact, that enabling the global *3-out-of-4* option increases the trigger efficiency. Unfortunately, the low energy tail described by equations (10) and (11) (p. 41) for real particles may lead to inefficiencies of the chambers and thus to tracks *not* seen by the trigger. This is especially true for $\vartheta \approx 90^\circ$ or $\vartheta < 15^\circ$, as the latter tracks cross the forward MWPCs under angles close to 90° , thus depositing only minimal energy.

3.3.4 The influence of incoherent noise

So far, we have assumed that the MWPC hit pattern is only dependent on the charged tracks crossing the chambers. With the high amplification necessary for the chamber signals, it is however not unlikely that they are susceptible to electrical noise. We also expect about 1% of all pads to fire due to converting photons from synchrotron radiation.

In this chapter, we will investigate the influence of such disturbing effects on the trigger performance. We shall restrict ourselves to incoherent noise in the sense that the distribution of the fired pads is randomly scattered throughout the chambers.

With no ep interaction taking place, the average number n_r of rays detected by the z-vertex trigger, that is the total number of histogram entries, is given by $n_r = p^4 \cdot n_T$ with n_T being the total number of rays investigated, namely 2150·16 φ -segments, and p the probability for a pad to have fired due to noise. $n_r \geq 1$ is only true for $p > 7.3\%$, which corresponds to 141 noisy pads out of the total of 1920 used as trigger input. Such a high noise rate is unrealistic under proper operating conditions. A typical H1 data sample accepted by the L1 trigger cocktail shows an average MWPC hit multiplicity of 56 pads with only about 3.5% of all events containing more than 200 hits. Nevertheless, we shall discuss noise rates up to $p = 35\%$ in the following, to get a feeling for the trigger response.

Figure 25(b) and (c) shows the trigger efficiency for DIS and $c\bar{c}$ ⁸ events respectively. It increases from an initial, sample dependent value to about 88% for $p = 35\%$. An eventwise analysis reveals that in all cases at least 87% of those events triggered with noiseless chambers survive the perturbation. The increase in the overall acceptance is therefore caused mainly by events, which would not have triggered without added noise. Their acceptance curve roughly follows the one for pure random hit patterns (figure 25(c)).

Although the average number of histogram entries increases from 20.6 to 776 with the peak size growing from 6.0 to 65.7 for the $c\bar{c}$ sample, if p goes from 0% to 35%, a good correlation between the z -coordinate of the reconstructed vertex and the peak bin location is maintained. This is shown in figure 25(a), which plots the distance between the fitted vertex and the peak position for events that have triggered with clean chambers. No noise however has been added to the driftchambers needed for reconstructing the event vertex z_{Fit} .

All the above simulations have been made with the *3-out-of-4* option (equation (18), p. 78) disabled. Enabling it would of course increase the number of noise induced rays found by the trigger and thus aggravate the tendencies described here.

3.4 Monte Carlo simulations of trigger efficiencies

With HERA being a precision instrument to investigate the structure of the proton, deep inelastic scattering processes (DIS) of the electron on one of the quarks present in the incoming proton are of particular interest (figure 26). They can be discussed in the two kinematical variables x and Q^2 . x is the fraction of the proton momentum carried by the struck quark and Q^2 is the square of the four momentum transfer between the electron and the quark. HERA gives access to an entirely new area in the x - Q^2 plane, which was not covered by previous fixed target experiments. Especially the region of very low values x and intermediate Q^2 give us more insight in the structure of the proton.

⁸ The $c\bar{c}$ sample is the same as the one discussed in chapter 3.6.2.

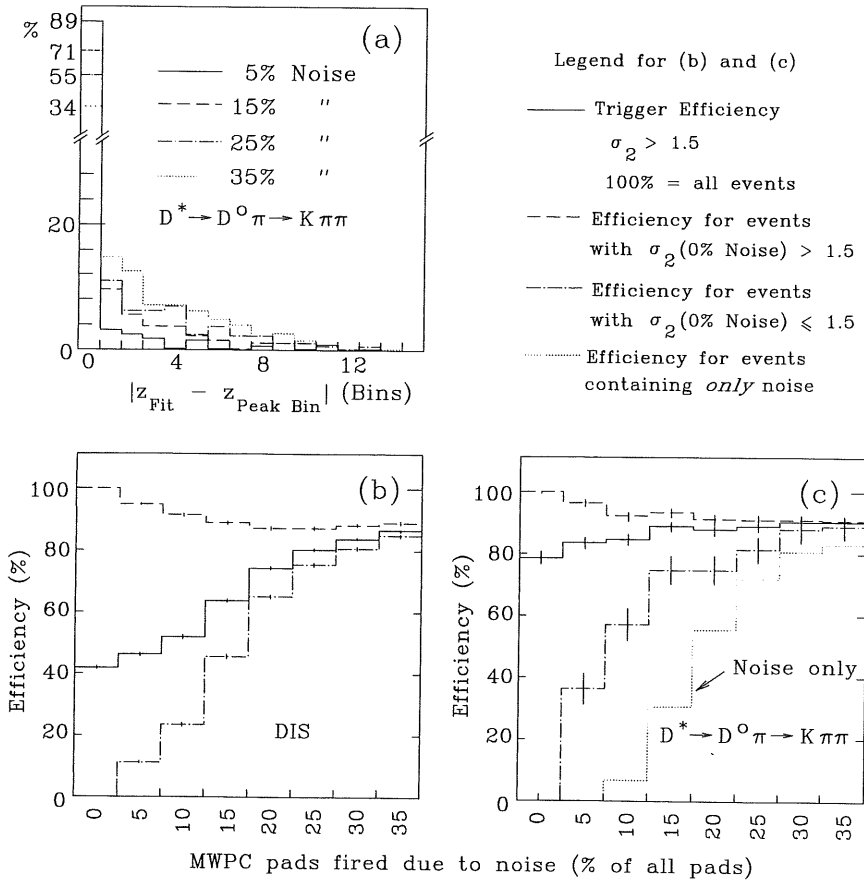


Fig. 25 Trigger efficiency as a function of the noise rate in the MWPCs for DIS (b) and $c\bar{c}$ (c) events. Although the average number of histogram entries increases from 20.6 to 776 with the noise rate going from 0% to 35%, the peak position is still well correlated to the reconstructed vertex (a). The $c\bar{c}$ sample is sharpened against the one discussed on page 52 by requiring at least two tracks in the central tracker with a transverse momentum $p_t > 250$ MeV and assumes fully efficient chambers. The DIS sample corresponds to the one shown in 29 with $T = 80\%$.

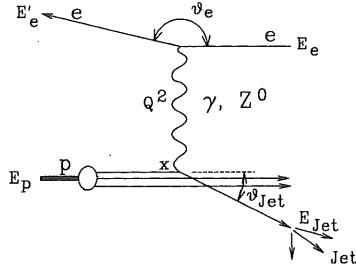


Fig. 26 The kinematical variables of a neutral current DIS interaction exchanging a γ or Z_0 are defined as follows: E_e and E'_e are the energies of the incoming and scattered electron respectively, ϑ_e is its scattering angle. ϑ_{Jet} is the angle of the outgoing quark (jet) respective to the proton direction, E_{Jet} its energy. The incoming proton carries an energy E_p , Q^2 is the square of the four momentum transfer between the electron and the quark, x the fraction of the proton momentum carried by the struck quark.

Although triggers for DIS events make use of the energy flow measurements in the liquid argon calorimeter and the BEMC to tag the outgoing jet and electron respectively, it is a good exercise to also investigate the z-vertex trigger performance in order to cross-check the triggers against each other.

The trigger efficiency as a function of x and Q^2 is given in figure 27. It is well above 90% for $Q^2 > 300 \text{ GeV}^2$ but as low as 40% for small values of Q^2 . The digitization threshold was set to $T = 80\%$ (see figure 29). The angle ϑ_{Jet} of the outgoing jet, together with the total transverse momentum p_t carried by it, largely determines the acceptance for a given event. These kinematical quantities can be calculated by requiring energy and momentum conservation only [34]:

$$\vartheta_{\text{Jet}}(x, Q^2) = \pi - \arccos\left(\frac{-x^2s^2 + xsQ^2 + 4E_e^2Q^2}{x^2s^2 - xsQ^2 + 4E_e^2Q^2}\right) \quad (13)$$

and

$$p_t(x, Q^2) = \frac{Q}{x\sqrt{s}} \cdot \sqrt{x^2s - xQ^2} \quad (14)$$

with $s = 4E_eE_p$ and E_e and E_p being the electron and proton beam energies respectively.

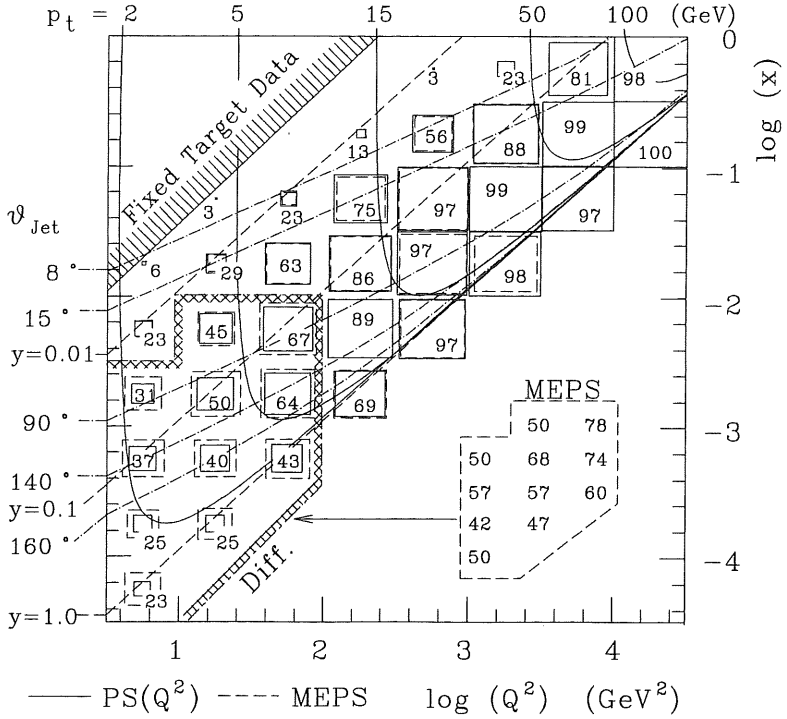


Fig. 27 Z-vertex trigger efficiencies in deep inelastic scattering are dependent on the event kinematics. For low values of Q^2 , the parton shower model used ($\text{PS}(Q^2)$ versus MEPS^9) affects the acceptance. The figures represent trigger efficiencies (in percent) for the $\text{PS}(Q^2)$ model. The inset shows the corresponding figures for the MEPS model for the region where they differ by more than the statistical errors from the $\text{PS}(Q^2)$ model.

For small values of p_t , the understanding of the hadronic final state becomes imperative if one wants to calculate trigger efficiencies. Following the discussions in [35], efficiencies have been calculated for two models of QCD effects, denoted $\text{PS}(Q^2)$ and MEPS^9 . The calculated trigger efficiencies differ by more than the statistical errors

⁹ $\text{PS}(Q^2)$: In ep collisions, two parton cascades are generated, one from the time-like scattered parton and one from the space-like initial parton in the proton. The amount and hardness of the gluon radiation depend sensitively on the virtuality of the parton before and after the quark-photon vertex. Q^2 can be chosen as the scale for the maximum allowed virtuality. (cont.)

only in the hatched area of figure 27, with $Q^2 < 100 \text{ GeV}^2$. At higher values, the transverse momentum is large enough to produce a sufficiently high particle multiplicity such that the trigger efficiency becomes independent of the detailed processes taking place at the photon-quark vertex of the ep interaction.

Rather than discussing the trigger efficiency as a function of x and Q^2 , it can be given in dependence of p_t and \mathcal{S}_{jet} , which is done in figure 28. An obvious dependence on p_t is seen. Also, the efficiency is almost independent of \mathcal{S}_{jet} over the geometrical acceptance range of the trigger, as expected from figure 23(d) on page 45. The t_0 efficiency - a non-empty histogram flags the exact HERA bunch crossing of an event triggered by another condition, which might be true over a longer period of time - is close to 100% over a wide range of p_t and \mathcal{S}_{jet} . Very forward oriented events however ($\mathcal{S}_{\text{jet}} < 16^\circ$) must rely on the forward ray trigger for t_0 .

With the HERA luminosity available in 1992, most DIS events were located at $Q^2 < 100 \text{ GeV}^2$. For these events, the overall z-vertex trigger efficiency is given in figure 29(a) as a function of the MWPC chamber digitization threshold T introduced in chapter 3.3.2 on page 39. T is compared with the charge deposited by a minimum ionizing particle traversing a chamber under $\mathcal{S} = 90^\circ$. The simulation took into account the p/mc dependence of dE/dx for a charged particle according to equation (10), but neglected its statistical distribution according to equation (11) (p. 32).

Also included in figure 29(a) is the trigger efficiency under the assumption of the MWPC status as described in chapter 3.5.1. It may be surprising that the dashed line corresponding to *real* chambers with some defective ϕ -segments and pads is above the solid line corresponding to *perfect* chambers. This however is only true because the chamber deficiencies were taken care of by enabling the corresponding *3-out-of-4* option. The penalty was a much higher background trigger rate. A comparison between Monte Carlo simulations and an independently triggered data sample is given in chapter 3.5.3.

Figure 29(b) contains efficiencies for another event class, namely the process $\gamma g \rightarrow c\bar{c}$, i.e. photon gluon into a charmed quark - antiquark pair. One of the c quarks is forced to decay through the channel $D^{*+} \rightarrow D^0\pi^+ \rightarrow K^+\pi^+\pi^+$. Such events do not deposit

MEPS: The photon-gluon and gluon radiation processes are simulated using exact order α_s matrix elements. Additional, softer emissions are added using the parton shower model. This model was found to best fit the data as measured at H1 [35].

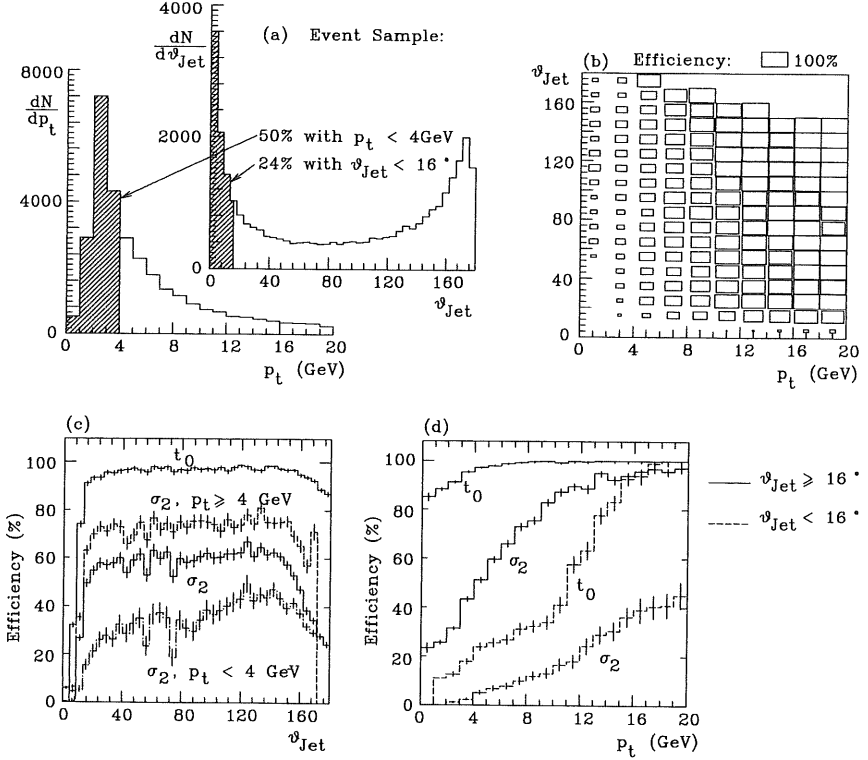


Fig. 28 DIS trigger efficiencies ($\sigma_2 > 1.5$, eq. (2), p. 32) as a function of p_t and ϑ_{Jet} are given in (b). Integrating over p_t and ϑ_{Jet} leads to the distributions (c) and (d) respectively. They must be viewed with the distribution of the event sample in the two variables p_t and ϑ_{Jet} in mind (a). The efficiencies marked with t_0 correspond to the *weak* t_0 condition (non-empty histogram). The sample corresponds to the $\text{PS}(Q^2)$ data of figure 27.

much energy in the calorimeter and thus rely on a pure track trigger. The threshold dependency is higher than for DIS events, which underlines the importance of a detailed understanding of the chambers.

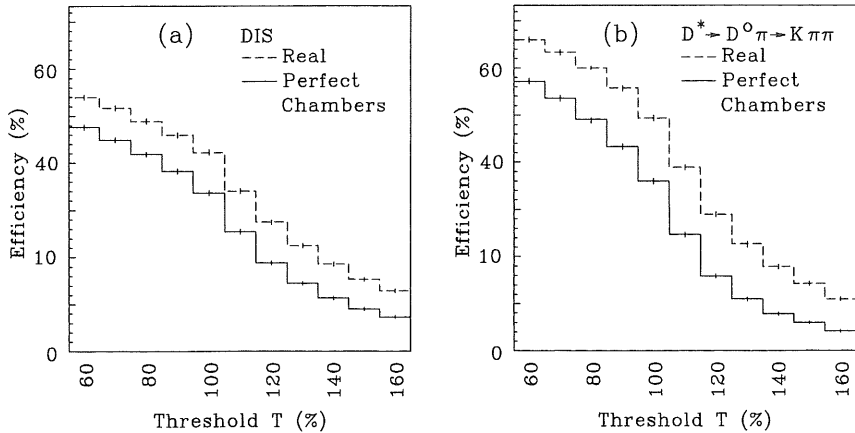


Fig. 29 Trigger efficiencies are dependent on the chamber digitization threshold T . 'Real' chambers refer to the MWPC status in 1992, as described in chapter 3.5.1. (a) shows the threshold dependency for DIS events with $Q^2 < 100 \text{ GeV}^2$. (b) shows a slightly higher dependency for another event class, namely $\gamma g \rightarrow c\bar{c}$, where one quark decays through a D^{*+} . T is defined on pages 39 and 52.

3.5 Experiences during the first H1 run period

3.5.1 The MWPC performance

The trigger performance is of course by no means independent of the MWPC performance. Dead pads and sectors directly lead to inefficiencies. Thus, we will shortly summarize the deficiencies as they existed in the MWPC area during the first running period of H1 in 1992.

The most severe single problem existed in the forward MWPCs, where about half the preamplifiers, which are directly mounted on the chambers and thus inaccessible after installation of the tracking detector, were defective. They operated satisfactorily during a test running period in spring 1991 but, after a summer maintenance shutdown,

failed to function since October 1991 for unknown reasons¹⁰. With the defective pads distributed randomly over all supermodules and chambers, the chances for a ray requiring forward pads to have fired were minimal due to the necessary coincidence between two pads.

It would have been possible for the trigger to react to this situation by either permanently switching the defective pads on or alternatively enable the *3-out-of-4* option in the forward region. For practical reasons however - to avoid the handling of complex setup files in times when they not only changed very often in order to adapt to new situations and experiences but when also the interpreting program was still under development, causing the file format to alter rather frequently - the forward region was operated *as is* as far as the z-vertex trigger was concerned. This caused it de facto to be permanently switched off.

Even before May 1992, the start of the first running period, one ϕ sector of the outer layer of CIP had to be switched off because it developed a short in the high voltage connection. For electrostatic reasons, also one neighbouring sector had to be degraded. As a reaction to this situation, the corresponding pads were allowed to be missing in the relevant rays by using the *3-out-of-4* option as described by equation (18) on page 78. With the option only enabled for one layer, this was logically identical to switching the respective pads permanently on.

Equally early, one ϕ sector of the outer layer of COP displayed a similar problem. Unfortunately, here both its neighbours needed degrading. Consequently, the corresponding *3-out-of-4* bits were enabled.

Later in the running period, two further sectors of the outer layer of CIP were damaged due to careless operation at a time when the HERA beam was not yet declared stable. Again, we made use of the *3-out-of-4* option. All these problems led to a total of 7 out of the 16 ϕ -segments of the trigger, which needed being operated as 3-fold coincidences only for the ray building.

All MWPCs experienced considerable electrical noise from various sources due to debatable grounding schemes. Especially the large pads of the COP proved to be good

¹⁰ The operating crew of the forward MWPCs assumed humid conditions in the preamplifier area during a hot summer period to have caused the failure.

antennas. As a consequence, the thresholds of the discriminators had to be increased at the cost of reducing the chamber efficiency. The latter could be determined from the data using particle tracks, which were well measured in the central jet chambers and which could be extrapolated into both CIP and COP. The average pad efficiencies in the active sectors varied between 94% and 97% for CIP, slightly lower than what was measured previously with test beams (99%, [26]). For COP, the noise problem was more severe and hence only an efficiency between 86% and 88% could be reached for the high thresholds needed [36].

The synchronization window of each subdetector must be carefully adjusted against the HERA clock phase such that each clock cycle at the output of the synchronization unit is uniquely related to a bunch crossing. This task is quite involved.

After installation, the time resolution of the CIP system was measured with cosmic rays using the final readout electronics and cables. The base width of the resolution shown in figure 30 was found to be 75 ns. Given the HERA bunch crossing frequency of 10.6 MHz, it is obvious that the adjustment of the synchronization clock phase, which defines the clock cycle within which a positive edge at the output of the discriminator is accepted for a certain bunch number, has to be made to a precision of well below 20 ns. Only slight misadjustments may lead to large ray inefficiencies, since a ray is a 4-fold coincidence between pad signals. Figure 31 illustrates this q^4 dependence¹¹ of the single ray efficiency, with q being the probability for a pad signal to be synchronized into the correct bunch crossing.

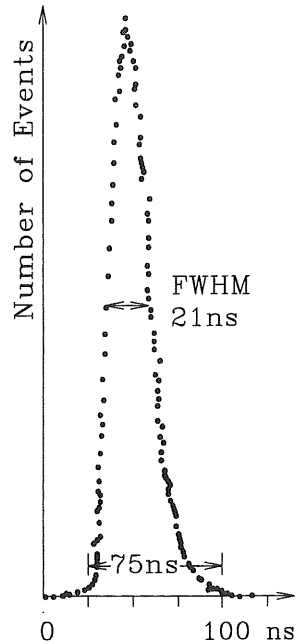


Fig. 30 Time resolution of CIP, taking into account the entire readout chain [26].

¹¹ Systematic shifts between the timing of some pads versus others may complicate the calculation of single ray efficiencies, but produce a qualitatively equivalent result. One would have to replace q^4 with $q_1 \cdot q_2 \cdot q_3 \cdot q_4$, with q_i being the probability of the pad signal from chamber i to be correctly synchronized.

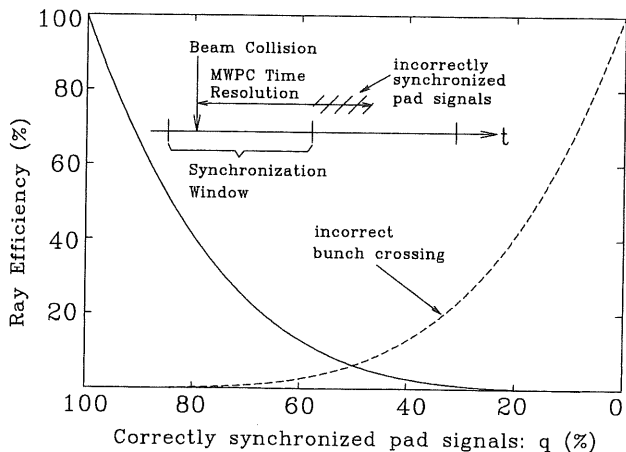


Fig. 31 The ray and thus trigger efficiency is highly dependent on the correct timing of the synchronization window relative to the HERA bunch crossing.

A problem in adjusting the MWPC clock phase is that almost any imaginable H1 trigger currently requires a *weak* t_0 information from the proportional chambers. All other triggers either cannot uniquely flag a single bunch crossing for an event they accepted, such as the calorimeter trigger, or run at such a high rate that they cannot be used in a stand-alone mode, such as the ToF system. Thus, the events used to analyze the MWPC timing already depend on the timing one wants to measure.

Consequently, it was necessary to analyze a series of special purpose runs, each taken with a different synchronization clock phase. Offline analysis of the MWPC hit distribution over many bunch crossings then allowed to evaluate the correct timing. It manifested itself by having (almost) no hits in the bunch before the one which triggered the event. Saturation effects of the preamplifiers may fake hits in the bunches *after* the trigger. Therefore, one chooses the earliest timing with no hits in bunches preceding the trigger to be the correct one. It is essential for the operation of the system to permanently monitor this critical parameter by observing the synchronization clock phase and the hit distributions.

3.5.2 The z-vertex trigger performance

The z-vertex trigger was first operated on cosmic ray events in October 1991 and then used during the entire 1992 HERA running period. It was however always operated in coincidence with the ToF system (figure 8, p. 24) except for very few test runs. Since the driftchamber R- ϕ trigger became only operational in September, it was the only track trigger available to H1 before that.

The trigger algorithm was typically chosen according to equations (2), with $x_2 = 1.5$, and (3) (p. 32). This resulted in a stand-alone trigger rate on the order of 15 to 30 Hz, depending on the beam quality, even with the luminosity as low as $\mathcal{L} \approx 10^{29} \text{ cm}^{-2}\text{s}^{-1}$. Scaling this to the HERA design luminosity results in a rate of the same order of magnitude as expected from Monte Carlo background simulations.

Visually scanning the events accepted by the trigger lead to the observation, that about 50% of them displayed no reconstructible tracks in the CJC. They show large spots of activity in the R- ϕ projection of CJC. An example is given in figure 32. The origin of this activity is not yet fully understood, but it seems to be related to the electron beam. The hits in the MWPCs are randomly distributed. Consequently, the peaks in the z-vertex histogram are faked by wrong pad combinations only. The remaining events mostly display a vertex within the interaction zone, although many are clearly interactions with residual gas atoms, as none of the tracks have a small DCA.

This observation led to an L4 filter program, which rejected events with no reconstructible tracks. Also, events with all tracks originating from upstream were rejected. The L4 processor reduced the data sample accepted by the z-vertex trigger alone by an average of 50%, which brought the data logging of H1 to an acceptable rate for the event recording devices. Nevertheless, the high L1 rate combined with

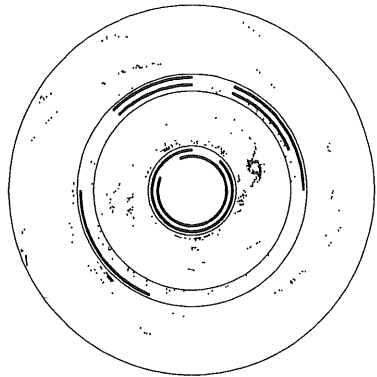


Fig. 32 Electron beam related background caused random hit patterns in the CJC as well as the MWPCs and thus resulted in large numbers of L1 triggers, which could easily be rejected by the L4 filter farm.

the slow readout speed of most front-end systems at the beginning of the run period led to a dead time at the limit of acceptability.

To reduce the L1 rate, the stand-alone z-vertex trigger was vetoed by a *CIP-Backward* signal, derived from pads at the -z side of CIP. Using NIM electronics, the 15 backward oriented pads of each ϕ sector of each layer were ORed. The coincidence of the two layers produced the sector signals. Three or more such sector signals led to the veto condition. The underlying idea is to reject upstream proton - beam pipe interactions, which produce activity in an area of CIP not included in the z-vertex trigger. This veto reduced the trigger rate by about 25% by rejecting some 70% of the events with an upstream vertex and roughly 15% of the electron beam related events discussed above. Less than 6% of events with a vertex in the nominal interaction zone were vetoed.

When the driftchamber R- ϕ trigger became operational, it was run in coincidence with the z-vertex trigger. The combined rate was typically as low as 4 Hz. Many events formerly rejected by L4 did not meet both criterions. The stand-alone operation of the z-vertex trigger was then ceased or prescaled with a high factor for monitoring purposes.

Within the H1 trigger cocktail selected in the CTL1 box, the z-vertex trigger was also run in coincidence with (see figure 6, p. 22)

- a required energy deposition in the BEMC, which tagged a scattered electron.
- the electron tagger, asking for a scattered electron under a very low angle plus some activity in the central tracker. Such an event is shown in figure 13 on page 31.
- the liquid argon calorimeter trigger.
- the muon trigger, which, in itself, has no vertex restricting capabilities. As one wanted to tag events with a few muons only, the z-vertex histogram was required to have just a few entries: The peak size was requested to be less than six and the sum of all other bins below four.

All these combined triggers produced a total rate below 1 Hz and therefore posed no problem for the data acquisition chain.

Figure 33(a) shows the vertex distribution of an electron-tagged event sample with the additional requirement of at least one registered track in the CJC with a small DCA. (b) shows the subsample, which was also accepted by the z-vertex trigger. The trigger has an obvious preference for events originating from the histogram area with $|z| < 439$ mm. Peaks in the outermost two bins on each side of the histogram were not allowed

to trigger. Thus, the effective acceptance zone was restricted to $|z| < 329$ mm.

Figure 34 displays the agreement between the peak location in the z-vertex histogram and the z-coordinate of the reconstructed primary vertex. 7678 events of a POT, a production output tape containing all but the L4-rejected events, were analyzed independent of the trigger conditions. 33% had a reconstructible vertex. Many of the other 67% were triggered by energy requirements in the BEMC or electron tagger and had not necessarily enough activity in the tracker to allow reconstructing the primary vertex. From a second sample of 5309 L4-rejected events only 18% had a reconstructible vertex.

79% of those POT events with a reconstructed vertex also had a z-vertex peak significance $\sigma_2 > 1.5$. This ratio was increased to 86% when the fitted vertex coordinate was restricted to $-440 \text{ mm} < z_{\text{Fit}} < 440 \text{ mm}$, which was fulfilled by a total of 1794 events. Figure 34(a) shows the correlation between z_{Fit} and the peak bin location for events with $\sigma_2 > 1.5$. (b) contains 246 events with $\sigma_2 \leq 1.5$, (d) 438 events rejected by the L4 filter program. Figure 34(c) shows the projection of (a) and (b) and proves that a peak gives a good estimation of the primary vertex location even if it is not significant. This is important to know, as big rays discussed in chapter 3.1 are enabled for *any* non-empty histogram. It might prove helpful to also accept big ray candidates related to histogram bins adjacent to the peak bin.

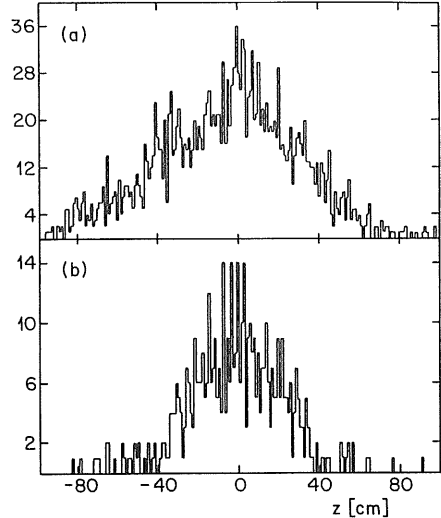


Fig. 33 (a) Distribution of event vertices along the beam axis for events triggered with the electron tagger and the subsample (b) triggered by the z-vertex trigger in addition.

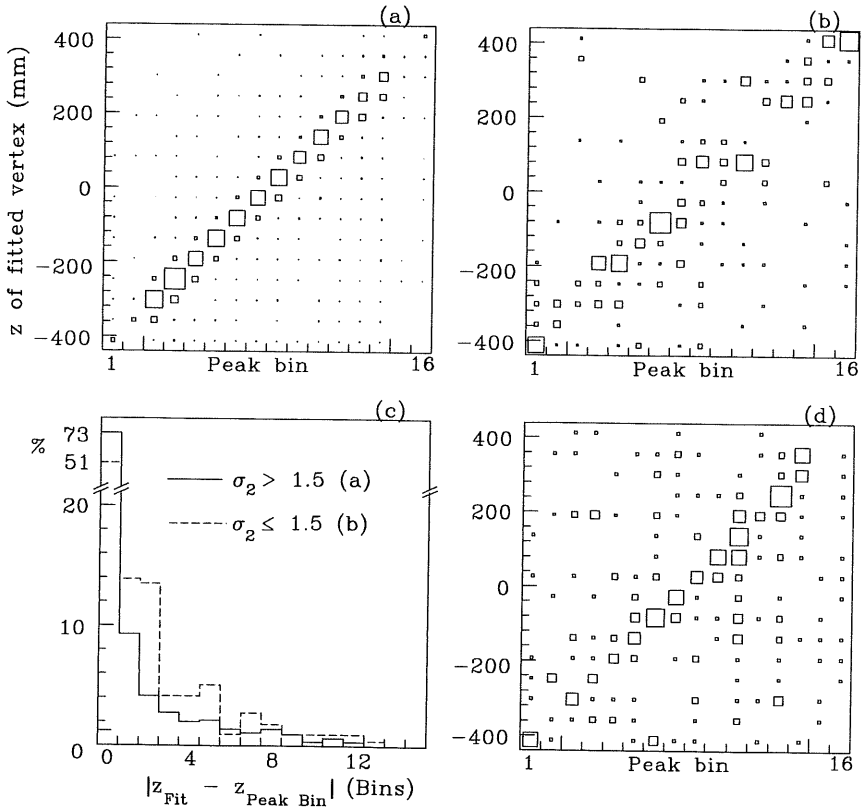


Fig. 34 The correlation between the peak bin of the z-vertex histogram and the z-coordinate of the reconstructed event vertex is shown for events with $\sigma_2 > 1.5$ (a) and $\sigma_2 \leq 1.5$ (b) (eq. (2), p. 32) which were accepted by the L4 filter program. (c) projects (a) and (b). (d) shows events rejected by L4.

3.5.3 Trigger performance on deep inelastic scattering events

The trigger performance largely depends on the digitization threshold T as explained in chapter 3.3.3 and 3.4 (see figure 29, p. 54). The charge deposited on any given chamber pad has to be larger than T in order for the pad to fire. T can be determined by the following procedure:

- Z-vertex triggered events are selected.
- Reconstructed tracks (in the CJC) that cross both CIP and COP or CIP and the first forward MWPC pair are selected. Such tracks are supposed to enable a ray in the z-vertex histogram.
- The track is requested to be isolated, i. e. no other track is found in the same spatial region.
- The z-vertex histogram is reconstructed under the assumption, that the selected track has not fired any MWPC pads at all. If the resulting histogram still had triggered the event, the selected track is said to be *unbiased*.
- The pad efficiency can be calculated from such unbiased tracks.
- The same procedure is applied to Monte Carlo simulated events. T is varied until the resulting pad efficiencies match those observed in real events¹².

With the above procedure, individual thresholds for each ϕ segment and layer of the central MWPCs were derived. For the following discussion, we completely turned off the forward chambers because of the problems reported in chapter 3.5.1.

Once T is determined, the z-vertex trigger efficiency of Monte Carlo simulated events can be compared with real data. For that purpose, we selected 1689 BEMC triggered events, which were filtered to match the following conditions:

- The energy deposited in the BEMC in the most energetic cluster was required to be $E_{\text{BEMC}} > 14$ GeV. This cut rejects photoproduction events.
- Within a radius of 15 cm around this BEMC energy cluster, a particle must have been seen in the backward MWPC thus identifying the energy cluster as originating from a particle, presumably an electron, coming from the H1 interaction region.

¹² A simpler approach than described by equation (5) (p. 39) was used to distribute the charge induced by one particle over neighbouring pads. All charge originating from a track segment directly underneath a given pad was attributed to that. Crosstalk was introduced as a global quantity, which transferred a certain percentage of the charge on each pad to its neighbours.

- For reasons related to the mechanics of the BEMC and the backward MWPC, either the x- or the y-coordinate of the energy cluster location had to be more than 16 cm from the beam line and the radius of the MWPC hit had to be in the range between 18 cm and 60 cm.
- The event had to have a reconstructible vertex with $|z_{\text{vertex}}| < 50$ cm.

A similarly treated sample of 5121 Monte Carlo simulated events was available for comparison.

A typical DIS event matching the above conditions is displayed in figure 35. The distribution of the event sample in the x-Q² plane is given in figure 36. The BEMC accepts electrons scattered under an angle $155^\circ < \vartheta_e < 174^\circ$.

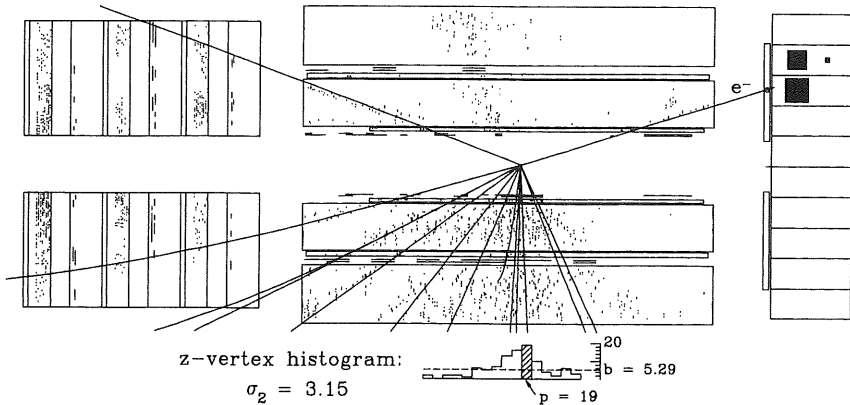


Fig. 35 A typical DIS event triggered by an energy cluster in the BEMC. The z-vertex trigger was not required but accepted the event as well. From the electron, one can reconstruct $x = 4.14 \cdot 10^{-3}$ and $Q^2 = 58 \text{ GeV}^2$ (equations (15) and (16), p. 64)

The hit multiplicities between the data and Monte Carlo sample for the four layers of central MWPCs were in good agreement with each other except for the inner layer of COP, which obviously contained many noise induced hits. We therefore restricted our sample by the additional condition $(COP-0 < 0.9 \cdot COP-1 + 10)$ AND $(COP-0 \leq 21)$ with COP-0 and COP-1 being the hit multiplicities of the two layers. This reduces the data sample by 25.9%, whereas the Monte Carlo sample is left almost untouched as only

0.84% of the events are rejected. Figure 37(a) compares the hit multiplicities before and after this cut.

Although the above cut does not significantly change the trigger efficiencies, as is expected from the discussion in chapter 3.3.4, we leave it in place, as it affects the number of entries in the z-vertex histogram. Figure 37(c) shows the average peak height and 37(d) the total number of histogram entries. The resulting peak significance σ_2 according to equation (2) (p. 32) is plotted in figure 37(b).

The kinematical variables x and Q^2 as introduced in figure 26 on page 50 can be reconstructed from the scattered electron only [34]:

$$Q_{el}^2 = 2E_e E_e' (1 + \cos(\vartheta_e)) \quad (15)$$

and

$$x_{el} = \frac{Q_{el}^2}{s \cdot y_{el}} = \frac{Q_{el}^2}{s} \cdot \left(1 - \frac{E_e'}{2E_e} \cdot (1 - \cos(\vartheta_e)) \right)^{-1} \quad (16)$$

The error in x_{el} becomes large for small values of y . It is therefore preferable to reconstruct y from the properties of the jet according to the method of Jacquet-Blondel, if $y_{el} < 0.2$:

$$y_{JB} = \frac{E_{Jet} \cdot (1 - \cos(\vartheta_{Jet}))}{2E_e} = \frac{\sum_i (E_i - p_{z,i})}{2E_e} \quad (17)$$

The sum runs over all observed final state hadrons. E_i and $p_{z,i}$ denote their energies and the z-component of their momenta respectively. We then calculate $x_{Mixed} = Q_{el}^2 / s \cdot y_{JB}$ with $s = 4E_e E_p$ and E_e and E_p the beam energies.

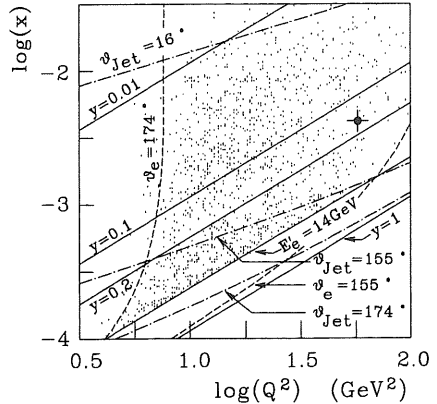


Fig. 36 Distribution of the DIS event sample in the x - Q^2 plane. The BEMC accepts scattered electrons under an angle $155^\circ < \vartheta_e < 174^\circ$. The sample was required to have $E_e' > 14$ GeV. The event shown in figure 35 is marked by a cross.

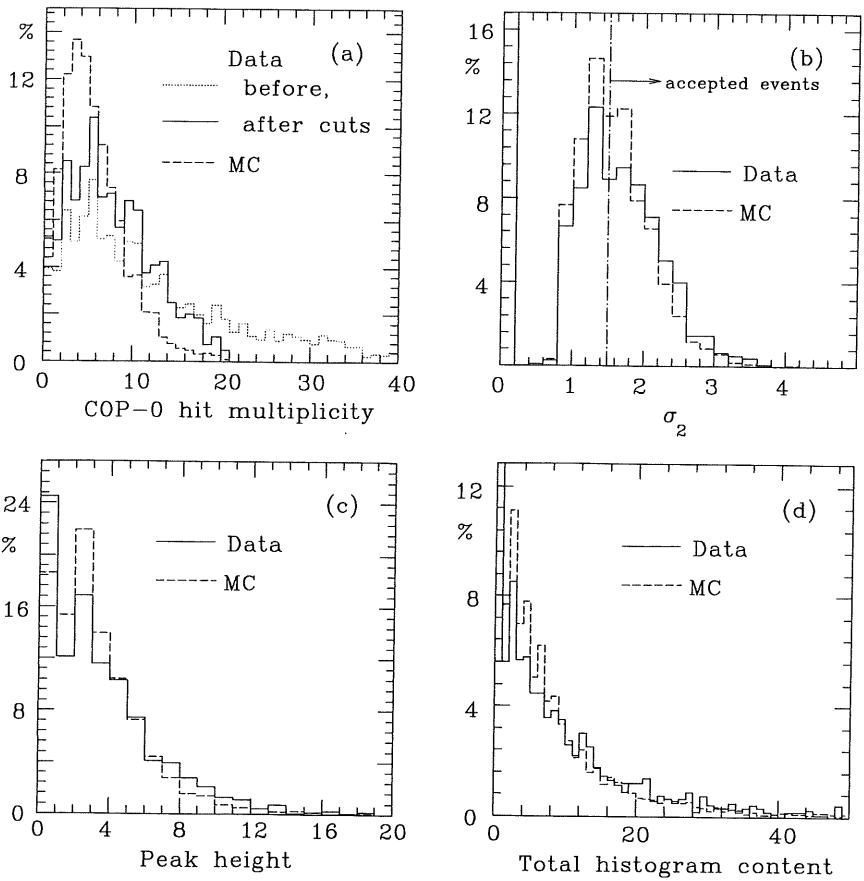


Fig. 37 (a) shows hit multiplicities of the inner layer of COP for the Monte Carlo and the data sample. The latter was improved by rejecting events with many noise hits in the COP as explained in the text. (b) compares the peak significance σ_2 (eq. (2), p. 32), (d) the total number of histogram entries and (c) the peak height.

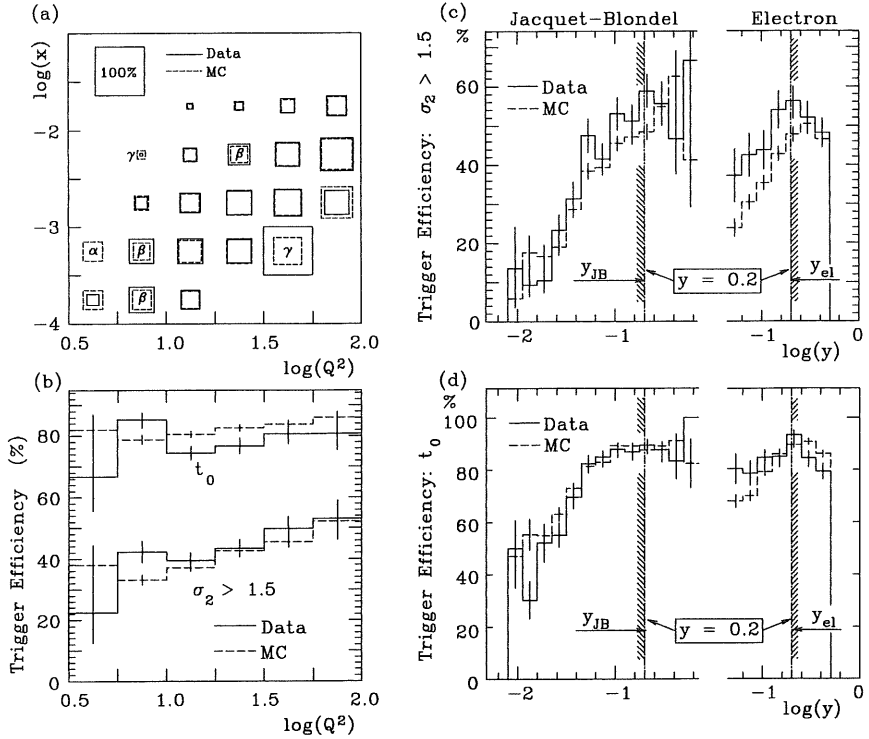


Fig. 38 (a) gives a comparison between simulated and observed trigger efficiencies as a function of x and Q^2 . No data were available for the box marked α . Only in the areas marked with β differ the trigger efficiencies by more than the statistical errors. Too few events were available in the kinematical ranges marked with γ to calculate statistical errors. (b) shows the trigger efficiencies as a function of Q^2 for both the *weak* t_0 condition and $\sigma_2 > 1.5$ (eq. (2), p. 32). (c) and (d) plot the same efficiencies as a function of y . For $y < 0.2$, the reconstruction method from Jacquet-Blondel (eq. (17)) gives better results. For larger values of y however, it should be reconstructed from the electron (eq. (16), p. 64). All error bars indicate statistical errors only.

Figure 38(c) and (d) show good agreement of the simulated and observed z-vertex trigger efficiencies as a function of y for both the *weak* t_0 condition (non-empty histogram) and $\sigma_2 > 1.5$ (equation (2), p. 32), if one chooses the optimum reconstruction method for y . The efficiencies as a function of Q^2 are given in figure 38(b). The slight discrepancy between the simulated and observed efficiencies in the kinematical range $10^{-4} \leq x \leq 10^{-3}$ and $5 \leq Q^2 \leq 10$ (figure 38(a)) can be partly explained by the kinematics of these events (see figure 36). Firstly, the scattered electron enters the BEMC almost at its inner boundary ($\vartheta_e \approx 174^\circ$). Secondly, the jet from the struck quark also points towards the BEMC and thus may disturb proper energy measurement of the electron.

The integrated σ_2 trigger efficiency within the kinematical range shown in figure 36(a) is $42.5 \pm 1.4\%$ for the data sample and $39.6 \pm 0.7\%$ for the Monte Carlo events. The *weak* t_0 condition is set by $78.0 \pm 1.2\%$ of the recorded and $81.5 \pm 0.6\%$ of the simulated events. Removing the noise cut on the COP hit multiplicity described above alters the efficiencies of the data sample by statistically insignificant 0.2% (σ_2) and 0.4% (t_0) only.

3.5.4 Total photoproduction cross section measurements

The total cross section for photoproduction events was measured during the first three months of H1 operation in the new kinematical region of an average centre of mass energy of $W_{\gamma p} \approx 190$ GeV [10]. Previous measurements were limited to $W_{\gamma p} \leq 18$ GeV [37], which left room for various theoretical models with expected total cross sections $\sigma_{\gamma p}^{\text{tot}}$ anywhere between $145 \mu\text{b}$ and $250 \mu\text{b}$ at $W_{\gamma p} = 250$ GeV [38].

At HERA, one can calculate $\sigma_{\gamma p}^{\text{tot}}$ from $d^2\sigma_{ep}/dydQ^2$ using the Weizsäcker-Williams approximation (WWA), which holds for very small Q^2 . It is $d\sigma_{ep} = \sigma_{\gamma p}^{\text{tot}} \cdot F(y)$ [39] with σ_{ep} the cross section for ep scattering processes and $F(y)$ a kinematical flux factor.

Two partly overlapping event samples were used. A so-called *tagged* sample required a level one trigger with an energy deposition in the electron tagger of $E_e > 4$ GeV in coincidence with an energy in the photon detector of $E_\gamma < 2$ GeV. The latter excludes bremsstrahlung events. Additionally, some minimal central tracker activity was required by the *weak* t_0 condition of the z-vertex trigger: A non-empty histogram was equivalent to requesting at least one ray in the central area (CIP/COP) due to the defective forward MWPC preamplifiers. The electron tagger requirement restricted the scattered electron to a cone with $\vartheta_e \leq 5$ mrad. Obvious background sources were removed offline by

sharpening the track requirements. Proton - gas interactions with a random coincidence of the electron tagger signal manifested themselves in adequately chosen kinematical variables.

A second, *non-tagged* sample was taken with the z-vertex trigger alone, with a peak significance condition according to equation (2) with $x_2 = 1.5$ (p. 32). As usual, the peak location was restricted to bins 3 to 14, requesting the primary vertex to obey $|z_{\text{vertex}}| \leq 329$ mm. This sample releases the requirement on ϑ_e . Background, mainly due to proton interactions with residual gas atoms within the interaction region, was statistically subtracted by comparing the trigger rate during those machine bunches filled with electrons and protons with that of the pilot bunches, which contained only protons or electrons respectively. This method reduced the sample by a factor of 10.

Considering an integrated luminosity $\int \mathcal{L} dt \approx 1.5 \text{ nb}^{-1}$ and all necessary cuts applied offline, 917 ± 38 events were found in the tagged sample and 940 ± 65 in the non-tagged one. The overlap contained 170 events. The total cross section was determined as $\sigma_{\text{p}}^{\text{tot}} = 159 \pm 7(\text{stat.}) \pm 20(\text{syst.}) \mu\text{b}$ for the tagged sample and $\sigma_{\text{p}}^{\text{tot}} = 152 \pm 10(\text{stat.}) \pm 32(\text{syst.}) \mu\text{b}$ for the non-tagged. The errors for the latter are bigger largely due to model dependencies of the expected activities in the central tracker region and the difficult background subtraction. The results agree with those from ZEUS [40] and seem to support Regge motivated parameterizations such as [41] and [42], but defy QCD minijet models [43]. Figure 39 shows these new data points in relation to previous measurements.

The good agreement between the cross section determined from the tagged and untagged sample underlines the understanding of the z-vertex trigger efficiency.

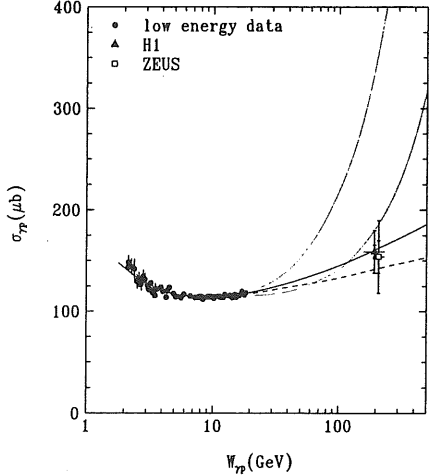


Fig. 39 The cross section $\sigma_{\text{p}}^{\text{tot}}$ as measured by H1 and ZEUS in comparison with existing data drastically illustrates the new energy scale accessible by HERA. The solid curve represents a Regge based fit of low energy data [41]. The dashed curve is the prediction of an ALLM parameterization [42]. The dotted lines are obtained using PYTHIA Monte Carlo with different parameterizations [43].

3.5.5 Hard scattering in γp interactions

To get a better understanding of (quasi-)real photon interactions with quarks and gluons inside the proton, the same hardware trigger conditions as described above were also used to study single particle distributions in the process $ep \rightarrow e+\text{hadron}+X$ with tagged events and inclusive jet production ($ep \rightarrow e+\text{jet}+X$) with a non-tagged sample [44].

Somewhat stronger but basically equivalent offline cuts as above were met by 330 tagged events. This was shown to be an almost pure ep sample by several independent methods. To investigate high p_t jets, non-tagged events were offline restricted to those having deposited a transverse energy E_t of at least 10 GeV in the calorimeter ($\theta > 25^\circ$). Deep inelastic scattering reactions were rejected by cutting on electron candidates with $E_{\text{BEMC}} > 10$ GeV in the BEMC. The final sample contained 51 events.

The cuts applied to the non-tagged events were also met by 19 tagged events. Of them, 10 were also accepted by the z -vertex trigger. The resulting trigger efficiency of $53 \pm 17\%$ agrees well with that derived from Monte Carlo simulations.

The investigations suggest the presence of resolved photon processes as required by QCD [45], which is supported both by the rate of the observed events and their spatial jet distribution.

3.6 Improving the trigger as a vertex estimator

3.6.1 Principle of the vertex estimator

The above chapters describe the current implementation of the z -vertex trigger. Its decision is solely based on analysing the single z -vertex histogram, although it is the sum of 16 individual histograms, one for each of the ϕ -segments of the chambers. This additional information has not been used other than by suppressing 'wrong' hit combinations and thus background entries in the histogram.

The good agreement between the reconstructed (or Monte Carlo generated) vertex and the peak bin position for most triggered events, as shown in figure 34 on page 61, underlines the effectiveness of the trigger as an estimator for the z-coordinate of the primary interaction. Knowing this, we can suppose that each sub-histogram of each ϕ -segment should also reconstruct the vertex coordinate of all activity reaching this segment. Thus, at best, all non-empty sub-histograms should display a peak in the very same bin as the z-vertex histogram does.

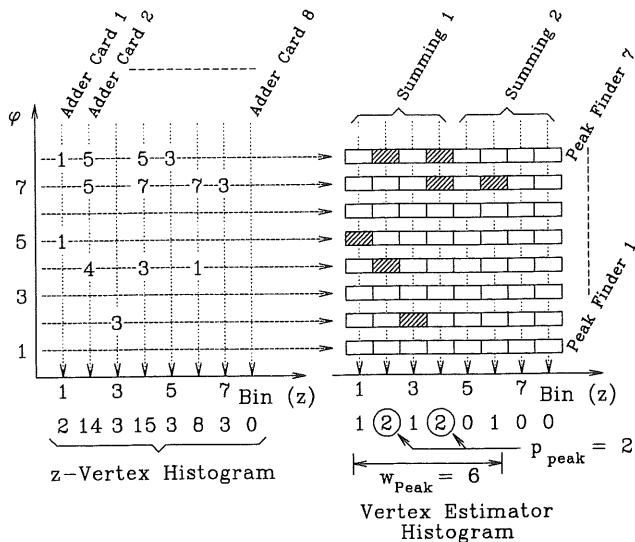


Fig. 40 The vertex estimator uses information from all ϕ -segments to construct a new *vertex estimator histogram*, which increases the background rejection power by cutting on the new variables p_{Peak} and w_{Peak} .

Using the additional information from each ϕ -segment can be done as illustrated in figure 40. For simplicity, only the non-empty entries of the sub-histograms are shown. Also, only eight bins and segments are displayed. An additional 16 bin wide *vertex estimator histogram* is constructed and evaluated:

- Each bin of the new histogram is correlated to a z-position along the beam axis, similar to the original z-vertex histogram.
- For each of the 16 z-vertex histograms related to a ϕ -segment, peak position(s) are evaluated.

- Each such peak found leads to an entry in the corresponding bin of the newly defined histogram.
- The peak p_{Peak} in this new histogram is evaluated.
- The histogram width w_{Peak} , that is the number of bins spanned by non-empty entries, is measured.
- New cuts are expressed in terms of p_{Peak} and w_{Peak} .
- Additionally, one might calculate b_{Peak} , the average number of entries in all but the peak bin of this new histogram. This allows calculating σ_{Peak} according to equation (2) on page 32.

Adapting the hardware to this scheme is discussed in chapter 6.3.

3.6.2 Performance of the vertex estimator

The performance of the suggested improvement of the z-vertex trigger can be tested directly with data taken during the 1992 running period of HERA, thus omitting most uncertainties involved in Monte Carlo simulations. Figure 41(a) shows the variable p_{Peak} for four classes of events that were accepted by the original z-vertex trigger ($\sigma_2 > 1.5$, equation (2), p. 32):

- L4-Reject - events, which have been rejected by the level 4 filter farm. The aim of any new L1 trigger must be to reject such events before the front-end readout process has even started.
- DST - events, which were selected for the data summary tapes, thus fulfilled some minimal physics classification requirements. About 3% of all recorded events qualify for the DSTs. Additionally, the sample was sharpened by asking for a reconstructed vertex with $|z_{\text{vertex}}| < 50$ cm and at least two reconstructed tracks (in CJC) crossing both CIP and COP and having a transverse momentum $p_t > 400$ MeV. Events not meeting these requirements cannot be expected to be accepted by the z-vertex trigger for other reasons than random coincidences.
- DIS - events from the autumn 1992 running period. This sample is further discussed in chapter 3.5.3.
- $c\bar{c}$ - Monte Carlo simulated events producing a charmed quark-antiquark pair through γ -gluon fusion. One of the quarks is forced to decay through the channel $D^{*+} \rightarrow D^0\pi^+ \rightarrow K^-\pi^+\pi^+$. Triggering such events is typically restricted to track triggers only, as almost no energy is deposited in the calorimeter. The sample is sharpened compared to the one used in chapter 3.4 (page 52) by requiring at least two tracks in the central tracker with a transverse momentum $p_t > 250$ MeV.

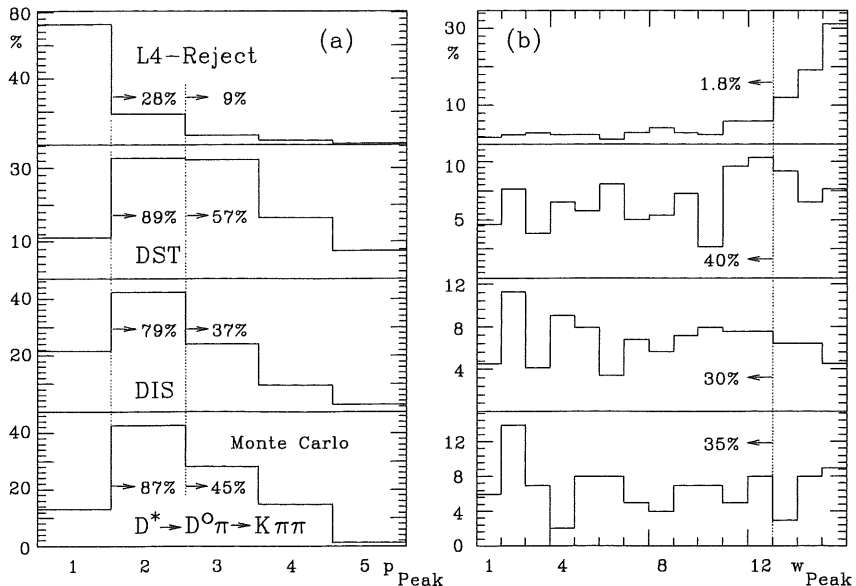


Fig. 41 (a) The variable p_{Peak} is shown for different event samples which have been accepted by the standard z -vertex trigger criterion ($\sigma_2 > 1.5$, eq. (2), 32). (b) w_{Peak} indicates further possible cuts if plotted for events with $p_{\text{Peak}} \geq 3$. The vertical axis of (b) shows the efficiency relative to the events accepted in (a), whereas the numbers in the figure refer to the full sample accepted by $\sigma_2 > 1.5$. Refer to the text for an explanation of the samples used.

Cutting at $p_{\text{Peak}} \geq 3$ rejects 91% of all σ_2 -triggered L4-Reject events, but only 55% of the $c\bar{c}$ events. According to figure 41(b), further¹³ improvements can be made by cutting at $w_{\text{Peak}} \leq 12$. 35% of the $c\bar{c}$ events meet this requirement as opposed to only 1.8% of the L4-Reject events.

¹³ w_{Peak} would not distinguish between data and background if plotted before cutting on p_{Peak} . Also, the weaker condition $p_{\text{Peak}} \geq 2$ cannot be improved by additional requirements on w_{Peak} .

For a successful operation of H1, it is important to have a low enough L1 trigger rate, such that the readout chain is not saturated and does not produce more than about 20% dead time. If the L1 rate increases above this critical limit, it must be linearly downscaled, which is equivalent to running at a lower machine luminosity. Thus, the quality of a trigger can be expressed by the acceptance A for desired events alone, if its total rate R is not critical to the readout chain. Above that limit, a quality factor Q , defined as $Q = A/R$, measures the trigger performance.

Table 5 compares the suggested vertex estimator with existing H1 track triggers. The trigger rates for both the L4-rejected and accepted events correspond to a beam luminosity as existing during the autumn 1992 running period, $\mathcal{L} \approx 10^{29} \text{ cm}^{-2}\text{s}^{-1}$. It is expected to be higher by about a factor of 10 in 1993. This would easily saturate the readout chain. Thus, tighter trigger conditions are imperative.

The biggest improvement with the vertex estimator is achieved if compared with a stand-alone z-vertex trigger. More realistically however, the z-vertex trigger is run in coincidence with the driftchamber $R-\phi$ trigger to restrict the primary vertex both along z and in the $R-\phi$ plane. With this combination, not more than a factor two can be gained in the trigger quality, at the cost of reducing the $c\bar{c}$ acceptance to a low 14%.

Figure 42 shows, how the new cuts actually tighten the event selection. (a) shows the efficiency of the vertex estimator compared to the original z-vertex trigger as a function of the z-coordinate of the primary vertex. Figure 42(b) and (c) suggest that preferably events with sufficient tracker activity are selected. The efficiency increases as a function of the number of reconstructible track segments found in the CJC as well as of the number of so-called *good* tracks. The latter are segments that reach at least from CIP to COP, have a transverse momentum p_t larger than 400 MeV and $DCA < 50$ mm, thus have a good chance of enabling a ray in the z-vertex trigger histogram.

The data sample used for figure 42 consists of 17060 recorded but otherwise unfiltered events¹⁴ which have been accepted by the z-vertex trigger according to equation (2) with $x_2 = 1.5$ (p. 32). Being recorded however means they have also been accepted by the level four filter program, which rejects L1 triggers based on tracker information only (that is the z-vertex and driftchamber $R-\phi$ triggers), if they have no tracks from inside the H1 interaction zone or too many from upstream. Thus, the

¹⁴ 12648 events with a reconstructed vertex (figure 42(a)) only.

distribution dN/dz peaks at $|z_{\text{vertex}}| < 40$ cm more significantly than one would expect from the performance of the standard z-vertex trigger alone. Events rejected by L4 are not included in figure 42, but table 5 proves that they are suppressed by a factor of 22, thus would only improve the picture.

Event Class	Trigger (1)		$\cdot P_{\text{Peak}} \geq 2$	$\cdot P_{\text{Peak}} \geq 3$	$\cdot P_{\text{Peak}} \geq 3$ $\cdot W_{\text{Peak}} \leq 13$
L4-Reject (R_1 [Hz])	$\sigma_2 > 1.5$	4.38	1.50	0.50	0.20
	$(\sigma_2 > 1.5)\cdot\text{DC}$	1.70	0.92	0.27	0.15
	$(\sigma_3 > 1.4)\cdot\text{DC}$	0.96	0.37	0.06	(2)
L4-Keep (R_2 [Hz])	$\sigma_2 > 1.5$	4.66	2.31	0.96	0.76
	$(\sigma_2 > 1.5)\cdot\text{DC}$	2.21	1.74	0.81	0.73
	$(\sigma_3 > 1.4)\cdot\text{DC}$	1.52	1.15	0.52	(2)
DIS (A_1 [%]) (3)	$\sigma_2 > 1.5$	44	35	16	13
$c\bar{c}$ (MC) (A_2 [%])	$\sigma_2 > 1.5$	55	48	25	20
	$(\sigma_2 > 1.5)\cdot\text{DC}$	38	30	17	14
	$(\sigma_3 > 1.4)\cdot\text{DC}$	30	24	14	(2)
Quality factor $Q = A_1/(R_1+R_2)$	$\sigma_2 > 1.5$ DIS $c\bar{c}$	4.87	9.19	10.96	13.54
		6.08	12.60	17.24	20.83
	$(\sigma_2 > 1.5)\cdot\text{DC}$	9.69	11.28	15.74	15.91
	$(\sigma_3 > 1.4)\cdot\text{DC}$	12.10	15.79	24.56	(2)

- (1) σ_2 according to equation (2) on page 32, σ_3 according to equation (3), DC = at least one track with a small DCA found by the driftchamber (DC) R- ϕ trigger.
(2) Cuts on w_{peak} do not further improve this trigger.
(3) Due to the DC R- ϕ trigger becoming available only towards the end of the run period, no trigger efficiencies are available for combined trigger conditions. The efficiencies given for the z-vertex trigger are before cuts described in chapter 3.5.3 to suppress the influence of noise in the MWPCs. Shaded cells indicate particularly good performance.

Table 5: Efficiency of the *vertex estimator*

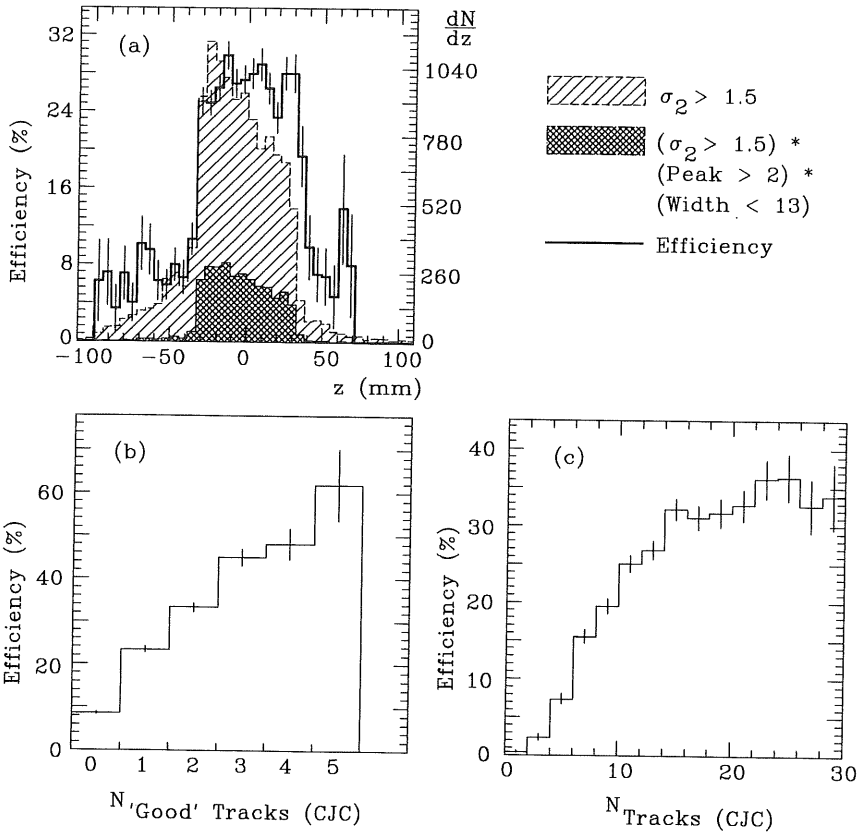


Fig. 42 (a) The vertex estimator tightens the cut on the z -coordinate of the event vertex. (c) The trigger efficiency becomes a direct function of the number of tracks found in the CJC. (b) 'Good' tracks cross at least CIP and COP, have a transverse momentum $p_t > 400$ MeV and a DCA < 50 mm. All efficiencies are given relative to a sample of events accepted by $\sigma_2 > 1.5$ (eq. (2), p. 32).

4 Hardware realization

4.1 Block diagram

As explained in chapter 3.1 and figure 7 on page 23, the *z-vertex trigger* receives a total of 1920 digitized and synchronized input signals. The block diagram of the trigger logic is given in figure 43. The *rayfinder* electronics builds the 16 histograms for the 16 φ -segments respectively. These individual histograms are summed up in the *adder cards* to one 16 bin wide histogram. The *vertex finder card* extracts some 'significant' numbers, which are passed to the *RAM card*. The latter is operated as a lookup table and produces the eight output trigger bits, each programmable to different levels of peak significance. These bits are passed to the L1 central trigger logic (CTL1), where a global trigger decision is derived. The *z-vertex trigger* bits are available 15 HERA bunch crossing clock cycles after the initial interaction, marked as 'BC 15' in figure 43.

4.2 The rayfinder electronics

The rayfinder electronics is distributed over 256 printed circuit boards, each building one histogram bin for one φ -segment. It has been discussed in detail in [46]. A four-fold coincidence defines a ray. For each bin and φ -segment, an average of 134 combinations of MWPC pads are examined. An adder cascade then calculates the number of active rays, which is passed to the adder cards as an 8 bit number.

Furthermore, the rays are grouped into *big ray candidates* according to the calorimeter *big towers* they are pointing to, which define regions in ϑ (and φ) (figure 10, p. 26). These candidates, 16 per φ -segment, have to be stored in a pipeline up to the moment where the peak finding logic on the vertex finder card has decided on the peak location in the histogram. Should the peak fall into the currently examined bin, they are validated by the *Bin Select* signal. Located on the crate backplane, 16 wired ORs combine all big ray candidates of all bins of one φ -segment, validated or not, and deliver the 16 *big rays* for that particular φ -segment, corresponding to 16 ϑ -regions. This information is passed to the *big ray distribution box*, shown in figure 58 on page 106, which makes it accessible to other triggers.

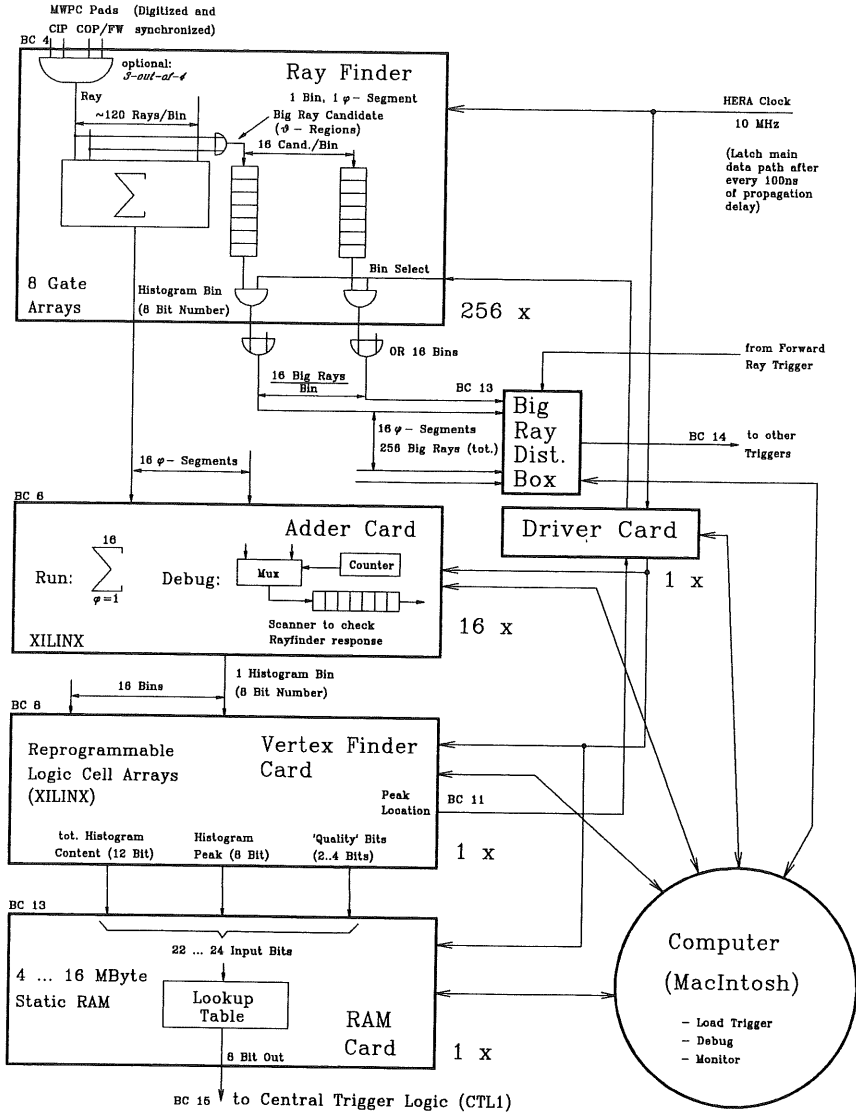


Fig. 43 Block diagram of the z-vertex trigger.

The rayfinder electronics is dominated by a huge number of coincidences and adder cascades, resulting in a relatively low gate count but high wiring density. It is therefore imperative to achieve an integration level as high as possible. We found that the circuitry of one rayfinder card is best distributed over eight to nine specially developed *gate arrays*. We use a 2200 gate-equivalent master from NEC in 1.5 μm CMOS technology [47]. Despite the relatively high development costs, we found that this solution was preferable to alternative designs employing standard TTL logic or analog adders. Advantages include overall price, total pin count (which simplifies board design and increases reliability) and low power consumption at the price of a slightly increased propagation delay. The rayfinder electronics requires 2112 gate array chips.

Additional benefits of the gate array solution were very flexible configuration options. Each ray R_j is defined as

$$R_j = (P_1 P_2 P_3 P_4 + x_1 P_2 P_3 P_4 + P_1 x_2 P_3 P_4 + P_1 P_2 x_3 P_4 + P_1 P_2 P_3 x_4) \cdot RENA_j \quad (18)$$

where P_i are the pad signals offered by the receiver cards, x_i programmable *preset bits* in the gate arrays, each associated with the respective pad signal P_i and $RENA_j$ a *ray enable register* uniquely associated to the ray R_j and again programmable in the gate array. The registers x_i implement a *3-out-of-4* option into which each pad can be included individually. As apparent from figure 7 on page 23, the pad signals P_i are given by $P_i = Ch_i \text{SwiLa}_i + TP_i \neg \text{SwiLa}_i$ with $i = 1..4$. Here SwiLa_i is a *switch latch register* on the receiver card, which selects the source of the receiver card output P_i as being either a pad signal Ch_i or a *test pattern* setting TP_i . It can be individually selected for each chamber pad and thus offers the following choices for P_i :

- permanently on (SwiLa off, TP on)
- permanently off (SwiLa off, TP off)
- chamber signal (SwiLa on)
- allowed to be missing in corresponding rays in cases where all other three pads of that ray are either permanently set *on* or the respective chamber pads have fired (register x_i set)

These options are used to adapt the rayfinder logic to not fully working chambers in case of

- noisy channels
- broken preamplifiers
- inefficient pads
- high voltage problems in some parts of the chambers

and allow to carefully balance trigger efficiency losses against increased background acceptance in such cases. The register REna allows to adapt the list of valid rays to the chamber behaviour as discussed in chapter 3.3.3.

Additional programmable registers control the ray to big ray relation inside a gate array. Each ray can be programmed to be included in up to five big rays, thus allowing overlap of the solid angles covered by individual big rays. This may be necessary as the big rays are for example used to validate calorimeter big tower energies. The shower profile of a particle entering the calorimeter close to a big tower boundary may however well leak into a neighbouring tower. Therefore, the corresponding ray should be capable of enabling more than just one big ray.

Other applications were kept in mind when developing the gate array and appropriate circuitry was included where possible. The chip can be used as an 8 bit wide serial in/serial out shift register with an externally selectable depth of one to eight clock cycles or as an adder for 31 1 bit numbers delivering a 5 bit result.

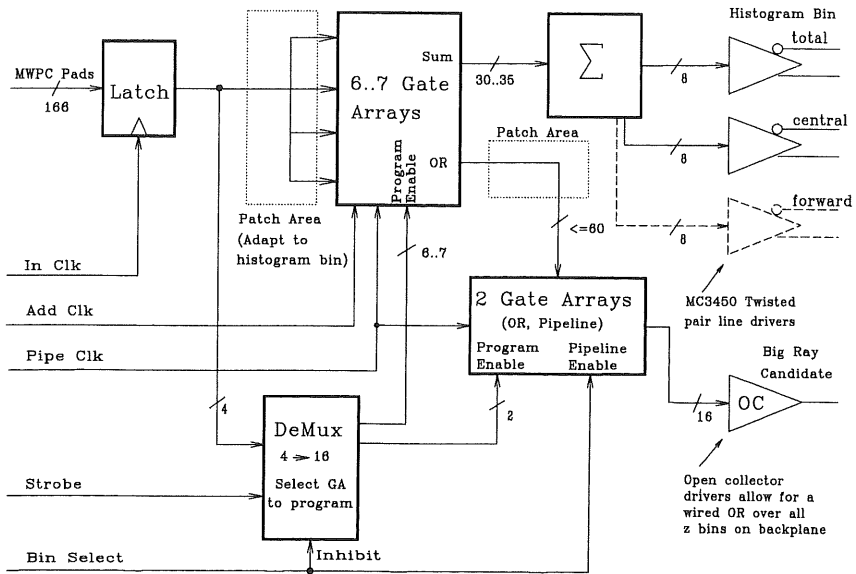


Fig. 44 Block diagram of the rayfinder printed circuit boards.

Figure 44 shows a block diagram of the rayfinder printed circuit boards. A total of 166 MWPC pads are latched and then distributed among six to seven gate arrays, which compose the histogram bin and big ray candidates. The number of rays found in each gate array - up to 31 - are added in a TTL adder cascade. It has separate outputs for the total bin content and the bin formed by rays from the central tracker only. An output for a histogram bin built from forward rays only is foreseen on the PCB, but not equipped with parts. The results appear as differential signals on two front panel connectors of the card. The big ray candidates are stored in a pipeline formed by two additional gate arrays until the *Bin Select* signal validates a particular histogram bin as containing the peak.

The rayfinder prints have no direct computer connection although each gate array contains a configuration memory of 236 bits is to be loaded upon power-up. Instead, we make use of the test pattern facility on the receiver card as shown in figure 7 on

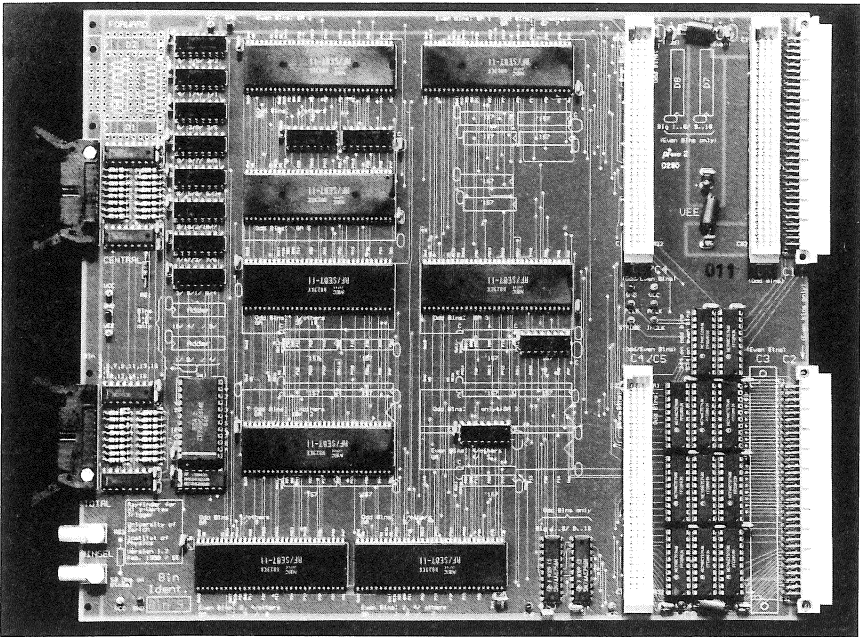


Fig. 45 The eight gate arrays dominate the rayfinder PCB. On the right, between the connectors, the input latches are visible. The lemo connector on the left is for the *Bin Select* signal. Above, the TTL adder cascade and the output drivers are found.

page 23. Some of the pad signals are dedicated to serve as address and data lines for the gate array configuration memory. Four others are used to ready the chip for programming via a demultiplexer. This approach minimizes additional logic needed for programming to just one chip, the demultiplexer, and one single *Strobe* signal to be cabled to the prints. However, the number of computer bus accesses needed to program the logic is much greater than the amount of useful information downloaded would suggest¹⁵.

4.3 The rayfinder backplane and rack layout

The 256 rayfinder prints are accommodated in eight crates, one for any two ϕ -segments. The prints have a dimension of 280·233 mm², corresponding to a 6 VU¹⁶ high board conforming to the euro-mechanics standard [48]. Two prints covering two histogram bins form a module with a width of 5 HU¹⁷. Each crate contains 2·8 such modules, leaving one slot free with a width of 4 HU. The pinning of the backplane connectors does not correspond to any industry standard. The backplane consists of a pair of prints. A passive part is responsible for distributing the signals to the rayfinder prints and the spare slot. The latter is equipped with two five-row euro-connectors, which make all pad signals available in the crate accessible to a possible future expansion card. An active print is piggyback mounted onto the passive backplane. It is responsible for receiving the differential pad signals from the receiver cards and making them available as standard CMOS levels.

With only two ϕ -segments located in the same crate, some pad signals need to be available to two neighbouring crates. This is caused by the eight-fold segmentation of the central inner proportional chamber and part of the forward chamber. Furthermore, mechanical constraints in the design of the latter made it necessary to group pad signals

¹⁵ A total of $1.8 \cdot 10^6$ bus accesses are needed to transport 61 kByte information! This increases the total loading time for the entire rayfinder electronics to about 10 minutes, which is dominated by the time needed by the controlling MacIntosh to translate the data to the format required by the hardware.

¹⁶ VU = Vertical Unit, 38.8 mm

¹⁷ HU = Horizontal Unit, 5.08 mm

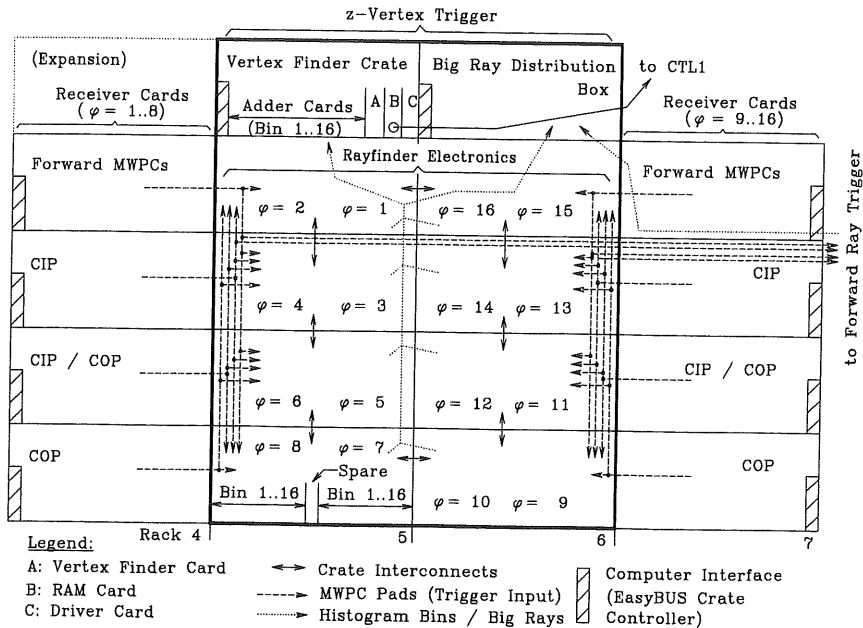


Fig. 47 Rack and crate layout of the z-vertex trigger.

unused computer controllable lines¹⁸, originating from one of the *fanout cards* [49] in the MWPC subsystem. One line is operated as a serial input to a shift register. The other is used as a clock.

A major problem when designing the trigger was the logistic task of distributing all chamber signals efficiently to the trigger crates. One has to keep in mind that all cables should have approximately the same propagation delay. The total of 1920 pad signals, which are examined per bunch crossing, result in a dataflow of 1.9 GBit/s! Figure 47 shows the rack and crate layout. The natural order for distributing receiver cards into crates is chamber oriented. The trigger on the other hand wants the signals sorted by φ -segments. These contradicting demands were met by distributing the crates such that chamber signals received in the receiver cards in rack 4 are only needed in trigger crates in rack 5. Similarly, rack 7 is linked to rack 6. The rayfinder crates form a ring such that crate interconnection cables never have to be longer than from one to a neighbouring

¹⁸ The so-called *Slow-3* and *Slow-4* signals of the fanout card are used for this purpose.

crate. Each rayfinder crate receives 17 cables with chamber signals from receiver cards and has 10 interconnections to each neighbouring crate. Furthermore, four big ray cables connect the crate to the big ray distribution box.

Figure 48 shows a side-view of a rayfinder crate. With a total of 41 twisted pair flat cables, containing some 800 signal pairs, connected to the back of the crate, the space between the power supply and the active backplane becomes more than crowded. Although the crates are mounted extensible in the racks, which facilitates access to the backplane, a failure on one of them requires at least a one-days work of unmounting and remounting the defective part! A power supply location below the backplane, just behind the ventilation and control unit, would greatly ease this process and maybe even allow for a mid-plane design, where active receiver cards are plugged to the back of an entirely passive though complex mid-plane. However, standard H1 crates do not offer this option [50]. Nor do the standard racks provide adequate room for cables in the back or offer any means for crate interconnections between horizontally adjacent racks [51]. When evaluating these parts, one has obviously not kept in mind that detector electronics, with their intrinsically high degree of parallelism, generally have a much

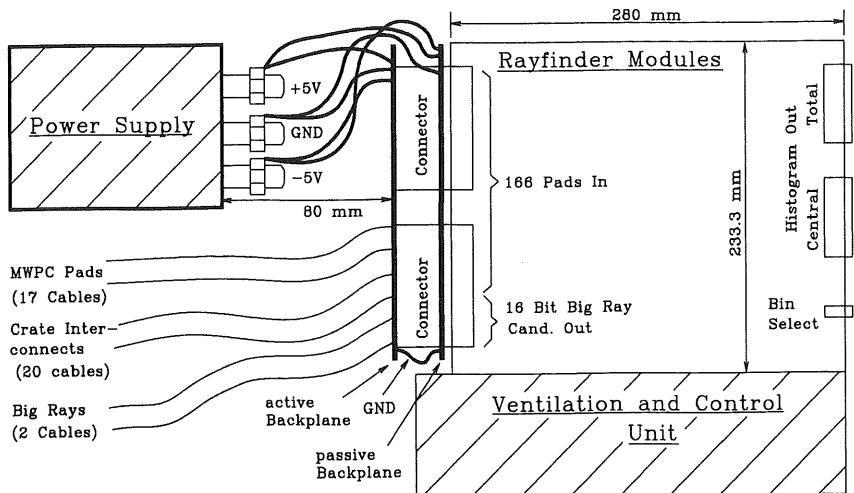


Fig. 48 Side view of a rayfinder crate. Due to the unlucky position of the power supply behind the backplane, insufficient space is available for cabling.

greater wiring density than ordinary industry applications placed in 19" racks, where highly intelligent units need only few links to the outside world.

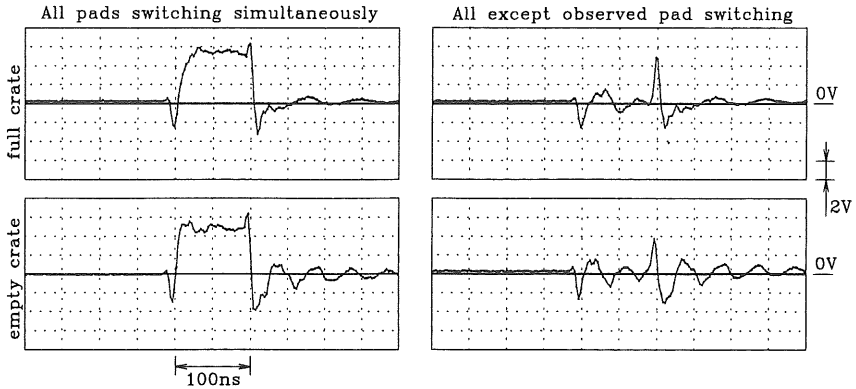


Fig. 49 The signal quality on the passive rayfinder backplane is critical due to ground bouncing between the active and passive backplane if all but one chamber pads switch simultaneously.

With 332 pads, 32 big rays and several steering signals travelling from the active to the passive backplane connected by four standard 96 pin euro-connectors, the inductance of the power lines has a major influence on the signal quality. With all pad signals switching synchronously, one can easily observe signals on the passive backplane, which are unstable for several tens of nano-seconds after the switching, as shown in figure 49. This is caused by the inductance of the ground connection between the two backplanes and commonly known as *ground bouncing*. Although short cables with a maximized surface keep the inductance as low as mechanically possible, a better solution would have been to use five-row connectors between the two backplanes, devoting two rows to ground only. With the current setup, *InClk* in figure 44 (p. 79) has to be delayed by some 20 ns in order to wait for stable conditions on the backplane.

4.4 The vertex finder crate

All the remaining trigger electronics except the *big ray distribution box* is located in a single *vertex finder crate*, which conforms to the EasyBUS standard, a custom designed bus used in the MWPC area of H1 only [52]. It is a subset of the VME standard, offering a 64 kWord address space per crate, which is mapped onto the address space of a master VME crate containing the front-end processor for the MWPC subsystem, and omits all interrupt services common to VME. It was chosen for its simplicity and the relatively cheap price per crate interconnection, since the front-end electronics including the receiver cards is distributed over 17 crates.

The 64 kWord address space of the vertex finder crate is divided into a 32 kWord page frame for loading and reading back the memory of the RAM card described below, and 2 kWord frames for the various functions of each of the 20 cards in the crate. The crate contains 20 cards in total:

- 1 EasyBUS Crate Controller
- 16 Adder Cards
- 1 Vertex Finder Card
- 1 RAM Card (8 HU wide)
- 1 Driver Card for clock and *Bin Select* distribution

The system description now follows the information flow backwards, i.e. from bottom to top in figure 43 on page 77.

4.5 The RAM card

Calculating the significance of a peak of a histogram typically requires operations such as divisions, square roots and other arithmetic operations to evaluate equations as discussed in chapter 3.2. Given the tight time constraints for these calculations ($< 1 \mu\text{s}$, taking into account the L1 decision time of $2.3 \mu\text{s}$, of which a large fraction has to be devoted to the histogram building), the only possible solution is a RAM lookup table.

In order to avoid dead time during refresh cycles, only the more expensive static RAM is suitable. The card was developed such that it can be equipped with 4 MByte at the beginning. With cheaper modules becoming available in the future, it can be

upgraded to 16 MByte, increasing the address space from 22 to 24 bits. Currently, we use 512k-8 bit modules from Hybrid Memory with an access time of 35 ns [53].

The input data for the lookup table describe the histogram which is to be analyzed. These data have to be prepared by the vertex finder card described in the following chapter and include:

- Total histogram content (12 bits)
- Number of entries in the peak bin (8 bits)
- *Quality bits* (2 to 4 bits) flagging special situations, such as the peak being in one of the outermost bins, which are outside the anticipated H1 interaction zone and should therefore not trigger, or a histogram having two non-adjacent bins with peak content.

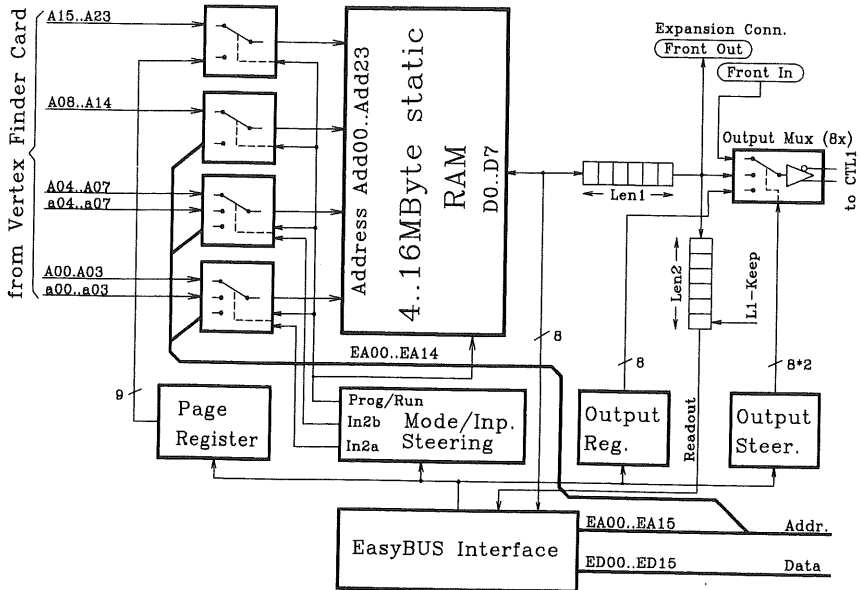


Fig. 50 Block diagram of the RAM card.

Figure 50 shows the block diagram. During the programming cycle, or when reading back the RAM content to the computer for test purposes, the entire address space is broken up by the *Page Register* into 512 pages of 32 kBytes each, which are then

mapped onto the EasyBUS address space . When operated as a lookup table, the address A00..A23 is provided by the vertex finder card. For increased flexibility, two groups of four address bits each may be switched to originate from a separate expansion connector labelled a00..a07.

The card generates eight bits of output. The source for each of them can be selected as either:

- the RAM output bit,
- permanently on, which can be used by a monitoring computer to flag the CTL1 logic a detected malfunction of the z-vertex trigger (chapter 5.4),
- permanently off, used to switch off currently unused or defective trigger bits,
- a front panel connector, used for future expansions. It allows fast switching between two neighbouring RAM cards, as a *Front Out* connector of one card could be directly connected to *Front In* of its neighbour. It also allows to change the source of some trigger bits to be something else than the RAM output.

The output can be delayed by up to eight bunch crossings by a pipeline with a programmable length *Len1*. This is needed to synchronize the trigger element input into CTL1 between the various L1 triggers. The RAM output value is also stored in a second pipeline, again with a selectable length *Len2*, such that the trigger elements are available for readout after a positive level one trigger decision has been broadcasted by *L1-Keep*.

4.6 The vertex finder card

It is the task of the *vertex finder card* to prepare the input values for the RAM lookup table described above. Furthermore, the peak position has to be communicated to the *Bin Select* inputs of the rayfinder cards. Despite the clear definition of these requirements, one wants to maintain as much flexibility towards future changes as possible. The *quality bits* may need redefinition, e.g. flagging other or additional special situations than initially foreseen. It may even be desirable to replace some high-order bits foreseen for the total number of histogram entries by additional quality bits. Furthermore, it is not immediately clear, whether only those *big ray candidates* associated with the histogram bin containing the peak should be validated, or also those originating from the immediate neighbours. The latter enables almost always the

candidates correlated with the true vertex location, as explained in chapters 3.3.3 and figure 34 (p. 61), at the cost of more wrongly tagged big rays.

XILINX Logic Cell Arrays offer both high integration and flexibility in the logic design, as they can be reprogrammed from a computer at any time. Appendix B further explains their architecture. The card design, generic to the task of analysing 16 8 bit wide inputs, is centred around four XILINX chips, as shown in figure 51. They can be configured from an associated computer such as the MWPC subsystem MacIntosh through the EasyBUS interface. The number of interconnections between the different XILINX chips has been chosen such that all circuits described in the following chapters can be accommodated on this board. They include

- the vertex finder logic,
- the adder card logic (see chapter 4.7),
- additional optional logic (see chapter 6.2 (*summing card*) and chapter 6.3 (*peak finder card*)),
- a scanner program to test the card inputs (see chapter 5.1) and
- a test pattern generator to test the RAM card connected to the vertex finder card (see chapter 5.2).

It is not always necessary to equip all chips on the board. The vertex finder card however makes full use of all chips except the ROM.

Figure 52 explains the circuitry used for finding the peak and its location within the z-vertex histogram, which is delivered to the vertex finder card from the adder cards. It makes use of the XILINX A1, A2 and C as indicated. The 16 bin wide histogram is divided into four sub-histograms of four bins each. For each of them, six comparators compare each bin with each other. Twelve output bits, two per comparator, are fed into a combinatorial logic in order to extract a four bit pattern flagging the bin(s) containing the same value as the biggest entry of the sub-histogram. It also steers a multiplexer which selects one of the bins containing the peak value. The four peak values, one for each sub-histogram, are fed into a similar unit. The peak value found in this second step obviously is the biggest entry in the original 16 bin wide histogram. The four bits flagging the peak location(s) are used to validate the respective bit patterns of the sub-histograms. The resulting 16 bit wide pattern flags each bin that contains a value equal to the peak.

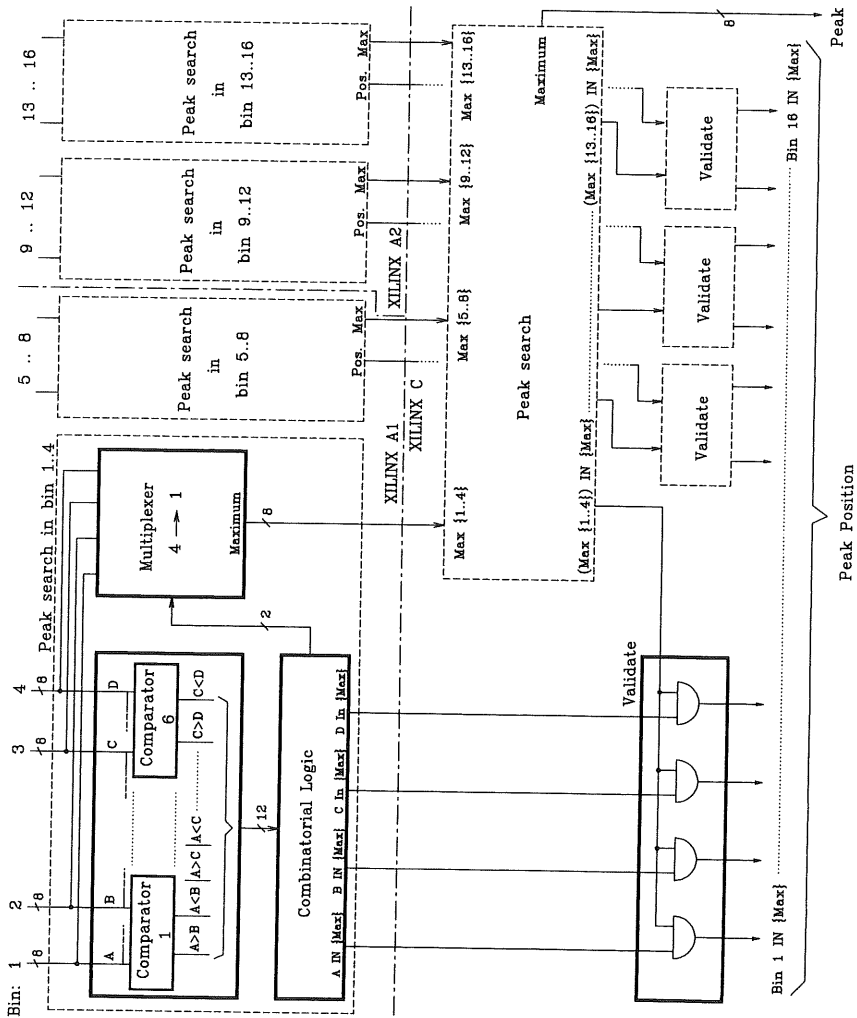


Fig. 52 Finding the peak of a 16 bin wide histogram is done by subdividing it into four parts of four bins each. The peak of each sub-histogram is found by comparing all bins with each other.

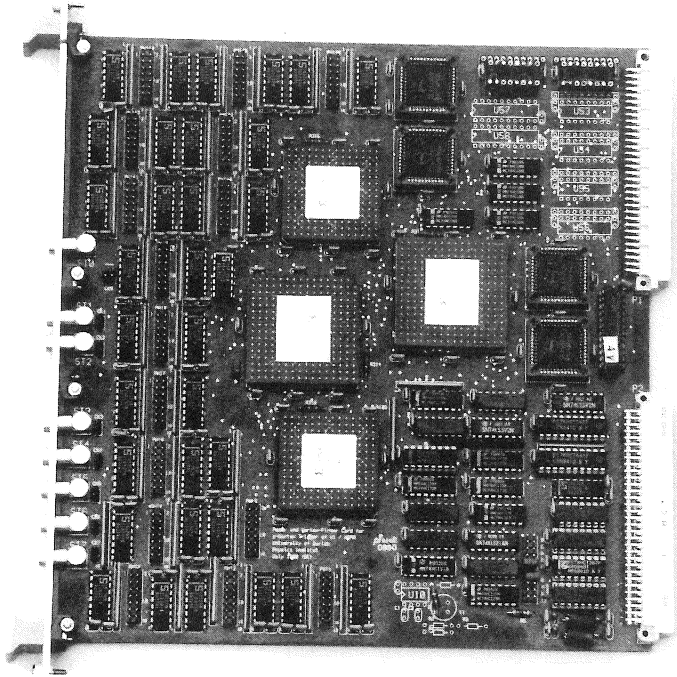


Fig. 53 The four XILINX chips clearly dominate the vertex finder card. In the lower right corner, one recognizes the EasyBUS interface. The input receivers occupy the left side. The empty positions in the upper right corner are foreseen for a 8-16 bit ROM with associated output drivers.

As only few of the *Configurable Logic Blocks* (CLB) of the XILINX C have been used for the above described logic¹⁹, it contains ample free space to accommodate logic for extracting the quality bits, and to modify the peak location bit pattern, which is eventually connected to the *Bin Select* inputs of the rayfinder cards, such that neighbours of bins containing a peak are also validated.

¹⁹ An 8 bit comparator can be built with just 7 CLBs, the 8-4 \rightarrow 1 multiplexer costs 12 CLBs and the combinatorial logic to steer it about 4 CLBs. Therefore, only about 58 of the 320 CLBs in XILINX C are used so far.

Currently, two quality bits are produced. One flags peaks in bins 1, 2, 15 and 16, as their respective locations along the beam axis are outside the nominal interaction zone for ep collisions, which should be restricted to $|z_{\text{vertex}}| < 25$ cm. The other marks histograms that are totally contained within four adjacent bins. This, in coincidence with a μ -trigger, should help tagging $J/\psi \rightarrow \mu^+\mu^-$ decays. Since the second quality bit cannot be totally derived from the information available in XILINX C, some of the six spare interconnections between XILINX C and A1 and A2 respectively are used to pass additional information as to where non-empty bins are located.

XILINX B is used to calculate a 12 bit sum representing the total histogram content. Since each input is represented by eight bits only, the sum can never exceed a value of $255 \cdot 16 = 4080 < 2^{12} - 1 = 4095$. Only eight bits are directly available at the card's backplane connector. The four high-order bits are looped through XILINX C. This gives the option to trade them in for additional quality bits.

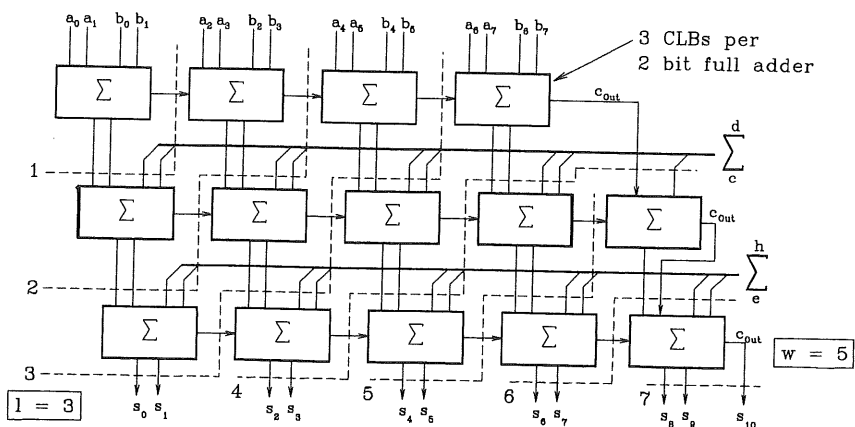


Fig. 54 The total propagation delay of the MSB of an adder cascade output is calculated as $t_p = l + w - 1$. l is the depth of the cascade and w the width of the last level. The dashed lines indicate constant propagation delay.

The adder cascade contains four layers of adders, the first one consisting of eight 8 bit units. The last one is formed of just one 11 bit unit delivering the 12 bit result. Three CLBs connected in parallel to the same inputs can be used to form a two bit full adder with look-ahead carry propagation. Wider units are best formed using the traditional ripple-through carry propagation technique. This is especially true for cascades of adders

as illustrated in figure 54, since the high order output bits of one layer are only needed *after* the carry signal from the low order bits of the subsequent layer propagated through. The total propagation delay for the MSB of a cascade output is therefore given by $t_p = l + w - 1$, with l being the time for the LSB to propagate through all layers and w the propagation delay of the *carry out* bit of the last (and widest) adder only. In our case, one finds $t_p = (4+6-1) \cdot t_{\text{CLB}}$ with t_{CLB} the propagation delay of one CLB (plus the associated net delays). The entire summation can be performed within two HERA clock cycles.

For debugging and monitoring purposes, each of the two XILINX B and C has a 16 bit wide pipeline associated with it, which is stopped upon *L1-Keep*. It can then be read out by the DAQ computer. The use of these pipelines is explained in chapter 5.

4.7 The adder cards

With the above described functionality of the vertex finder card, it is obvious that we don't need a different card to sum up the 16 ϕ -segment related histograms: Each of the 16 *adder cards*, which correspond to the 16 histogram bins, gets sixteen 8-bit figures as input, originating from the respective rayfinder cards. The output sum can theoretically be as big as $8 \cdot 255 = 4080$. This would call for a 12 bit representation. Experience from extensive Monte Carlo simulations however shows, that ep collision events never produce a histogram with a peak bin content of more than 255, which makes an 8 bit output feasible.

A wider output would not pose so much of a problem to the *adder cards*, which of course are the same printed circuit boards as the vertex finder card, with only XILINX B mounted and programmed, but to the latter, which would then have to deal with a histogram consisting of 16 12 bit numbers. This would increase the decision time, need many more CLBs²⁰ and explode the required RAM size on the RAM card to a fantastic $2^{12+16+2 \cdot 4} \cdot 8 \text{ bit} = 1.4 \text{ GByte}$, as the total histogram content would need a 16 bit representation.

²⁰ A 12 bit comparator requires 11 CLBs, arranged in four layers, as opposed to 7 CLBs in three layers for a 8 bit circuit.

XILINX B is therefore loaded with a slightly different version of the adder cascade program used on the vertex finder card: Only the low order 8 bits are produced and in the rare case of an overflow situation, the value 255 (\$FF) is delivered. This value would easily propagate through the peak finder logic to the RAM card as the peak bin content. The latter can then either communicate this situation to CTL1 as one of the eight trigger elements or locally reject or accept the corresponding event.

4.8 The driver card

The last card needing description in the vertex finder crate is the *driver card*. As the name suggests, it mainly consists of line drivers and distributes various signals throughout the z-vertex trigger system. For one, it has 16 front panel lemo connectors, each distributing the HERA clock signal. A computer-programmable delay line allows to individually adjust the relative clock phase of each of these outputs in 16 steps of 2 ns each [54].

Secondly, the *Bin Select* signals, originating from the vertex finder card, are distributed to the rayfinder modules. Alternatively, the 16 signals can be directly computer controlled, which is needed during the programming cycle of the gate arrays in the rayfinder electronics. Each signal is available on two separate front panel lemo connectors, as it needs to be daisy-chained through all rayfinder ϕ -segments, located in the two racks 5 and 6 of figure 47 (p. 83). One output is associated with one crate, thus limiting the total cable lengths.

All outputs are TTL compatible and allow a 50 Ω termination. Additionally, some general purpose I/O registers are available through the backplane connector, but are currently not used by the trigger.

5 Test procedures

5.1 The rayfinder electronics and the *scanner*

Testing the rayfinder electronics and ensuring its proper functioning is a non-trivial task. Not only does the great number of 256 PCBs defy extensive testing by means of conventional methods, but also the fact that the *rays*, the coincidences of four MWPC pad signals, are not accessible since they exist only inside the gate arrays. Available are numbers only, corresponding to the respective histogram bin content. Furthermore, the gate arrays need a lengthy configuration cycle of some 7000 EasyBUS accesses per rayfinder board before they can be expected to function properly.

Rather than going to great lengths trying to connect logic analyzers and oscilloscope probes at strategically important points within the logic, which would require extensive recabling procedures for each test to be performed, one can make use of the reprogrammability of the XILINX chips in the adder cards connected to the outputs of the rayfinder prints.

After having programmed all gate arrays, two test patterns can be presented to the trigger by means of the test pattern facility in the receiver cards, as sketched in figure 7 on page 23: With the SwiLa register loaded to the off-state, the pad signals arriving at the rayfinder inputs do not originate from the chambers but from the test pattern registers TP1 and TP2. Which one of the two is selected can be controlled by the *TP-Select* line, which in turn is either computer controllable through one of the fanout cards²¹ of the MWPC system, or can be steered by a pulser, synchronous to the HERA clock. A bad design of the receiver cards does not allow to toggle between the two test patterns with 10 MHz. It is however possible to select one test pattern for 2·96 ns, corresponding to two bunch crossings, and the other for just one clock cycle. These test patterns propagate through the *rayfinder cards* and arrive at the adder card inputs. Thus, each adder card sees 32 input states, each 8 bit wide, corresponding to the 16 ϕ -segments connected to it, times the two test patterns applied.

²¹ For each the central, forward and backward MWPCs, one *fanout card* is responsible for the HERA clock (*HClk*), *Pipeline Enable* and *Slow* signal distribution. The *TP-Select* signal corresponds to the *Slow-2* output of these cards [49].

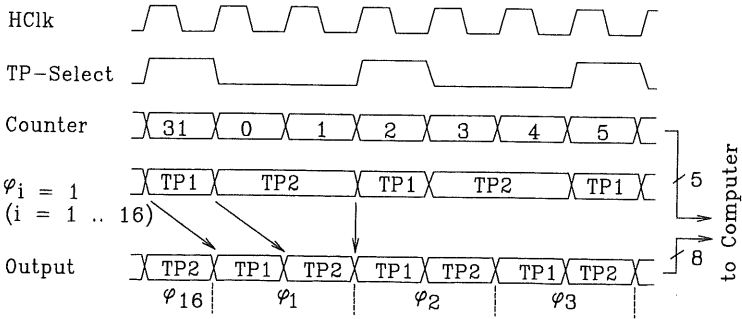
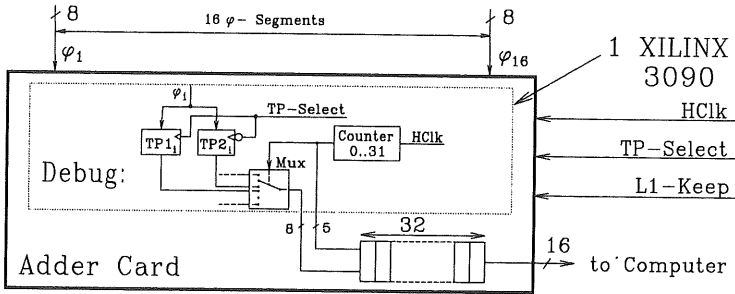


Fig. 55 A special *scanner* program is loaded into XILINX B of the adder cards for testing the rayfinder electronics.

A special XILINX program (figure 55) located in chip B (see figure 51, p. 89), the so-called *scanner*, contains a five bit counter, which is increased by the HERA clock frequency *HClk*. It steers an 8 bit wide 32→1 multiplexer, which makes 32 registers available to the output, each for one clock cycle. Any of the 16 ϕ -segment inputs are connected to two of these registers, and loaded into them by *TP-Select* and \neg *TP-Select* respectively. Thus, all 32 input states are available at 8 XILINX output pins within 32 clock cycles. They are then fed into a pipeline 32 levels deep. Stopping it at any randomly chosen moment by means of switching *L1-Keep*, which again originates from the fanout cards and is computer controllable, allows reading back all input states by completely emptying the pipeline. For this purpose, it can be advanced by the computer while *L1-Keep* is asserted. To uniquely relate the 32 states to the corresponding inputs, also the five bits representing the respective counter status are fed into the readout pipeline, which is 16 bit wide. Three bits remain unused.

Thus, using the MacIntosh steering the whole system (figure 43, p. 77) one can perform complete tests of the rayfinder electronics. The program knows which configuration was loaded into the gate arrays, knows which test patterns were presented to the trigger and can read back all outputs of the rayfinder prints. These outputs can then be compared to the simulated trigger response. Being able to read back the counter of the *scanner* correctly is a good indication of a properly working adder card. Any possible discrepancy to the expected result must then be explained by a misbehaviour of the electronics in front of it. Malfunctioning of the digital part of the receiver cards can be excluded by reading back their pipelines, which of course must contain the test patterns loaded.

Once an error has been detected, tracing it to a single defective chip involves manual intervention. The control program on the MacIntosh supports this procedure by being able to display any of the 2112 installed gate arrays of the rayfinder modules on-screen, with expected signal levels for each pin. This is true for both the programming phase of the gate array configuration registers and for test pattern runs as described above. It is necessitated by the fact that rayfinder cards can hardly be debugged in a workshop environment, as more than 166 input (pad) signals are not only needed for checking the correct operation but also during the configuration phase. Rather than duplicating large parts of the electronics and software environment, we opted for highly advanced debugging tools allowing to trace errors down to chip levels in the 'real' environment.

Not only can the *scanner* program be loaded to the 16 adder cards, but also to the vertex finder card. Then, the adder cards are operated in their standard configuration as summing units. This allows scanning the final z-vertex histogram and fully includes the adder cards to the chain tested. Detected errors however can in this case only be related to histogram bins but not to a single rayfinder card.

- Test patterns used for these tests originate from various sources including
- manual entry through a graphical interface showing all MWPC pads,
 - randomly generated patterns with a selectable average occupancy of the chamber pads,
 - patterns read from a file and
 - automatically generated patterns.

The file input mode allows feeding any Monte Carlo simulated event into the trigger or even replaying events from previous run periods. This may be useful in cases where the trigger response cannot be reconstructed from the MWPC pads fired. It is then possible to rerun such an event through the hardware and trace possible bugs. Automatically generated patterns allow to test the hardware over an extended period of time.

5.2 Testing the RAM card

Reading back the content of the RAM card to the computer ensures, that each cell contains the programmed value correctly. It does however not prove, that the card also works properly in the data taking mode, where the timing situation of most steering signals is entirely different to when the card is under computer control. On the other hand, it is impractical to let test patterns from the receiver cards propagate through the whole trigger logic to the RAM card for testing the latter. There is no simple algorithm available to calculate trigger inputs, such that they produce a particular histogram with which one wants to test the lookup table.

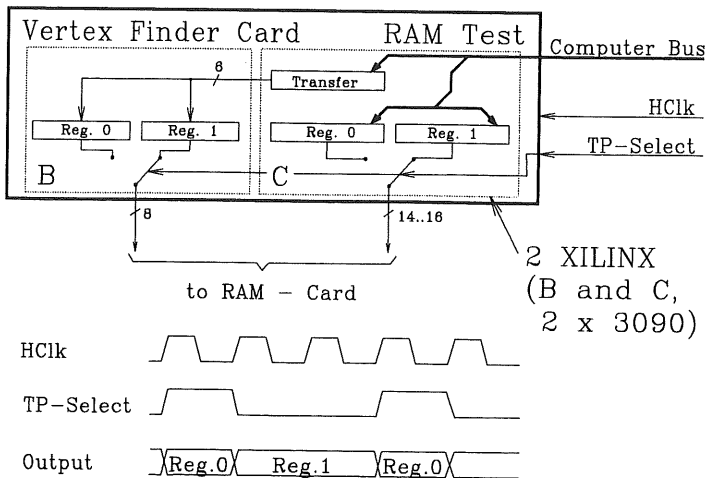


Fig. 56 The RAM card can be tested by loading computer programmable registers into XILINX B and C of the vertex finder card.

Again, we can make use of the reprogrammability of XILINX chips on the vertex finder card. All 22 to 24 bits arriving at the RAM card address lines during normal trigger operation originate from the vertex finder cards XILINX B and C (figure 56). The latter has eight pins connected to EasyBUS address lines and four to data lines, which allows one to program some registers into chip C, which can be made directly accessible to the computer. This feature is used to load two test patterns into XILINX C (and by means of the seven bidirectional interconnections between C and B also into B²²), which can then be made available to the RAM card. Switching between the two patterns is steered by the same *TP-Select* signal, which has to be present on the vertex finder card for steering the *scanner* program described in the previous chapter.

A second concern operating the RAM card arises from the fact that algorithms used to evaluate the peak significance of the z-vertex histogram may change with experiences gained from physics runs of HERA. This requires recoding the appropriate routine in the controlling and configuration program responsible for loading the lookup table. Since any data read back from the RAM card is compared with the expected response calculated by this very same routine, coding errors are particularly hard to detect. The situation is aggravated by the nature of the code needed, which is essentially a bit-sorting task.

To better control this error source so much related to human imperfectness, two subroutines are available in the control program. Each is supposed to calculate the same lookup table but they both should be coded by independent programmers. Running the two routines against each other discloses any discrepancies immediately.

²² 2·8 bits need to be transferred. They are subdivided into 4·4 bits. Four interconnections are dedicated as data lines, one plus *TP-Select* (which is available to both XILINX and constantly pulsing), operate as address lines and one interconnection is asserted during an ongoing data transfer. This operation is initiated by a write access to one of the EasyBUS address locations inside XILINX C and synchronized by *HClk*.

5.3 Difficult error conditions

The test patterns of the receiver card are fed into the normal signal path even before synchronization with the HERA clock. This ensures that the digital part of the entire MWPC system is *exactly* identical during tests and running periods. Any error that was not detectable with the tests described above must therefore have one of the following reasons:

- Very rare error. The automatic tests of the rayfinder hardware are limited by the speed of the controlling computer, which has to simulate the entire trigger in order to evaluate the response. The currently used MacIntosh II is capable of simulating about two events per minute. Overnight tests therefore run over some 1500 events. Errors that manifest themselves with a much smaller frequency will not be detectable. Hard errors, i.e. errors related to a source which is permanently bad, such as a broken cable, cannot belong to this category.
- Crosstalk and ground bounce related errors. With 1920 MWPC pads analyzed by the trigger, only a negligible subset of all possible 2^{1920} possible states can be checked. With the limited signal quality on the backplane of the rayfinder crates due to *ground bouncing* as described in chapter 4.3 it cannot be excluded that some unlucky combinations of circumstances lead to errors. Worst case situations such as all pads but one switching simultaneously have however been tested successfully. Errors of this category should be traceable by replaying events from data taking runs.
- Noise related errors. The H1 hall is an electronically very noisy environment. The noise situation is also different during test periods and run periods when all systems are running simultaneously. Although the trigger is a fully digital system, errors due to noise pickup cannot be fully excluded.
- Chamber and analog electronics related errors. As most other complex systems, the trigger follows the 'garbage in, garbage out' rule. Errors of this category can only be found by monitoring the chamber behaviour on a statistical ground.
- New errors. Errors only evolving during run periods can of course not be detected beforehand. Most likely, such errors are related to shifts of the timing of some signals relative to the HERA clock phase. Even with the temperature in the racks being stable to within about 5 °C, shifts of 7-10 ns on some clock lines have been observed over a period of a couple of months. With an allowed window of

sometimes only a few nano-seconds for a particular clock phase²³, this may cause harm.

All these error conditions call for a careful online monitoring as described in the following chapter. Furthermore, one would wish that clock phases could not only be set by the computer (as done on the driver card described in chapter 4.8) but also monitored by some strategically distributed *time to digital converters* (TDC). This would drastically reduce possible error sources, as experience shows.

5.4 Online monitoring and diagnosing

Monitoring the behaviour of the trigger over a long period of time can be subdivided into two main tasks: One is to ensure that the trigger operates as a fully predictable digital system. Given a certain input, a particular hit pattern in the MWPCs, the logic must produce a predictable result. The second, more difficult task is to monitor the input, the chamber response to certain classes of physics and background events. Constantly monitoring hit patterns, timing distributions and the noise, gas and high voltage situation of the chambers is part of this effort. We shall concentrate on the first task in this chapter.

The trigger input is available offline, as all pad signals are not only sent to the rayfinder electronics, but are also stored in pipelines on the receiver cards, as shown in figure 7 on page 23. These pipelines are read out upon *L2-Keep* and added to the event data. It is then possible to recalculate all eight z-vertex trigger bits delivered to CTL1. The sensitivity for detecting errors is however limited, as a single missing bit in the input of one of the adder cards for example does not necessarily influence the result of the significance criteria programmed into the RAM card. On the other hand, it would of course change the shape of the histogram presented to the vertex finder card. Thus, adding each of the 16 histogram bins to the event data through reading out the pipelines located on the adder card, as shown in figure 57, allows a much more sensitive test.

²³ The allowed window for a clock phase is given by $t_w = 1/f - t_{\text{Skew}} - t_{\text{Skew}}^{\text{Clk}} - t_{\text{Setup}} - t_{\text{Hold}}$ with f being the clock frequency and t_{Skew} the maximum skew between any two signals to be clocked. $t_{\text{Skew}}^{\text{Clk}}$ is the skew originating from the clock signal distribution. t_{Setup} and t_{Hold} are the setup and hold times of the synchronization register.

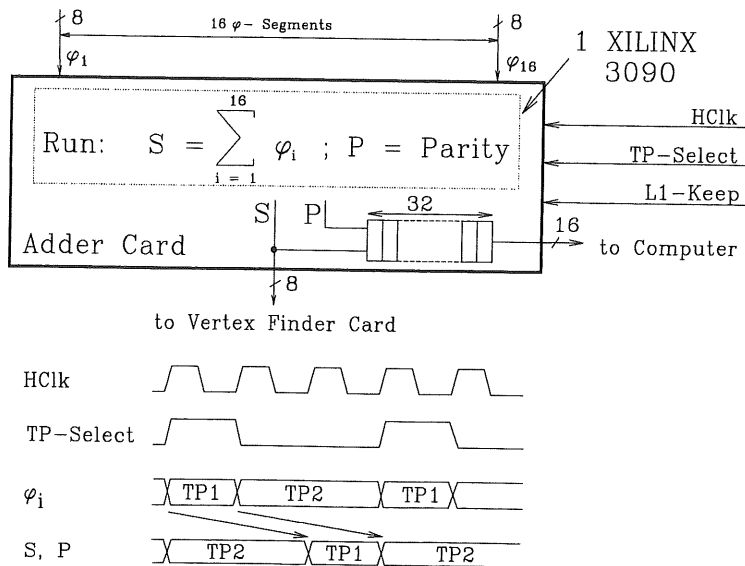


Fig. 57 The XILINX program loaded to the adder cards during normal trigger operation not only calculates the sum of the 16 inputs but also delivers six parity bits allowing detailed online monitoring of the rayfinder and adder cards.

Comparing the 16 histogram bins to the ones recalculated from the MWPC hit data also allows to better locate any possible error. At least the misbehaving bin can be tagged - if the cause of the error is located somewhere within the trigger electronics and not in the receiver card readout chain. An even better analysis can be made if the entire width of the adder card pipeline is put to use. It was chosen to be 16 bit wide, matching the EasyBUS data path. Eight bits are devoted to the histogram bin content, one is permanently connected to the *TP-Select* signal used by the scanner XILINX program (see chapter 5.1) and one is driven by XILINX A1 not equipped on the adder cards²⁴. The remaining six bits can be used for monitoring purposes to improve the error location capability.

²⁴ There is no particular reason to relate this 16th bit to XILINX A1. However, there were no additional I/O pins available on XILINX B to connect it to. Of the 144 pins, 128 are used as inputs for the histogram and one is used as a clock input. The remaining 15 signals are all attached to the pipeline.

An error occurring on one of the rayfinder cards would most probably flip the parity of the bin content delivered to the adder card. The six monitor bits are programmed to be combinations of these parities. With just one of the 16 cards misbehaving, five bits are needed to uniquely flag it. The sixth bit can be used to detect situations with errors occurring on two cards simultaneously.

Bit / Bin	1	2	3	4	5	6	7	8	9	10	11	12	13	14	15	16
0									1	1	1	1	1	1	1	1
1	1	1	1	1	1	1	1	1								
2	1	1	1	1					1	1	1	1				
3	1	1			1	1			1	1			1	1		
4	1		1		1		1		1		1		1		1	
5		1				1				1			1		1	1
Err. Vect.	30	46	22	6	26	42	18	2	29	45	21	5	57	9	49	33

Table 6: Parity bit allocation.

Table 6 explains the allocation of the six parity bits to parity flips of the 16 inputs. If one of the input bins change parity, the bits having 1 in the corresponding column are negated. With the help of this table, all parity bits can be calculated from the inputs to the adder cards. The bitwise exclusive OR of this number, calculated offline, and the one produced online, in XILINX B of the adder card, can be interpreted as a six bit error vector. Zero represents agreement.

As an example, lets assume a parity error in bin 6. This causes the parity bits 1, 3 and 5 to flip. The error vector, $101010 = 42$, is unique to this situation as long as the assumption holds, that only one or two inputs have changed parity. The error vectors associated with parity errors in two inputs are distributed such that the faults can be attributed to any of just four pairs of inputs. Assume the vector to be $010100 = 20$. This can be explained by errors in either the bins 3 and 8, 4 and 7, 9 and 14 or 10 and 13. If one has to assume more than two bad inputs, the errors can no longer be located.

It would be possible to run a monitor program on a processor installed in parallel to the one responsible for coordinating the data read out of the MWPC system. It would

perform the above described tests on a subset of events. In case of a detected malfunction, it could not only inform the operator on the central data acquisition console of H1 immediately, but also shut off the z-vertex trigger automatically by disabling its output bits through the output steering option of the RAM card shown in figure 50. It could also notify CTL1 through a dedicated trigger bit and thus influence the level one trigger mask. The system not only allows a fast error detection but can also pinpoint a single defective printed circuit board under most conceivable conditions.

6 Expanding the z-vertex trigger

6.1 Big rays and the big ray distribution box

Big Rays as introduced in chapter 3.1 are not only created by the z-vertex trigger, but - for small angles ϑ - also by the *forward ray trigger*. The purpose of the *big ray distribution box* (BRDB) is mainly to merge these two big ray sources in areas where they overlap and to distribute them to the various consumers.

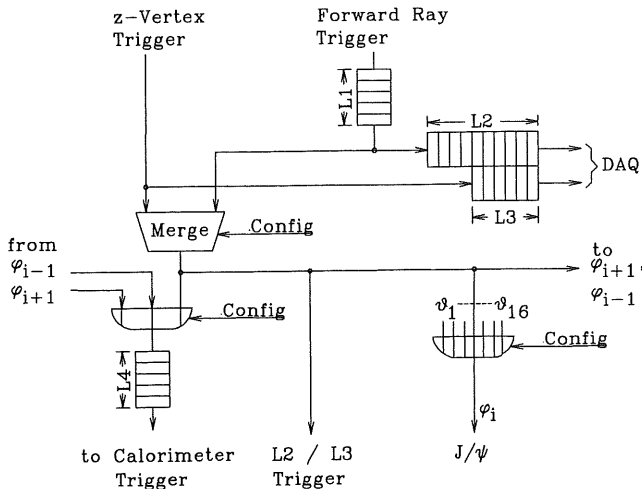


Fig. 58 The purpose of the big ray distribution box is to distribute the signals to various consumers, each with different electrical input specifications.

Figure 58 sketches the functionality of the BRDB [55]. The big rays originating from the z-vertex and forward ray trigger are merged where appropriate. Several software-selectable options are available:

- logical AND between the two signals,
- logical OR between the two signals,
- only the z-vertex big ray or
- only the forward ray trigger big ray.

Independent of this merging, both signals are stored in pipelines such that they can be read out by the DAQ upon *L2-Keep*.

The merged big rays are made available to L2 and L3 triggers through interface cards standardized within H1. They have a granularity of 16 ϕ -segments times 16 areas in ϑ . The latter correspond to the calorimeter big tower segmentation shown in figure 10 on page 26.

An additional output is foreseen to combine big ray information with calorimeter big tower energies already at the first trigger level. Within the calorimeter electronics, it is foreseen to set a threshold on the number of big towers which are validated by the corresponding big ray and contain an energy above a certain threshold. For that purpose, the ϕ -segmentation has to be adapted to the one of the calorimeter, which in a few cases is 8 or 32-fold.

A charged particle described by a big ray may not only deposit energy in its directly correlated big tower but also in its neighbours due to the shower profile leaking into them and the particle being deflected by the magnetic field inside the H1 tracker. The latter leads to low energy cutoffs along the lines discussed in chapter 3.3.1. Thus, it may be desirable to enable neighbouring big rays in ϑ and ϕ . The first is easily achieved by means of the programmable OR integrated into the rayfinder gate array described in chapter 4.2. In ϕ however, only the BRDB has available all necessary signals, since the rayfinder electronics is grouped by ϕ (and histogram bins). Thus, it contains a programmable OR to perform the enabling of the neighbouring ϕ -segments.

One ' J/ψ ' output per ϕ -segment is foreseen, which is realized as a programmable OR over all big rays of that segment. It is thus possible for a simple topological unit connected to these 16 signals to search for $J/\psi \rightarrow \mu^+\mu^-$ candidates, which can be identified by exactly two signals obeying $\Delta\phi = \pi$ [27]. Big rays corresponding to very small angles ϑ might need to be excluded due to their high rate. The programmable OR offers the additional possibility of selecting just one big ray per ϕ -segment, which might be useful for debugging purposes.

The BRDB is realized on 16 PCBs, one per ϕ -segment, and located in a separate crate. The configuration options and readout pipelines are accessible through an EasyBUS interface common to the H1 MWPC electronics. Various pipelines with adjustable lengths are included to synchronize the signals with each other in units of full HERA clock cycles.

6.2 Extended peak significance criterion

Evaluating the peak significance of the z-vertex histogram according to equation (1) rather than (2) (chapter 3.2) requires evaluating $s^2 = (\sum c_i^2 - nb^2) / (n^2 - n)$, the standard deviation of the average number of background histogram entries $b = \sum c_i / n$ ($i \neq j$ (peak bin), $n=15$).

Firstly, we shall release the condition, that s is calculated from all *but* the peak bin contents. Thus, we allow $i = j$ and denote the resulting standard deviation with s_1 . The adder cards, shown in figure 51 (p. 89), contain sockets for an 8·16 bit ROM, which can be programmed to calculate the square of each histogram bin content c_i . A hardware implementation of (1) is then possible, as shown in figure 59.

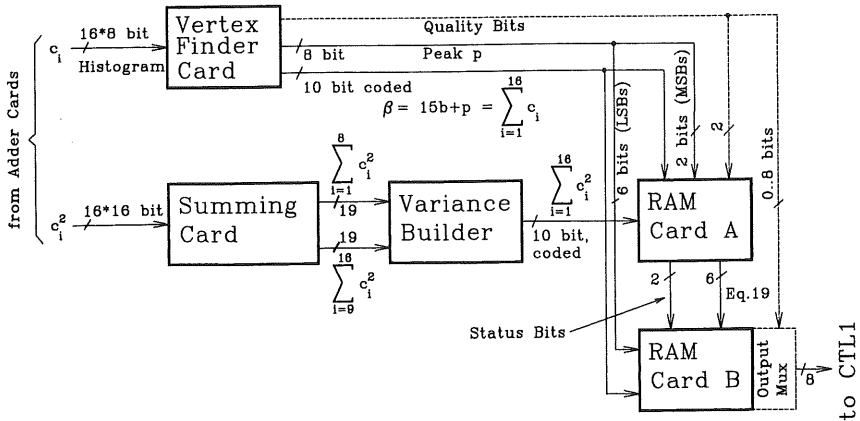


Fig. 59 The vertex finder electronics can be extended to calculate the peak significance according to equation (1) rather than (2) as discussed in chapter 3.2.

A new summing card calculates $\sum c_i^2$. The adder card design can be used for this purpose. Each of the two XILINX A1 and A2 calculates $\sum c_i^2$ with $i = 1..8$ and $i = 9..16$ respectively. The result, two 19 bit numbers, are delivered to a variance builder, which adds them up and codes the result to a width of just 10 bits, suitable as an input to a RAM card identical to the one described in chapter 4.5. This same card *A* also receives $\beta = 15b + p$, coded to a width of 10 bits only, and the two most significant bits (MSB) of p . These numbers originate from the vertex finder card described in chapter 4.6. Equation (1) can be reformulated as:

$$\begin{aligned}
 p &< \frac{225}{512} \cdot x_1^2 + \frac{\beta}{16} - \frac{15}{512} \sqrt{225x_1^4 + 64x_1^2(\beta + 16s_1^2)} \quad \text{or} \\
 p &> \frac{225}{512} \cdot x_1^2 + \frac{\beta}{16} + \frac{15}{512} \sqrt{225x_1^4 + 64x_1^2(\beta + 16s_1^2)}
 \end{aligned}
 \tag{19}$$

Thus, the lookup table *A* calculates the MSBs of the right sides of the above inequities and compares them with the MSBs of *p*. It might well be that these comparisons already exclude one of the above conditions, in which case the corresponding *status bit* is set to 0 and the right side of the other inequity is sent to RAM card *B* as a six bit number. If it is not possible to exclude any of the conditions of (19), the square root only is sent to *B*, and both status bits are set to 1. The coding scheme for these floating point numbers might well make use of the knowledge of the size of β for increased precision.

The lookup table *B* receives eight bits from *A* plus the six least significant bits of *p* from the vertex finder card. It also needs β , again to 10 bit accuracy. *B* delivers the trigger bits to CTL1. There is no room in this scheme for *quality bits* to mark special trigger conditions except by producing them elsewhere and feeding them directly to CTL1 as trigger bits, using the front panel input connectors of card *B*.

So far, s_1 was calculated by running the respective sums over *all* histogram bins, including the peak bin *j*. To exclude the latter from the calculation of *s*, equation (19) can be modified by replacing s^2 with

$$s^2 = \frac{\sum_{i=1}^n c_i^2 - p^2 - \frac{(\beta - p)^2}{n-1}}{(n-1)^2 - (n-1)}
 \tag{20}$$

in equation (1), which is then solved for *p*. *n* is the number of histogram bins, $n = 16$.

6.3 Building a vertex estimator

Making use of the rayfinders capability of estimating the primary vertex location along the beam axis independently for each ϕ -segment, as suggested in chapter 3.6.1, can easily be accomplished by duplicating some already existing hardware.

According to figure 40 on page 70, each z-vertex sub-histogram, one per ϕ -segment, has to be analyzed in a *peak finder* card, which delivers a 16 bit wide pattern. Each bit is set to 1, if the corresponding bin is a peak of the sub-histogram. The vertex finder card, as described in chapter 4.6, is designed for this purpose. In the context of the vertex finding, it has to deliver the *Bin Select* signals to the rayfinder modules in order to validate the big ray candidates of the peak bin(s). The peak finder cards however do not need XILINX B, as it is responsible for calculating the total histogram content, a function not needed here.

One peak finder card corresponds to one ϕ -segment. They reside in a crate similar to the vertex finder crate. Similarly, the adder cards correspond to a z-vertex histogram bin each. This poses a logistics problem, as every rayfinder output has to be cabled to two different cards in two neighbouring crates. They both receive a total of 256 twisted-pair cables with eight signal pairs each through front panel connectors. Electrically, it is easily possible to drive two receivers from with one MC3450 differential line driver as used on the rayfinder cards. Theoretically, both ends of such a line should be terminated with a 60Ω resistor against ground or 120Ω between the two lines. Given that these resistors are soldered into the rayfinder and adder cards, the peak finder would need to be located between those two cards, which is almost impossible due to lack of space. Experience however shows, that terminating lines at three rather than only two locations does not endanger the signal quality²⁵. It is therefore possible to place the rayfinder cards between the adder and peak finder prints which leaves more space for cables.

The 256 output bits of the peak finder cards are analyzed by two *summing cards*. Again, we make use of the vertex finder card design, which has 128 differential inputs.

²⁵ The output current of a MC3450 is only insufficient under *worst case* conditions. Replacing weak drivers with individuals meeting *typical* values provides a sufficient security margin for save data transfers.

Enough capacity is available in XILINX B to sum up the bit patterns presented by the peak finder cards. Each card ($i = 1, 2$) therefore has available one half of the vertex estimator histogram, from which it can calculate the peak bin content $p_{\text{Peak}, i}$ ($\leq 16, 5$ bits), the positions of the left- and rightmost non-empty bins ($0 \leq l_i, r_i \leq 7, 3$ bits each) and the total number of entries $b_{\text{Peak}, i}$ ($\leq 128, 9$ bits). Card one communicates these numbers, 20 bits in total, through XILINX C and the bidirectional backplane connections to card two, which can then return p_{Peak} ($\leq 16, 5$ bits), w_{Peak} ($\leq 16, 5$ bits) and b_{Peak} ($\leq 256, 9$ bits²⁶) describing the entire vertex estimator histogram. 19 backplane output pins are needed for these numbers. The 40 pins available thus provide enough connectivity.

Simple cuts on p_{peak} and w_{peak} can be performed inside XILINX C of summing card two, even with computer selectable thresholds, as some address and data lines of the EasyBUS are directly available in the chip. Cutting on σ_{Peak} according to equation (2) (p. 32) however would require an additional RAM card operated as a lookup table addressed with p_{Peak} and b_{Peak} . The new trigger elements can either be sent directly to CTL1 as additional information, or, in case they should replace some bits previously derived inside the RAM card of the vertex finder crate, looped through the output multiplexer of that card.

Only the crate backplane for the new vertex estimator crate and the XILINX programs residing in the summing cards need new development work. The backplane has to rearrange the output bits of the peak finder cards and make them available as differential signals such that they can be connected to the summing card inputs.

²⁶ One might choose to represent b_{Peak} by 8 bits only, disregarding the pathological case of $b_{\text{Peak}} = 256$.

7 Summary and Conclusion

The z-vertex trigger discussed herein has been operated successfully throughout the 1992 run period of HERA. Despite its complexity - it examines as many as 34400 rays simultaneously and still maintains a large degree of flexibility through many programmable options - its reliability was more than satisfactory.

This is largely a result of the sophisticated test and debugging tools available (Chapter 5). They allow a fast and complete test of the entire digital part of the electronics. It is even possible to replay any recorded or simulated event through the actual hardware, from the synchronizing circuit to the trigger output.

Although the trigger decision is based on the evaluation of a histogram, which, by definition, contains many entries not related to an actual particle track, its resistance against incoherent noise within the underlying multiwire proportional chambers is surprising (Chapter 3.3.4).

Despite the large range of possible crossing angles between particle tracks and the chamber planes ($6^\circ < \vartheta < 155^\circ$), the trigger acceptance is largely independent of ϑ , as shown in chapter 3.3.3 and 3.4.

Comparisons between independently triggered data samples and Monte Carlo simulations, as done in chapter 3.5.3, indicate a good understanding of the trigger behaviour. Therefore, z-vertex triggered events could be used for the measurement of a total photoproduction cross section σ_p^{tot} (Chapter 3.5.4 and [10]).

The trigger still has some potential to improve the ratio between accepted ep events and rejected background interactions by means of some comparatively simple hardware extensions. They are suggested and discussed in chapter 3.6 and 6.3. The gain is particularly impressive, if the z-vertex trigger can for one reason or another *not* be run in coincidence with the driftchamber R- φ trigger.

Appendix A: Pipelined triggers

Figure 60 explains the basic principle of a pipelined trigger. The digitized data is fed into a *pipeline*, a serial-in-serial-out shift register. If the setup and hold times - the time for which the data has to be stable before and after the relevant clock edge - is small compared to the time difference between two consecutive clock cycles, one may include data reduction logic between any two registers of the pipeline. If the pipeline is long enough, the functionality of all these individual reduction steps sums up to a complete trigger logic, delivering the *L1-Keep* signal. It is used to gate the clock of a data pipeline in which the original detector information has been stored whilst the trigger decision was evaluated. Once this pipeline is halted, the read-out process starts, which finds the detector information responsible for the positive trigger response in the last register of the data pipeline. If no trigger occurs, the pipeline continues running and a decision based on the consecutive bunch crossing is delivered one clock cycle later.

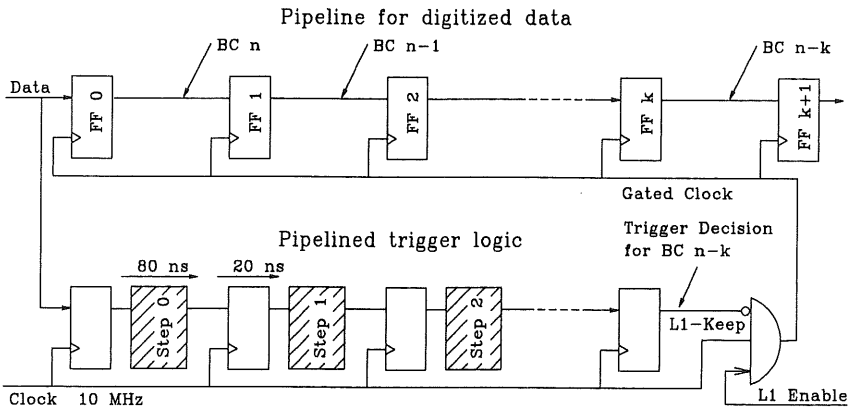


Fig. 60 A pipelined trigger distributes its logical functions (hatched boxes) between the registers of a shift register.

Appendix B: XILINX logic cell arrays

XILINX Logic Cell Arrays [56] (LCA) are fully configurable chips consisting of a matrix of Configurable Logic Blocks (CLB), and a number of peripheral Input / Output Blocks (IOB) associated with pins. All these blocks can be interconnected with each other by a hierarchy of programmable routing resources. The configuration memory can be thought of as a static RAM lying underneath the user-visible collection of CLBs, IOBs and interconnections, as sketched in figure 61. Table 7 gives an overview of the available dies of the XILINX 3000 series. Each die is available in a collection of different packages and speed grades.

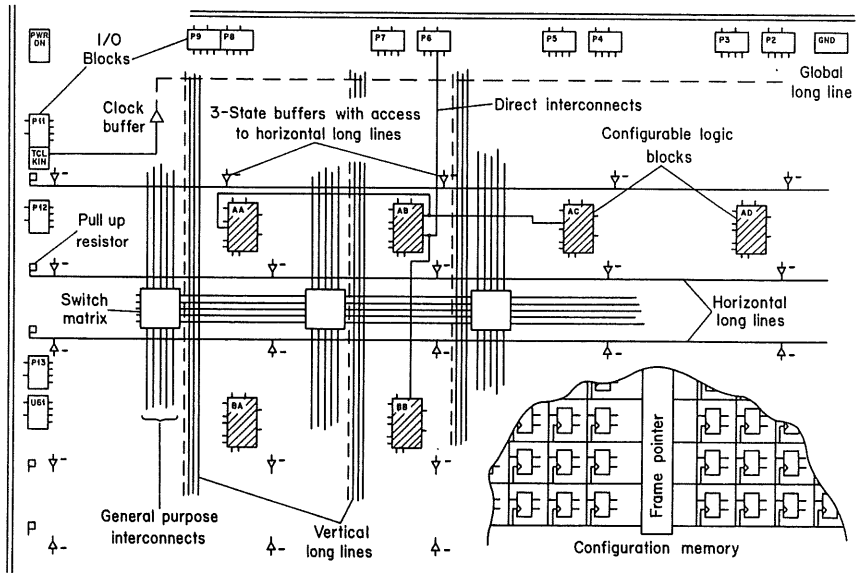


Fig. 61 The functionality of the logic blocks (CLBs) and interconnection resources inside a XILINX is configurable by loading an appropriate configuration bit stream into the underlying static memory upon power-up or after asserting a *reset* pin [56].

Die	Logic Capacity (gate equivalents)	CLBs	IOBs	Program Data (No. of bits)
3020	2000	64	64	14779
3030	3000	100	80	22176
3042	4200	144	96	30784
3064	6400	224	120	46064
3090	9000	320	144	64160

Table 7: XILINX 3000 series: available dies

Each CLB has a structure as shown in figure 62²⁷. The five inputs are fed to a combinatorial block, together with two feed-back lines Q_x and Q_y . The functions F and G are either equal, in which case they can provide any function from up to five of the seven input variables, or independent functions of (almost) any two sets of four input variables. A CLB also contains two registers, which can either operate as flip-flops or latches and get their input from D_{in} , F or G . The outputs X and Y can be programmed to be either Q_x or F and Q_y or G respectively.

The IOBs are also programmable to being either an input, output or a bi-directional connection with a tri-state output, each with selectable polarity. They contain a register each, again programmable to be either a latch or a flip-flop. The input characteristics can be selected to be either CMOS or TTL compatible. Some IOBs may not be connected to an external pin, dependent on the package used, in which case they can be used as an internal register.

Each CLB has direct interconnections with its four immediate neighbours, which results in a very high-speed link with only one switch transistor (*programmable interconnect point*, PIP) inbetween. Two long-lines run horizontally across the entire die between any two rows of CLBs. Tri-state buffers connecting to them allow the implementation of buses. Vertically, there are three long-lines between any two columns

²⁷ Described here is the functionality of the XILINX 3000 series. There also exists a 2000 series with a slightly simpler structure, e.g. CLBs with only four inputs. The new 4000 series on the other hand has significantly more interconnect resources.

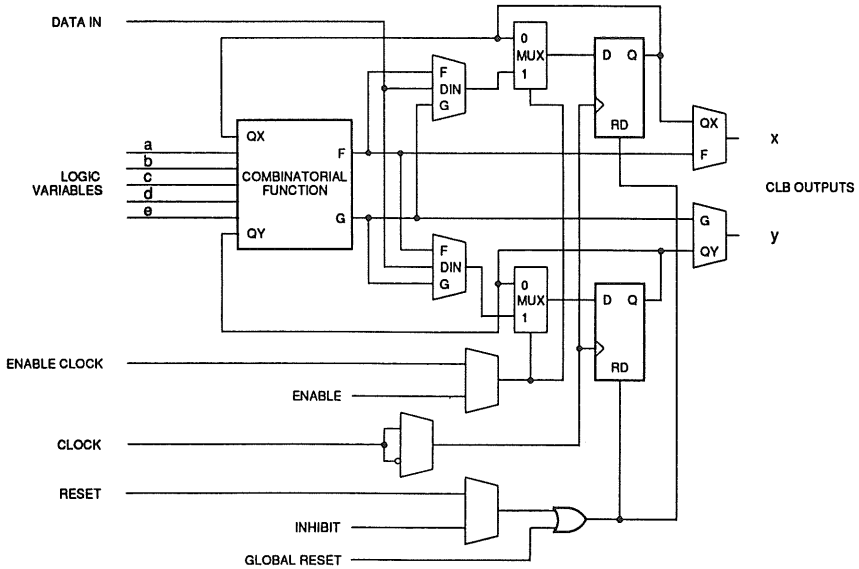


Fig. 62 A configurable logic block can be programmed to perform any function of five input variables. Two output registers are available [56].

of CLBs. For the larger dies, two of them are connectable half-length lines. These long-lines allow signals to travel fast over a greater distance. An additional global long-line can be connected to all clock inputs of all CLBs and IOBs to allow for low-skew clock distribution across the entire chip. Five general purpose interconnect lines run between any two columns and rows of CLBs. At the cross points, switching matrices offer almost any desired connectivity.

The XILINX chips come in speed grades of 50, 70 and 100 MHz²⁸, with maximum propagation delays through a CLB operated as a combinatorial block only of 14, 9 and 7 ns respectively. However, due to the delays occurring on the signal interconnections due to the various switching transistors passed through in PIPs and switching matrices, a good propagation delay estimate was found to be 20 ns/CLB for the 100 MHz version.

²⁸ 125 MHz versions became available after the design of the electronics described herein. Also, the new 3100 family is pin-compatible to the 3000 series, but faster due to new switch transistor layouts at PIPs and in switching matrices.

With the HERA clock frequency of 10.4 MHz, this calls for synchronization of all signal paths after a maximum of four CLBs passed.

As the configuration memory of a XILINX consists of static RAM, it needs reloading after every power cycle. Several options are available. The least flexible one uses a serial ROM connected to the XILINX. Upon power up, all necessary steering signals are provided by the XILINX to read its configuration from the ROM. The z-vertex trigger however is one of the applications that wants to profit from the reprogrammability of the LCAs. For such applications, programming through a computer interface is supported. An appropriate bit stream residing on the harddisk of a computer is loaded into a XILINX after deleting any old configuration already existing there.

The circuit design for LCAs is highly automated through the appropriate CAD software. After entering the circuitry into a schematic editor such as ORCAD, SCHEMA II, P-CAD, etc., the netlist is translated into a format suitable for the native XILINX CAD software package. The latter maps the schematic entities used, such as ORs, ANDs, multiplexers, counters, etc. onto the architecture of an LCA consisting of CLBs. The so mapped circuit can then be either routed by hand - a somewhat tedious task - or handed over to an auto router. Depending on the complexity of the circuit, measured mainly in number of connections per net, up to 95% of all CLBs can be used without sacrificing a 100% auto routing success.

Appendix C: Low energy cutoff in the single ray acceptance

A charged particle of finite and constant²⁹ energy travels along a helix inside the tracking detector of H1 due to a homogeneous magnetic field of 1.2 T parallel to the beam axis. It can be parameterized by the total momentum p , the transverse momentum p_t and the *distance of closest approach (DCA)* to the beam line together with z_0 , the z -coordinate at DCA. The R - φ projection of this helix is a circle which is independent of p . Its radius is given by $\rho = (p_t / B) \cdot (10^4/3)$ with $B = 1.2$ T, p_t measured in GeV and ρ resulting in mm.

The z -vertex trigger only accepts particle trajectories that cross both the CIP and COP (or forward MWPC) in the same φ -segment. Assuming a homogeneous φ distribution for tracks, an acceptance can be calculated from figure 63. For a given p_t (and thus ρ) and DCA, only trajectories *between* the two extremes 1 and 2 cross both chambers within the φ -segment drawn. Thus, comparing $\Delta\varphi = \varphi_s - |\varphi_0 - \varphi_1|$ with φ_s gives the acceptance $\mathcal{A} = \Delta\varphi / \varphi_s$ for $\Delta\varphi > 0$ ($\mathcal{A} = 0$ otherwise). The absolute sign takes care of trajectories with smaller ρ than sketched in figure 63(b), where track 1 touches the outer chamber in A and track 2 the inner in B . φ_s is the opening angle of one φ -segment, usually $2\pi/16$. To calculate φ_0 and φ_1 , one has to distinguish between the DCA circle laying inside (a) the circle formed by the track and outside (b). One calculates with $i = 0, 1$ [57]:

$$\varphi_i = \arccos\left(\frac{r_i^2 + DCA^2 \mp 2\rho \cdot DCA}{2r_i \cdot (\rho \mp DCA)}\right) \quad (21)$$

with the positive sign for case (b). $\Delta\varphi$ is forced to 0 if

- either of the arguments of the arccos is greater than 1 or less than -1 or
- $\rho < DCA$ (a) or
- $DCA + 2 \cdot r_0 < r_1$ (b) or
- $DCA > r_0$.

The single ray acceptance for trajectories with $DCA = 0$, thus possibly originating from a primary vertex along the beam line, has been plotted in figure 17 in chapter

²⁹ We shall neglect energy loss due to coulomb scattering.

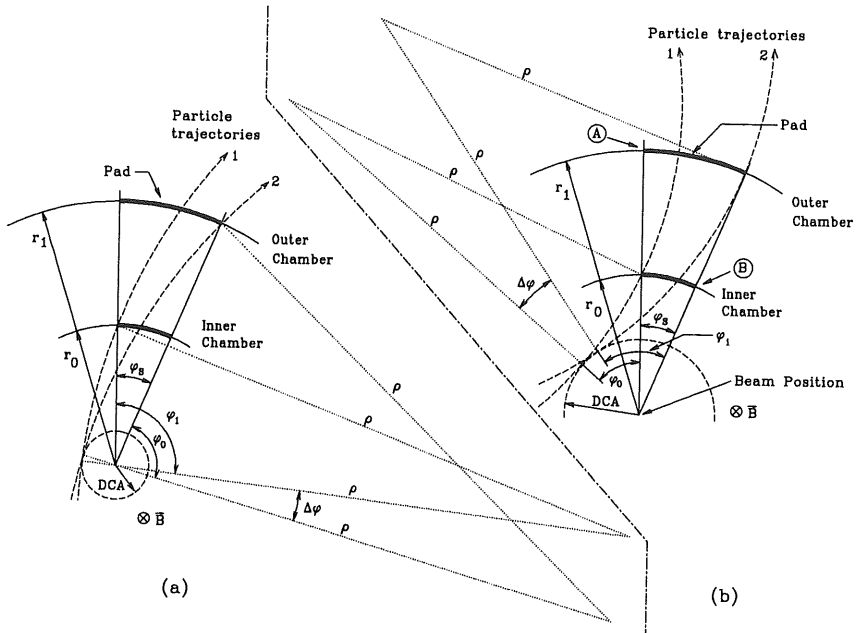


Fig. 63 For tracks with a given transverse momentum p_t and DCA, a probability for not crossing a ϕ -segment boundary can be calculated. Two cases (a) and (b) have to be distinguished.

3.3.1. Figure 64 shows the acceptance as a function of DCA. Note, that even low momentum tracks can reach high acceptance probabilities if their DCA is sufficiently large. These tracks, originating from secondary vertices, most probably in the beam pipe, add to the background of the z-vertex histogram, as they do not generally point to the primary vertex.

The R-z projection of the helix followed by a track with $DCA = 0$ and originating from z_0 is a sine curve, which crosses the forward MWPC plane at a radius $r - \Delta r$, with $r = z_0 \cdot \tan(\theta)$ the radius expected for an infinite momentum track. According to figure 65(a), one calculates:

$$\Delta r = z_{FW} \cdot \tan(\hat{\theta}) - \rho \cdot \sin\left(\frac{z_{FW} \cdot \tan(\hat{\theta})}{\rho}\right) \quad (22)$$

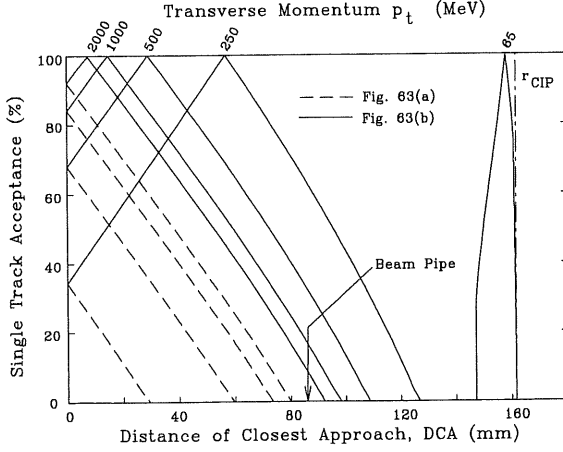


Fig. 64 The single track acceptance for low momentum tracks is dependent on the transverse momentum p_t and DCA. The solid lines correspond to case (a) in figure 63, the dashed lines to case (b).

Similarly, one calculates Δz at the radius r_{COP} of the COP for a track crossing both CIP and COP (figure 65(b)):

$$\Delta z = \left| \arcsin\left(\frac{r_{COP}}{\rho}\right) \cdot \frac{\rho}{\tan(\theta)} - \frac{r_{COP}}{\tan(\theta)} \right| \quad (23)$$

These derivations have to be compared with the pad size of the forward MWPC and the COP respectively at the crossing location. The forward MWPC pad size for the (logical) pad i is given by $\delta r_i = 2 \cdot (r_{i+1} - r_i) / (r_{i+1} + r_i) = 3.75\%$, using the radii r_i of the pad boundaries given in table 4 (p. 28) and taking into account the radial offset of the pads between the two layers of the chamber. The COP pad size is constant at $\Delta z_i = 120.7$ mm (see table 4). The probability to fire the same ray as the one which would have been activated by an infinite momentum track is plotted in figure 18 (p. 36) as a function of θ and p_t .

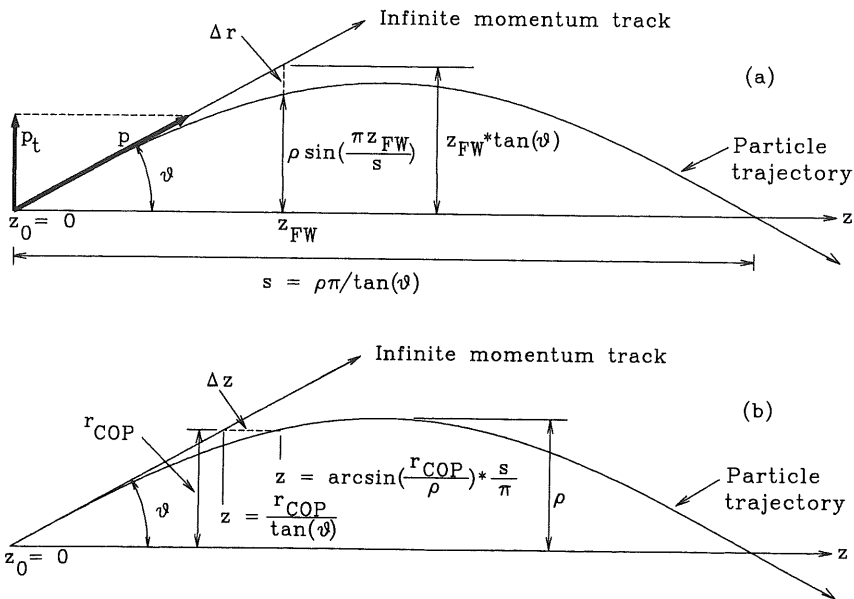


Fig. 65 The helix of a low momentum track projects a sine curve onto the R-z plane and thus does not necessarily cross the same FPC or COP pad as an infinite momentum track would. Instead, it is deflected by Δr (a) and Δz (b) respectively.

Figure 18 restricts the range of ϑ such that only rays constructed from pads of CIP and the forward MWPC are included. Central rays, built from pads of CIP and COP, correspond to $\vartheta > 25.5^\circ$ (see figure 16, p. 35). Their probability to fire the same ray as an infinite momentum track is above 80% for $p_t > 0.5$ GeV and above 95% for $p_t > 1$ GeV. Thus, this effect is negligible compared to the low energy cutoff discussed above and shown in figure 17 if the φ -segmentation of the z-vertex trigger is chosen to be 16-fold.

Appendix D: Dictionary of abbreviations

BC	Bunch Crossing, 96 ns
BEMC	Backward Electromagnetic Calorimeter
BRDB	Big Ray Distribution Box
CAD	Computer Aided Design
CERN	Centre Européen de Recherces Nucléaires
CIP	Central Inner Proportional Chamber
CIZ	Central Inner z-Chamber
CJC	Central Jet Chamber
CLB	Configurable Logic Block (of a XILINX LCA)
CMOS	Complementary MOS
COP	Central Outer Proportional Chamber
COZ	Central Outer z-Chamber
CTL	Central Trigger Logic
DAQ	Data Acquisition
DCA	Distance of Closest Approach (of a track reconstructed in the R- ϕ plane to the beam line)
DESY	Deutsches Elektronen Synchrotron
DIS	Deep Inelastic Scattering
DST	Data Summary Tape
ECL	Emitter Coupled Logic
FER	Front End Ready
FPC	Forward Proportional Chamber
HERA	Hadron Elektron Ring Anlage
HU	Horizontal Unit (Euro-mechanics, 5.08 mm) [48]
IOB	Input / Output Block (of a XILINX LCA)
JADE	one of the experiments at PETRA
L1, L2, L3, L4	Level 1, 2, 3, 4 trigger
LCA	Logic Cell Array (XILINX)
LHC	Large Hadron Collider (at CERN)
LSB	Least Significant Bit
MOS	Metal Oxide Semiconductor
MSB	Most Significant Bit
Mux	Multiplexer
MWPC	Multiwire Proportional Chamber

NIM	Nuclear Instruments and Methods, standard for electronic modules used in high energy physics and based on ECL signal levels
PCB	Printed Circuit Board
PETRA	e^+e^- collider at DESY, now pre-accelerator for HERA
PIP	Programmable Interconnection Point (of a XILINX LCA)
POT	Production Output Tape
PSI	Paul Scherrer Institut
QCD	Quantum Chromo Dynamics
RAM	Random Access Memory
RISC	Reduced Instruction Set Computer
ROM	Read Only Memory
SSC	Superconducting Super Collider (in Texas, USA)
TDC	Time to Digital Converter
TTL	Transistor-Transistor Logic
ToF	Time of Flight detector (scintillator wall) (cf. Fig. 8, p. 24)
VME	Versatile Module Europe [48]
VU	Vertical Unit (Euro-mechanics, 38.9 mm) [48]
WWA	Weizsäcker-Williams Approximation
XILINX	Brand name for LCAs, cf. Appendix B

Bibliography

- [1] R. Rückl, Nucl. Phys. B234 (1984)91
- [2] Proc. of the study for an ep facility for Europe, edited by U. Amaldi, DESY-report 79-48 (1979);
Proc. of the HERA workshop, Hamburg 1987, edited by R. D. Peccei, DESY, Hamburg (1988), vol. I and II;
Proc. of the workshop on physics at HERA, Hamburg 1991, edited by W. Buchmüller and G. Ingelman, DESY, Hamburg (1992), vol. I, II and III.
- [3] H1 Collaboration, T. Ahmed et al., The H1 detector, Nucl. Instr. and Meth., to be submitted;
F. W. Brasse, The H1 Detector at HERA, Proc. of the XXVI International Conference on High Energy Physics at Dallas, 1992; DESY 92-140, Oct. 1992
- [4] K. J. F. Gaemers, M. van der Horst, Nucl. Phys. B316 (1989) 269
- [5] J. Tutas, Myonen im H1-Detektor, Ph. D. thesis, PITHA 91/10, RWTH Aachen (1991)
- [6] P. Robmann, The central inner z-chamber of the H1 experiment at HERA, Ph. D. thesis, University of Zurich, (1993), in preparation
- [7] H1 Collaboration, Technical Proposal to build Silicon Tracking Detector for H1, DESY, PRC 92/01, July 1992
- [8] W. J. Haynes, Microprocessor based data acquisition systems for HERA experiments, in CERN Yellow Reports, CERN 90-06 (1990)
- [9] W. J. Haynes, Experiences at HERA with the H1 Data Acquisition System, DESY 92-129, Sept. 1992
- [10] H1 Collaboration, T. Ahmed et al., Total photoproduction cross section measurement at HERA energies, Phys. Lett. B299 (1993) 374-384
- [11] Review of Particle Properties, Phys. Lett. B239 (1990)
- [12] H1 Collaboration, Technical Proposal for the H1 Detector, Hamburg 1986
- [13] S. P. Denisov et al., Nucl. Phys. B61 (1973) 62
- [14] A. Campbell, A RISC multiprocessor event trigger for the data acquisition system of the H1 experiment at HERA, Int. Conf. Real Time '91, Jülich, Germany (1991)
- [15] J. Fent et al., Proposal for a second level neural network trigger, MPI Munich internal report, March 17, 1992

- [16] H. Krehbiel, The H1 Trigger Decider: From Trigger Elements to L1-Keep, H1 internal report, H1-09/92-239, DESY, Hamburg (1992)
- [17] Th. Wolff, et al., Nucl. Instr. and Meth. A323 (1992) 537, H1 internal report H1-02/92-213
- [18] H. J. Behrend and W. Zimmermann, A hardwired trigger processor using Logic Cell Arrays (XILINX), Proc. Int. Conf. on Computing in High Energy Physics, Tsukuba, Japan (1991), p.237
- [19] H. Brettel, et.al., Calorimeter Event t_0 and Trigger Elements for CTL and DSP, MPI Munich internal report, H1-MPI-140, Oct. 22, 1990, unpublished
- [20] J. Ban et al., The BEMC single electron trigger, H1 internal report H1-07/92-235, DESY, Hamburg (1992)
- [21] J. Tutas, A level 1 trigger from the limited streamer tube system, H1 internal report H1-07/91-185, DESY, Hamburg (1991)
- [22] T. Ahmed et al., A pipelined first level forward muon driftchamber trigger for H1, Proc. Int. Conf. on Computing in High Energy Physics, Annecy 1992; H1 internal report H1-10/92-251
- [23] H. Krehbiel, MWPC Receiver Card; Semi-final circuit diagram, H1-MWPC Note No. 5, DESY, Hamburg, May 26, 1988, unpublished
- [24] R. Eichler et al., The first level MWPC trigger for the H1 detector, H1 internal report H1-04/87-61, DESY, Hamburg (1987)
- [25] J. Olsson et al., Nucl. Instr. and Meth. 176 (1980) 403
- [26] K. Müller et al., Nucl. Instr. and Meth. A312 (1992) 457; H1 internal report H1-09/91-192
- [27] R. Eichler et al., Note on Topological Triggers for J/ψ Events, H1 internal report H1-01/91-162, DESY, Hamburg (1991)
- [28] Carola Schmidt, DESY Hamburg, W-2000 Hamburg 52, private communication
- [29] Stephan Egli, University of Zurich, 8001 Zürich, private communication
- [30] I. Endo et al., Nucl. Instr. and Meth. 1988 (1981) 51
- [31] K. Kleinknecht, Detektoren für Teilchenstrahlung, Teubner Studienbücher, Stuttgart 1992, p. 98 ff.;
H. G. Fischer et al., Proc. Int. Meeting on Proportional and Drift-Chambers, Dubna 1975, JINR report D 13-9164
- [32] i.g. W. R. Leo, Techniques for Nuclear and Particle Physics Experiments, Springer Verlag, 1987, p. 24 ff.

- [33] i.g. W. R. Leo, *Techniques for Nuclear and Particle Physics Experiments*, Springer Verlag, 1987, p. 46 ff.
- [34] S. Bentvelsen et al., in *Proc. Workshop on Physics at HERA (DESY, Hamburg 1992)*, vol. I, p. 23 ff.
- [35] H1 Collaboration, T. Ahmed et al., *Phys. Lett. B*298 (1993) 469-478
- [36] K. Müller, University of Zurich, 8001 Zürich, private communication
- [37] S.I. Alekhin et al., *Compilation of cross sections*, Vol. 4, report CERN-HERA 87-01 (1987)
- [38] in *Proc. Workshop on Physics at HERA (DESY, Hamburg 1992)*, vol. I: G.A. Schuler (p. 461 ff.), A. Levy (p.481 ff.) and S. Levonian (p.499 ff.); G. Schuler and J. Terron, CERN preprint CERN-TH.6415/92 (1992)
- [39] C.F.Weizsäcker, *Z. Phys.* 88 (1934) 612;
E.J. Williams, *Phys. Rev.* 45 (1934) 729
- [40] ZEUS Collab., M.Derrick et al., *Phys. Let. B*293 (1992) 465
- [41] A. Donnachie and P.V. Landshoff, CERN preprint CERN-TH.6635/92 (1992)
- [42] H. Abramowicz et al., *Phys. Lett. B*269 (1991) 465
- [43] M. Drees and F. Halzen, *Phys. Rev. Lett.* 61 (1988) 275;
R. Gandhi and J. Sarcevic, *Phys. Rev. D*44 (1991) R10
- [44] H1 Collaboration, T. Ahmed et al., *Phys. Lett. B*297 (1992) 205-213
- [45] W.Stirling and Z. Kunszt, in: *Proc. HERA Workshop (DESY, Hamburg, 1987)*, vol. I, p.331 ff.
- [46] S. Eichenberger, *Development of the Ray Finder Electronics for the z-Vertex Trigger for the H1 Detector at HERA*, Diploma thesis, University of Zürich (1988); H1 collaboration internal report H1-11/88-96, unpublished.
- [47] NEC Electronics (Europe) GmbH, Oberratherstrasse 4, 40472 Düsseldorf, BRD
- [48] The VMEbus Specification Manual, also known as IEC 821 Bus or IEEE P1014/D1.2
- [49] H. Krehbiel, *The Fanout Card of the Subsystem Trigger Controller*, User's manual, unpublished
- [50] Crate manufacturer: Wiener, Plein & Baus GmbH, Müllersbaum 20, 51399 Burscheid, BRD
- [51] J. Stastny, V. Schröder, *H1-Racks, Prototype Test*, H1 internal report H1-09/88-91, DESY, Hamburg (1988)

- [52] P. Huet, The H1 MWPC data acquisition, Ph. D. thesis, Bruxelles 1993
- [53] Hybrid Memory Products LTD, Elm Road, West Chirton Industrial Estate, North Shields, Tyne & Wear, England NE29 8SE
- [54] Data Delay Devices, PDU-16F-2, distributed by Telemeter Electronic GmbH, 86609 Donauwörth, BRD.
- [55] The *Big Ray Distribution Box* is currently (Spring 1993) being built and installed by LAL, Université de Paris-Sud, F-91405 Orsay Cedex, France.
- [56] XILINX: The Programmable Gate Array Data Book, XILINX Inc., 2100 Logic Drive, San Jose, CA 95124, USA
- [57] H. P. Beck, University of Zurich, 8001 Zürich, private communication

Acknowledgements

I would like to thank the many people I had interesting and fruitful discussions with during the work on this thesis. In particular, I would like to express my gratitude to:

- Ueli Straumann for his excellent technical and moral support even during the most difficult times, when I was close to giving up.
- Katharina Müller, Robert Roosen, Erik Evrard and Philippe Huet, who were responsible for the proportional chambers and the data acquisition software. Despite the narrow working conditions in the aisle of the electronic trailer, it was fun to work with them.
- The staff of the Physics Institute, especially Karl Esslinger and Walter Fässler for their help and suggestions.
- Hanspeter Beck and Stephan Egli for their work in understanding the trigger efficiency and in monitoring its correct operation.
- J. Stastny (DESY) and Mr. Schleuniger (PSI) for their efforts in routing XILINX programs and printed circuit boards.
- Peter Robmann and Thom Wolff for the many discussions on general topics.
- Last, but not least, Prof. Dr. Peter Truöl for the trust he had put in me. He gave me an exceptionally large degree of freedom in designing the system, which allowed me to learn many aspects of managing such a project.

This list is far too short to be complete. To the many people from the H1 collaboration, the Zurich H1 group, the Physics Institute of the University of Zurich and others I have not mentioned here:

Thanks !

Curriculum vitae

Personalien:

Name: Eichenberger
Vorname: Stefan Otto
Geboren: 10. Mai 1959 in Zürich
Bürgerort: Zürich und Beinwil a.S.

Bildungsgang:

1966 - 1972 Primarschule in Zürich
1972 - 1975 Realgymnasium Rämibühl, Zürich
1975 - 1979 Mathematisch-Naturwissenschaftliches Gymnasium Rämibühl,
Zürich
1979 Matura Typus C
1980 - 1988 Studium der Physik (Mathematik, Publizistik) an der Universität
Zürich
1988 Diplomarbeit in Experimentalphysik unter der Leitung von
Prof. Dr. P. Truöl
Titel: 'Development of the Ray Finder Electronics for the z-Ver-
tex Trigger for the H1 Detector at HERA'
1988 Diplom in Experimentalphysik
1988 - 1993 Wissenschaftliche Mitarbeit beim H1 Experiment an HERA in
Hamburg (DESY) und Dissertation bei Prof. Dr. P. Truöl

Dozentenverzeichnis:

C. Amsler	P. Gabriel	U. Niederer	T. Schelbert
K. Bauknecht	A. Guttman	B. D. Patterson	B. Schmid
W.-J. Beyn	M. Haller	R. E. Pixley	H.-R. Schwarz
H. Bonfadelli	J.-J. Hoffmann-Nowotny	H. S. Pruis	V. Siedler
D. Brinkmann	P. Klein	G. Rasche	N. Straumann
E. Brun	H. W. Kopp	W. Reichart	U. Straumann
B. Derighetti	W. Kündig	U. Saxer	K. Strebel
R. Engfer	P. F. Meier	M. Schanne	A. Thellung
D. Frei	V. Meyer	G. Scharf	P. Truöl